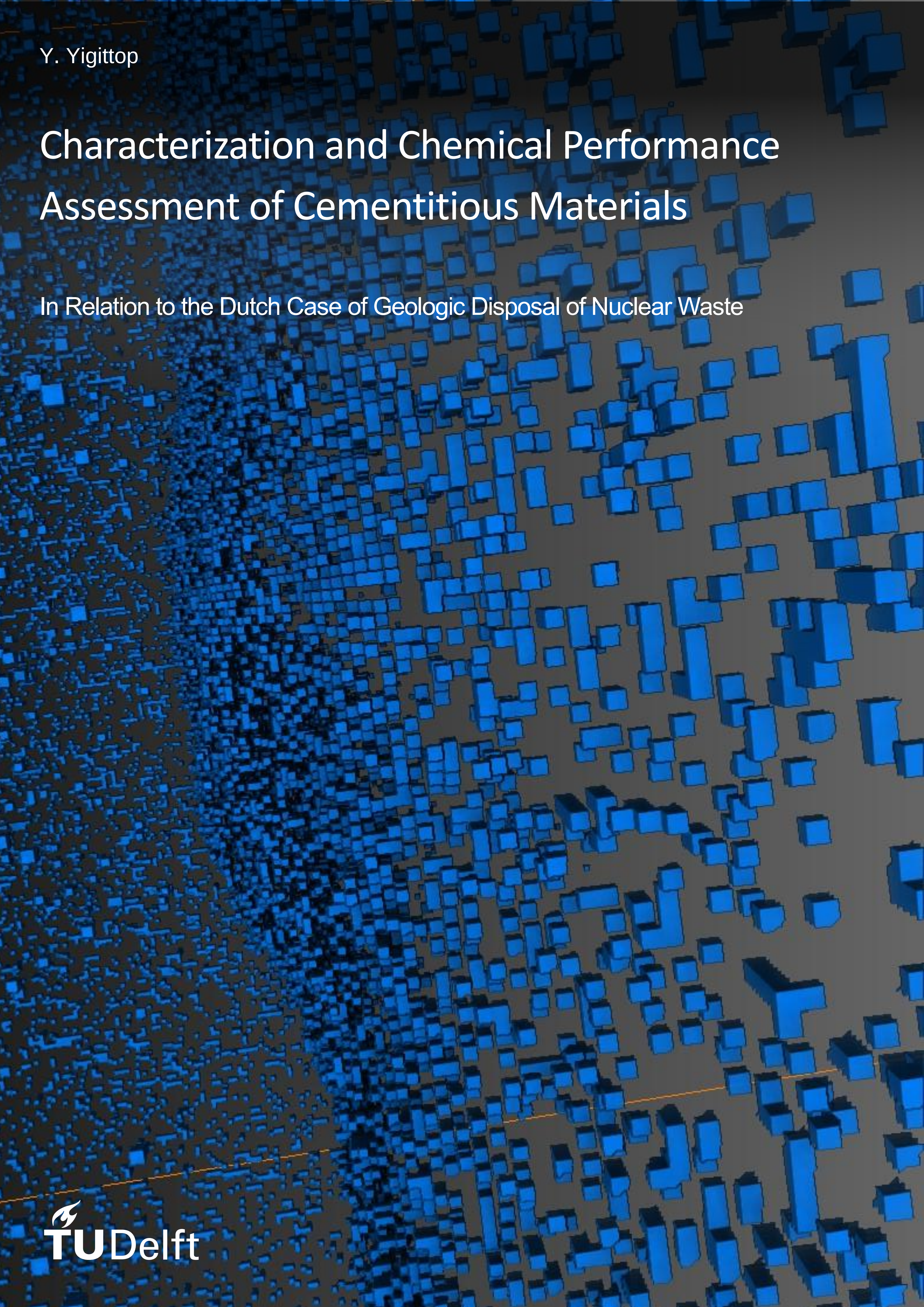

Y. Yigittop

Characterization and Chemical Performance Assessment of Cementitious Materials

In Relation to the Dutch Case of Geologic Disposal of Nuclear Waste

TUDelft

Characterization and chemical performance assessment of cementitious materials in relation to the Dutch case of geologic disposal of nuclear waste

---

by

Y. Yigittop

in partial fulfilment of the requirements for the degree of

Master of Science
in Materials Science and Engineering

at the Delft University of Technology,
to be defended publicly on Wednesday December 11th, 2019

Thesis committee:	Dr.ir. S.E. Offerman	Chairman
	Dr. L. van Eijck	Member
	Dr. A.L. Smith	Member

An electronic version of this thesis will be available at http://repository.tudelft.nl/.

List of content

List of figures

Summary

As we approach 2020, it has become evident that renewable energy alone is not enough to reduce CO_2–emissions of electricity production to the levels of the Paris agreement. In this agreement, a long-term goal is to limit the global temperature rise below 2°C permanently, compared to pre-industrial global average temperature. Nuclear energy plays an important role to reach this goal, as stated in the four main scenarios of a recent report of the IPCC. How electricity can be generated with nuclear technology has improved significantly. Compared to conventional nuclear power plants, *Generation IV* nuclear power plants are meltdown-proof and up to 300x more fuel efficient. Some future generation-IV reactors are even capable of burning existing nuclear waste. Generation IV nuclear reactors are soon to become a reality. A high temperature gas reactor (HTGR) for example is scheduled to be deployed in South-Africa by 2021 (Kadak, 2016) and a gas-cooled fast reactor in Olker (France) by 2025 (Arostegui & Holt, 2019).

Nuclear waste has to be handled with care. The main reason being that the waste continues to emit ionizing radiation for periods of hundreds of thousands of years. Furthermore, The Netherlands is expected to have accumulated 170.000 barrels of nuclear waste by 2130. In a report by COVRA (Centraal Orgaan voor Radioactief Afval) published early this year, the concept of nuclear waste disposal deep underground is investigated. The challenge is to prevent the nuclear waste from entering the biosphere, by incarcerating the waste in an underground nuclear waste storage facility using a combination of compact materials including steel and concrete.

This thesis is about how the internal structure of concrete can be visualized using non-destructive methods and how it is affected by physiochemical processes that are expected at depths of 500 meters beneath The Netherlands. The purpose is to introduce methods to assess the performance of candidate concrete samples and compare the findings with concrete samples that have undergone degradation in the lab. The degradation is performed by immersing concrete samples in solutions containing chlorides and sulphates, in similar concentrations as the micro-scale pore water pockets in Boom clay. The pore size distribution, sorptivity and sphericity (shape of pores) of non-degraded concrete and degraded concrete samples are compared.

X-ray radiography and neutron tomography at the Reactor Institute of Delft are used to reveal the internal structure of concrete as well as to obtain the sorptivity. The limitation in being able to distinguish objects in Neutron Tomography is about 250 μm when image processing algorithms are not used. With the aid of algorithms, porosity and pore size distributions are obtained with pore sizes from up to 110 μm. The difference between these accuracies is explained by the fact that algorithms take previous and next slice automatically in consideration. Sorptivity is a transport parameter that describes the rate of capillary suction. To validate the results, a standardized test of ASTM is performed as well. The samples investigated with x-ray radiography, neutron tomography and sorptivity are candidate materials for:

- Gallery lining concrete, CEM II/A to B-V (tunnel walls for mechanical support)
- Encapsulation concrete, CEM III/B 42.5 LH/SR (incarceration of nuclear waste)
- Foam concrete, CEM III/B 42.5N LH/SR + Foaming Agent (to fill up tunnels)

The results show an increase of the sorptivity by a factor of 7.2 and 7.5 for the concrete samples that are exposed to sulphates and chlorides, respectively. The sorptivity values measured are in agreement with literature values. Tomography studies revealed that not only do the pores grow in size as a result of concrete degradation by chlorides, but new pores also emerge, although by a smaller factor. In a

similar research performed in 2016, it is found that chloride attack exposed concrete sample suffers greatest loss in Vickers hardness (Xiong, et al., 2016), which is in line with the findings in this thesis. The assumption is made that an increase in sorptivity is a result of dissolution of cement phases within the concrete. Chloride attack exposed concrete samples suffer the most by dissolution of hydration phases.

1. Introduction

1.1 Geologic repository for nuclear waste

Nuclear waste originates from various industries. Other than nuclear reactors, they are generated in healthcare (for imaging purposes), agriculture, research and education. Currently, The Netherlands has one organization that is responsible and licensed to collect and store nuclear waste. The organization is COVRA (Centrale Organisatie Voor Radioactief Afval). The current policy dictates that nuclear waste is to be stored in a central location for up to 100 years. After this period, the nuclear waste will be sufficiently cooled down for long term storage.

Nuclear waste is classified in two categories, e.g. low-level waste (LLW) and high-level waste (HLW). Low-level waste are materials that have been contaminated with nuclear waste, typically protective covers, clothings, tissues, filters etc. High-level waste on the other hand, originate mostly from uranium fuel used in a nuclear fission reactor. Once it is no longer efficient to use the fuel, it is disposed of. Fission products include cesium-137 and strontium-90. The half-life time of these materials range from decades to millennia.

There is a worldwide consensus that deep underground storage of nuclear waste is the safest choice, mostly meant for the HLW. Depths of 300 to 800 meters are typically, actual depth will depend on the host rocks/clay beneath the surface. At 500 meters depth in The Netherlands, Boom clay has been identified as the major host clay. Bentonite is also present, both Boom clay and bentonite are smectite rich clay. These materials have been excavated and investigated, results show that they have a low hydraulic gradient and slightly alkaline pH when under the conditions at 500 meters beneath The Netherlands. The migration of radionuclides through these materials is confirmed to be diffusion controlled. Therefore, the migration path is relatively low, making geologic repository for nuclear waste beneath The Netherlands ideal.

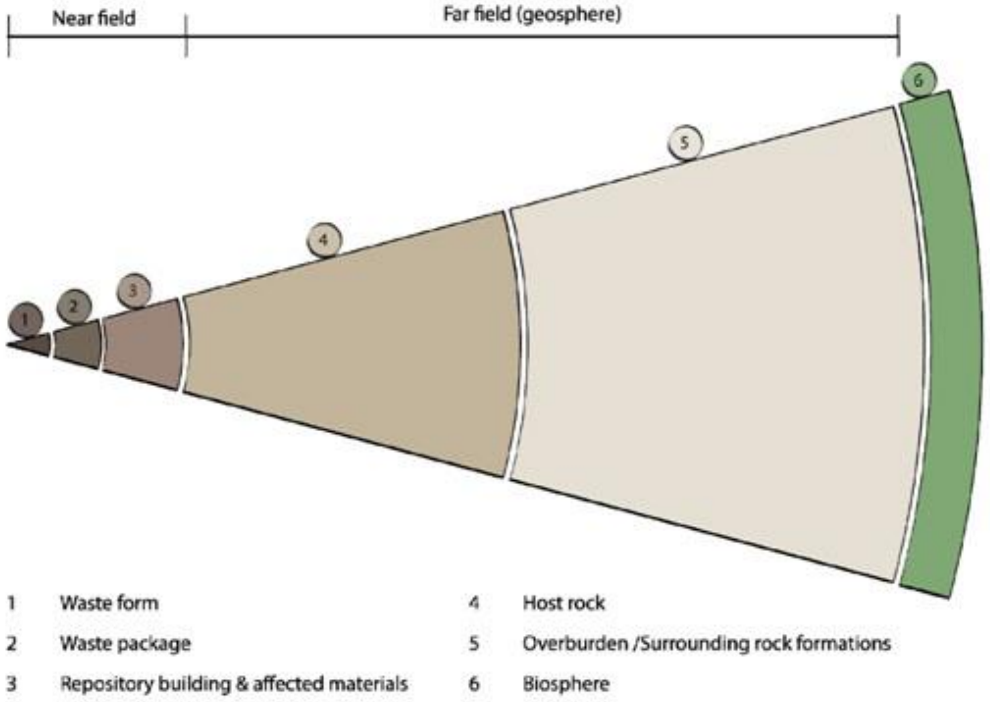

Figure 1: Compartments of a design of a geologic repository concept

Figure 1 shows a schematic overview of the barriers that nuclear waste would face when stored in a deep underground storage facility. Boom clay and bentonite (the host rock/clay) starts from the fourth position. Before that, nuclear waste is incarcerated primarily by concrete/cement-based materials. Diffusivity of radioactive elements found in HLW through far-field compartments (labelled 4 to 6 in Figure 1) is a heavily investigated phenomena, but outside the scope of this thesis.

A more practical demonstration of a geologic nuclear waste disposal site is shown in Figure 2. The site consists of tunnels, filled with concrete/steel barrels which contain the waste. The space between the gallery lining and the drums are filled with foam concrete (backfill) for mechanical support. Current designs show that the thickness of the gallery lining concrete that make up the tunnels is 0.4 meters, with an outer diameter of 4.8 meters.

Figure 2: Artist impression of geologic nuclear waste disposal site (Verhoef, et al., 2014)

From the nuclear waste to the biosphere, the path is as follows:

Waste containment (package) -> foam concrete -> gallery lining concrete -> boom clay

Retention performance by concrete and cement-based materials (near-field compartments 1 to 3, from Figure 1) is of primary interest in this work. Concrete and cement-based materials are engineerable, to which innovation is possible for improved and prolonged incarceration. This brings us to the CEBAMA project.

1.2 The CEBAMA project

Cebama (cement-based materials) is a project funded by the European Atomic Energy Community (EURATOM). It is a collaborative project under the Horizon 2020 research and training program, with the goal to investigate the feasibility of implementing a geological repository. The structural components of a repository consist of cementitious materials, which are:

1. Gallery lining for mechanical support of the repository
2. Encapsulation of the nuclear waste in the shape of a barrel
3. Back-fill materials to fill the void in the repository after the barrels are in place

The CEBAMA project had selected the NERA department of RID (Reactor Institute Delft) as one its participants, along with many other research institutes and universities across Europe. The European Commission acknowledges the need to address the issue of long-term disposal of nuclear waste. As a result, 3.9 million Euros has been financed for the CEBAMA project which has started on June 1st 2015 and is to last for 4 years.

Depending on the specialization of the CEBAMA participant, specific tasks are given. Harnessing the power of the nuclear reactor at the university, the NERA department has been assigned its own tasks, one of them being the utilization of the Neutron source the reactor produces as well as X-Ray imaging setup (borrowed from NPM2 department). This mostly encompasses the research project by Yasin Yigittop. Additionally, standardized tests have been carried out for candidate concrete specimens. Concrete undergoes physio-chemical alterations when exposed to natural ground water. This addresses a safety concern when used for mechanical support in an underground nuclear waste storage facility. Several concrete specimens have been degraded in the lab in an accelerated process by exposure to high concentrations of sodium sulphate and ammonium chloride, separately. Their performances have been assessed using ASTM standardized tests and x-ray transmission imaging. The sorptivity, a transport parameter, has been measured and compared for non-degraded and degraded concrete.

1.3 Master's project - Research questions

Boom clay and concrete materials are materials investigated in this master project. The goal of the research is to visualize and characterize the internal structure of clay and concrete samples and quantify the influence of concrete degradation on the internal structure in the Dutch case of geologic nuclear waste disposal.

The presence of groundwater (naturally) in the pores of the clayey rock will cause physicochemical modifications in the concrete matrix (carbonation, leaching, carbonates precipitation) due to its neutral pH value and the high concentrations of sulphates and chlorides. Cementitious material is the most commonly used medium in the safe disposal of low and intermediate level radioactive waste. It may be used both as a barrier to prevent water from contacting the radioactive nuclides, and as an encapsulant against the migration of radionuclides. An underground disposal site typically contains multiple types of concrete. Current designs show that nuclear waste is encapsulated in fine cement, stored in tunnels which are then to be filled with foam-based concrete. The gallery lining of the tunnels are made of concrete with coarse aggregates for mechanical support. Among more samples, both the gallery lining concrete and the foam-based concrete are investigated in this study.

Both the barrier function and encapsulating function are susceptible to degradation induced by the presence of groundwater (flooding). Since high-level nuclear wastes must be isolated from the biosphere for a period in the order of 100.000 years, it is of fundamental importance to predict the performance of a geologic disposal site.

In order to establish a proof of principle, in this study the concrete specimens (provided by COVRA) have been analyzed with neutron tomography. The internal structure is revealed and with the data, the pore size distributions are obtained. The degradation that concrete will undergo when exposed to the conditions at 500 meters depth, is simulated in the laboratory. The boom clay pore water contains ammonium chloride and sodium sulphates, which induce physio-chemical alterations of concrete. The effect of this degradation has been measured by performing another neutron tomography measurement of degraded concrete samples.

The contact of boom clay with concrete will induce alterations over a long time-frame. Sorptivity is a transport parameter that gives information as to what degree solutions can migrate through an object. Sorptivity has been measured using X-ray radiography and the data is compared with sorptivity obtained using a standardized test method from ASTM. By obtaining this data of the concrete samples that were degraded in the lab and comparing it with sorptivity data of non-degraded concrete samples, allows the visualization of the impact of concrete degradation under geologic conditions in the Netherlands.

The data obtained from all these measurements will answer the following questions:

1 **What are the limits in the Neutron Tomography set-up at RID?**

2 **To what extent is the internal structure of concrete with Neutron Tomography quantifiable?**

3 **With the imaging set-up at RID, is it possible to visualize the water uptake over time?**

4 **Can the concrete degradation be visually revealed with Neutron Tomography?**

5 **Which concrete degradations are imminent, can the impact on the internal structure of concrete be quantified by measuring sorptivity?**

The internal structures of Boom clay and concrete samples are obtained with neutron tomography. The impact on sulphate and chloride attack on concrete is investigated by exposing concrete samples to a sodium sulphate and ammonium chloride solution. Afterwards the sorptivity is measured using X-ray radiography and using the standardized ASTM test. The difference between the pore size distribution of non-degraded and degraded samples are compared to quantify the impact of concrete degradation.

2. Theory

2.1 Concrete

Cement-based materials are by default unstable in the long-time perspective. The interaction between concrete and the environment is the most significant cause of the chemical alteration of concrete. Generally, the first period of alteration is caused by contact with atmospheric gases, especially carbon dioxide. The later degradation is mainly governed by the groundwater composition with which the concrete tries to equilibrate. As a result of the latter degradation, both the composition of the concrete and the groundwater change over time. In general, the concrete degradation process should be treated as a combination of multiple degradation mechanisms occurring simultaneously. Since the groundwater composition is known for the Dutch case of geologic repository system, the type of degradations that would occur can be better estimated.

In cement chemistry, abbreviations are often used for compounds and are listed below for convenience:

$C = CaO$
$M = MgO$
$T = TiO_2$
$S = SiO_2$
$K = K_2O$
$P = P_2O_5$
$A = Al_2O_3$
$\bar{S} = SO_3$
$H = H_2O$, OH
$F = Fe_2O_3$
$N = Na_2O$
$\bar{C} = CO_2$

Generally, in the preparation of concrete, cement is mixed with water to bring about a cement paste which starts the setting to create concrete. EN 197-1 defines Portland cement as a hydraulic material consisting, by mass, at least 2/3 of calcium silicates and the remainder of aluminium- and iron-containing phases. By sintering calcium-, silicon-, iron-oxides (obtained from limestone, clay, etc) and small amounts of other materials in a kiln, Portland cement clinker is created. Grinding the clinker results in Portland cement in powder form, classified as CEM I according to EN 197-1 standard. Mixing the portland cement with water makes up concrete. Prior to the setting of concrete, additives may be added to portland cement, such as quartz sand and binders, to enhance the properties of concrete. It is also common to have a fraction of portland cement substituted by other compounds, such as granulated blastfurnace slag. The cement classification then changes from CEM I to CEM III. Blastfurnace slag consists of calcium-, magnesium-, aluminium- and silicon-oxides.

2.1.1 Hydration products

The emerging products after mixing portland cement with water are called hydration products and are summarized below (adapted from (Lagerblad & Tragardh, 1994)). For simplicity, pure portland cement is considered. The composition of the hydration products is related to temperature and curing conditions.

1. **Calcium-silica-hydrate (C-S-H)**
   Main hydration product, which is amorphous to semi-crystalline. Ca/Si molar ratio varies between 0.8 and 3. The CSH can also contain some alkalis, sulphate and chloride ions.

2. **Calcium dihydroxide (CH)**
   Also called portlandite, a common crystalline product in concrete

3. **AFm: abbreviation for "alumina, ferric oxide, mono X " or (Al_2O_3 – Fe_2O_3 – mono)**

Term used for a group of phases of calcium aluminate hydrates with the general formula:

$$[Ca_2(Al,Fe)(OH)_6] \times X \times yH2O$$

Where X is a singly charged anion or half a double charged anion. Common examples are OH^-, SO_4^{2-}, Cl^- and CO_3^{2-} (Taylor, 1993). Most common phases of AFm are: C_4AH_x, where x varies in setting conditions, $C_4AC_{0.5}H_{12}$, C_4ASH_{12} (monosulphate), $C_4(CL^-)H_{10}$ (Friedel's salt) and C_2AH_8.

4. **AFt: abbreviation for "alumina, ferric oxide, tri X" or (Al_2O_3 – Fe_2O_3 – tri)**
   Another group of phases with the general formula:

$$[Ca_3(Al,Fe)(OH)_6 \times 12\ H2O]_2 \times X_3 \times yH2O$$

Where y<2 and X is a doubly charged anion or two singly charged anions. Examples are: SO_4^{2-}, $H_2SO_4^{2-}$ and CO_3^{2-}. Most common phases of AFt are:

○ Ettringite:	$Ca_6(Al,Fe)_2\ (OH)_{12}$ x $24H_2O$ x $(SO_4)_3$ x $2H_2O$
○ Thaumasite:	$Ca_3Si(OH)_6$ x $12H_2O$ x SO_4 x CO_3
○ Jouravskite:	$Ca_3Mn(OH)_6$ x $12H_2O$ x SO_4 x CO_3

With high contents of chloride anions, a chloride Aft phase is stable:

○ Tricalcium aluminate	$[Ca_3Al(OH)_6$ x $12H_2O]_2$ x $(Cl)_6$ x $2H_2O$

5. **Sulphates phases**
   These phases include sulphates that originate from the gypsum used in the cement. Most of the sulphates are consumed to create the hydration product ettringite. Some gypsum may remain unreacted after the concrete has set. Another phase that may be formed under specific conditions which includes sulphates is syngenite $K_2CA(SO)_4 \times H_2O$.

One example of the distribution of the hydration product is shown in Figure 3.The concrete composition stems from a conceptual model of a high-quality concrete of W/C ratio between 0.4 and 0.5 used by Swedish researchers to gain understanding in long time degradation of concrete in a deep nuclear waste repository (Lagerblad & Tragardh, 1994).

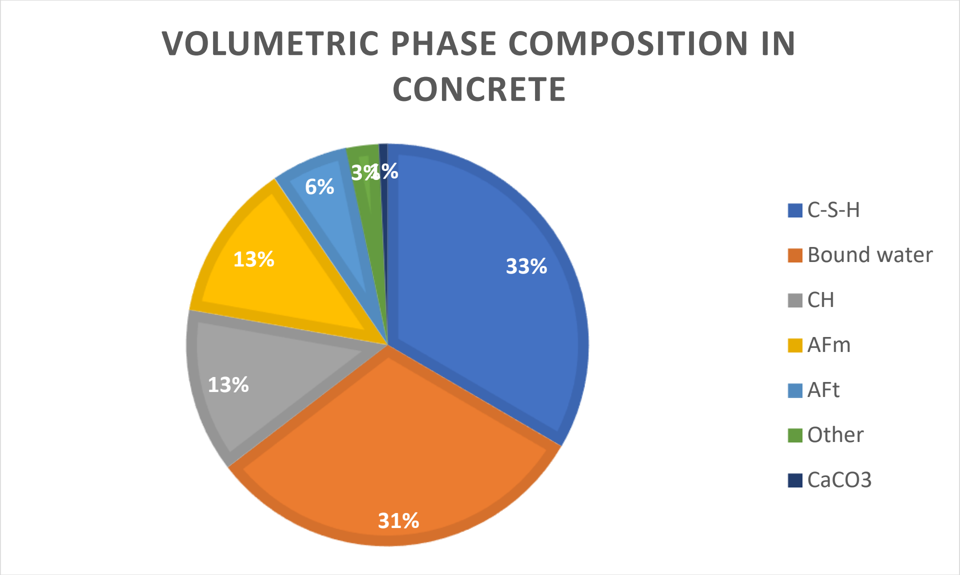

Figure 3: Phase composition of the Swedish conceptual model of concrete

2.1.2 Superplasticizers

Superplasticizers (SPs) are organic polymer additives in liquid state used for increasing the workability of concrete. Sulphonic acid groups are attached at regular intervals to the polymer chain. Its purpose is to disperse the cement paste during the setting (flocculated -> dispersed), reducing the amount of water needed which enhances the compressive strength property of concrete. SPs are polymers of which the polycarboxlyate-type (PC) is the most popular (Yamada, et al., 2000). Polycarboxylate type plasticizers are known to enhance flow behaviour and viscosity of the cement mixture. Other types of superplasticizer are suplhonated naphthalene-formaldehyde condensates (NS), modified lignosulphonates (LS) and sulphonated melamine-formaldehyde condensates (MS). The polymeric structures are illustrated in Figure 4.

Superplasticiser TM OFT-II B84/39 CON. 35% (BT-SPL) TM is used for the concrete samples and its application is designed for the production of concrete with a low water-cement ratio while improving workability and compactness (Tillman, 2016). Its maximum alkali content (Na_2O equivalents) is set as 8.5% & maximum chloride content as 0.1%. More information can be obtained from NEN-EN 934-2:2009+A1:2012 (European standard).

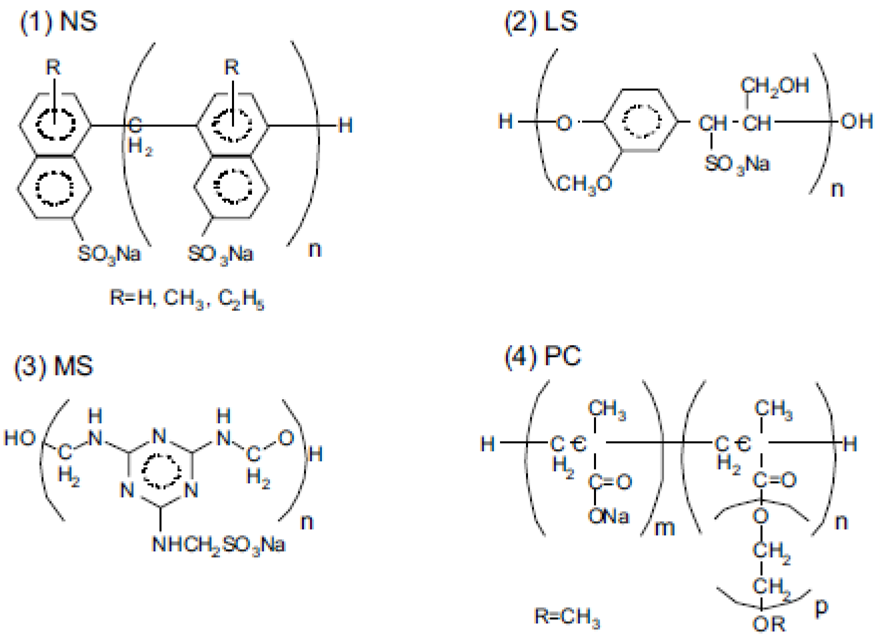

Figure 4: Structural polymeric formulae of common superplasticizers (Luna, et al., 2006)

2.1.4 Aggregates

Cementitious materials contain aggregates which have the role of a structural filler. The durability, mechanical strength, density and shrinkage are a few properties affected by the choice of the aggregate. Choosing the right aggregate for encapsulation of nuclear waste is important. As cementitious materials should fulfil its incarceration purpose for at least 100 years. Deterioration of concrete can be limited by choosing aggregates that prevent internal reactions that would occur otherwise.

One example is limestone as aggregates for the encapsulation of depleted uranium (low-level waste). Depleted uranium (uranium oxide, U_3O_8) is mixed with Portland cement containing limestone as aggregate. In this composition, the limestone aggregates have a useful feature to react with traces of UF_6 and precipitate into stable minerals (Kienzler 2013: p.32), improving the overall incarceration endurance. Aggregates in concrete have sizes that vary from 0 to 20mm. Furthermore, to prevent alkali-silica reactions (more about this degradation phenomena in section 2.2.2) amorphous or reactive silica are avoided as aggregates in concrete for nuclear incarceration purposes. Quartz and limestone are commonly used aggregates, with grain size varying from 0 to 20mm.

2.2 Concrete degradation

The degradation mechanisms may be summarized as follows (PCA, 2002):

- Chemical attack
- Alkali-aggregate reactivity
- Restraint to volume changes
- Fire/heat
- Loss of support
- Corrosion of embedded metals
- Overload and impact
- Abrasion/erosion
- Surface defects
- Freeze-thaw deterioration

The type of deterioration that the concrete may undergo in the repository concept is limited to the first seven mechanisms, when the entire geological nuclear repository is considered. For the sorptivity measurements of manually degraded samples however, the first two mechanisms are relevant.

2.2.1 Chemical attack

This type of degradation considers the change in pH of the near environment of concrete due to the intrusion and accumulation of specific chemicals. The result is a chemical interaction which includes the dissolution of portlandite due to the intrusion of hydrogen ion, increase of concentration of calcium in the pore solution, formation of additional ettringite by sulphate attack and the formation of Friedel's salt by chloride adsorption in the C-S-H gel (Lin, et al., 2016). Thus, for these types of degradations, the hydrochemical environment of cement-based materials within the repository design is determined by the externally originating groundwater composition inducing chemical reactions that alter the mechanical stability and transport properties.

First form of chemical attack covered in this report is carbonation. In this form, carbon dioxide dissolves in the pore solution of the cement paste, producing CO_3^{2-} which will react with Ca^{2+} to produce $CaCO_3$ (calcite) (Lagerblad & Tragardh, 1994). This reaction consumes the calcium dihydroxide (CH) hydration product, according to:

$$Ca(OH)_2 + CO_2 = CaCO_3 + H_2O \qquad [1]$$

Once the $Ca(OH)_2$ is depleted, the calcium of C-S-H gel is consumed. The hydration products AFm and AFt also react to form carbonate phases. After complete carbonation, the end products are calcite, amorphous silica, hydrocarboaluminates and various Al- and Fe- hydroxides (Luna, et al., 2006).

In short term degradation, this type of deterioration should be considered as a surface attack, as a carbonation depth of 5 mm is calculated for an exposure time of 50 years (Tuutti, 1982). This poses an experimental challenge and is not considered in the experiments performed by the author of this report. It is however a detrimental degradation for the repository.

Second form is sulphate attack; this may be misleading as sulphates are already present in gypsum ($CaSO_4 \cdot 2H_2O$) which is one of the components of cement. During the setting of the cement paste, sulphates react and end up mostly in the AFm and AFt phases. If carbonate ions are present, minor amounts of sulphate ions may be bound to thaumasite. 'Sulphate attack' may be better expressed as ‘external sulphate attack’, where additional sulphates are introduced, as the term indicates, externally. This leads to reformation of gypsum and formation of additional ettringite, resulting in volumetric expansion, which induces fracture formations.

Additional ettringite formation, which is the degradation phenomena of sulphate attack, takes place according to the following reaction:

$$3CaO\cdot Al_2O_3\cdot 6H_2O+2Ca(OH)_2+CaSO_4\cdot 2H_2O+2(K,Na)_2SO_4+76H_2O \qquad [2]$$

$$= 3CaO\cdot Al_2O_3\cdot 3CaSO_4\cdot 32H_2O+4(K,Na)OH$$

Third form is chloride attack, where the chlorine ions bind to the hydration products, either physically (adhesion) or chemically (salt formation). Chloride ions in concrete remain in two forms, either as a free chloride in the pore solution or as a bound chloride in some form in the cement hydrates. After a year exposure of a Slite Std Portland cement to sea water, about 40% of the chlorides within the concrete is reported to be dissolved in the pore water and 60% bound to the hydration products (Lagerblad & Tragardh, 1994).

This form of chemical attack is in general unwanted as it creates the onset of depassivation of steel (reinforcement of concrete in structures), where Cl^-/OH^- ratio is reported to be the relevant parameter (Diamond, 1986). In structural designs, steel is used as a reinforcing material. Due to the steel not being a naturally occurring material under atmospheric conditions, it will try to revert back to its natural state, which is iron oxide. After the initial setting of concrete, the pH value of the concrete surrounding the metal is commonly between 12 to 13. At this pH values a thin oxide layer (passivating layer) forms around the steel which reduces the corrosion rate to an insignificant level. The corrosion rate is then typically 0.1 μm/year. The passivating layer is destroyed when due to other processes the pH value decreases and/or the chloride concentration increases to above the threshold. Contact between dissimilar metals, such as zinc and steel, also induces corrosion, which is called galvanic corrosion.

The binding capacity of chlorine by hydration products is an extensively studied phenomenon, as this is a form of retention prohibiting access to reinforcing steel. Formation of chloride complexes on the surface of C-S-H is reported to reduce the porosity (Kayyali & Haque, 1988). Another study revealed that if the concrete sample is immersed in a chloride solution long enough, the flow of the chloride solution becomes restricted (Midgley & Illston, 1984),

A comparison was made between whether chlorides that adhere on the surface of C-S-H sheets are leachable by water and ethanol. Findings indicate that chlorides interact with Ca^{2+} ions and OH^- groups to form oxychloride complexes which are leachable by water but not ethanol (Beaudoin, et al., 1990).

In 1994 a group of Swedish researchers created a conceptual model for long time degradation for concrete in a deep nuclear waste repository. Their findings in the influence of external intrusion of chloride ions are the retention in AFm phase $C_3A \times CaCl_2 \times 10H_2O$, which is a compound named Friedel’s salt. If the chloride content is increased and the product is kept at low temperatures, the AFt phase (trichloride) is stable. The chloride retention capacity of the cement paste is a function of OH^-, CL^- and SO_4^{2-}, as these ions compete for the same spot in the AFm phase group.

The degree of retention of Cl^- by C-S-H is reported to be a function of Ca/Si ratio in C-S-H and C-S-H concentration (Yoon, 2010). Initially the chloride ions adhere onto the surfaces of C-S-H and may be quantified by the zeta potential of C-S-H, which is a theoretical measure of the degree of coagulation of substances in dispersed colloids. For longer periods the chloride ions become chemically bound in C-

S-H. Formation of Friedel’s salt is related to the amount of unhydrated C_3A and C_4AF phases in the cement paste.

In 2005, Japanese researchers have reported that of the hydration products, the C-S-H and AFm show the most significant chloride retention (Hirao, et al., 2005). Two mechanisms of chloride binding are proposed, where the first being the formation of Friedel’s salt by the substitution of sulphate in the AFm phase group and the second being adhesion on C-S-H surface. AFt phase and $Ca(OH)_2$ show no chloride binding capacity, however at a high chloride concentration it is possible that AFt phase dissolves followed by Friedel’s salt formation, in accordance to the findings of the Swedes in 1994. Figure 5, adapted from the work of Hirao and others, indicate a significant increase of Friedel’s salt formation as the initial chloride concentration is increased. This result is obtained by exposing synthesized AFm phase to a chloride solution. The researchers reported a formation of Kuzel’s salt at lower chloride concentration and Friedel’s salt at higher concentration. The researchers have performed secondary electron imaging before and after the degradation by chloride ions and concluded that the AFm phase remain their plate-like structure after the exchange of sulphates with chlorides.

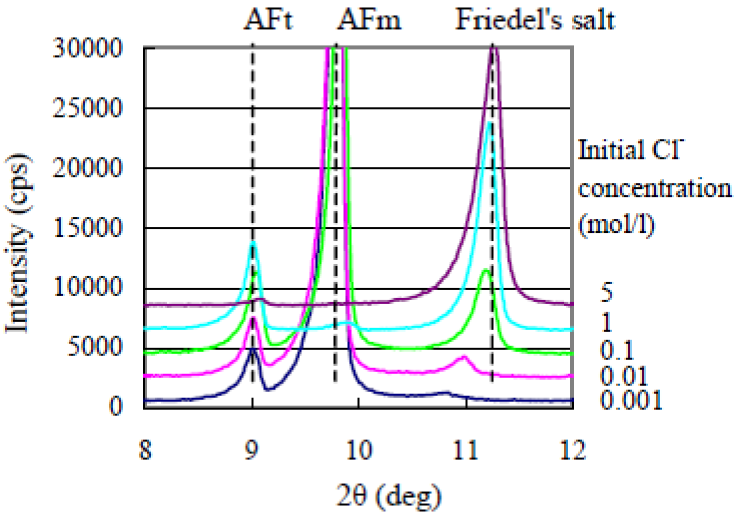

Figure 5: XRD patterns of AFm phase as a function of CL⁻ concentration (Hirao, et al., 2005)

Figure 6 shows the computationally obtained pH evolution of a concrete sample without aggregates & externally induced degradation. The graph is included with annotations indicating the physiochemical stage. At early time the pore water of the fresh cement has pH values over 12.5 with high K^+ and Na^+ concentrations. Next stage involves the dissolution of the CH hydration product, keeping the pH around 12.4. At stage 3 the CH product is dissolved and the CSH hydration product controls the chemical evolution. Upon complete degradation of CSH, major solid phases left are calcite and silica gel.

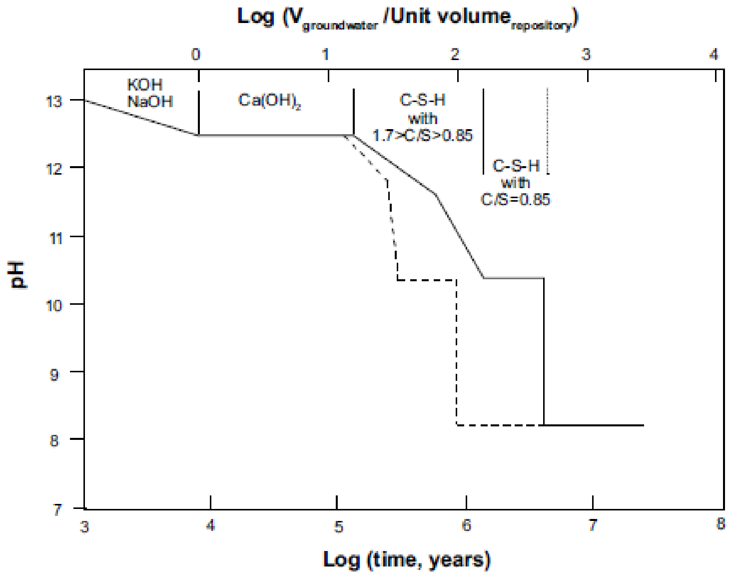

Figure 6: Modelled pH evolution of pore solution as a function of time (Atkinson, 1985)

2.2.2 Alkali-aggregate reactivity

This form of degradation involves reactions between alkali elements originating from the cement and the aggregates, in contrast with degradation by external elements. The reaction is of chemical and physical nature where an alkali-silica gel is formed by the dissolution of aggregates of which the reaction rate is related to the transport mechanisms of ions. The gel is able to take up water, which results in expansion and cracking of concrete. Diffusion and osmosis are the associated transport phenomena involved in the reaction between the pore solution and the reaction sites. Major factors of alkali-aggregate reactivity are the alkali concentration in the pore solution, mass fraction of the calcium hydroxide hydration product, reactivity of the siliceous component of the aggregates, pH of the pore solution and temperature (Lagerblad & Tragardh, 1994).

The alkali concentration in the pore solution originates from the alkali content of the cement. If this concentration is below 0.6 wt% Na_2O equivalent, no significant degradation is expected for up to 100 years, where no external source of alkali elements is assumed. Reactivity of the siliceous component of the aggregates is related to crystallinity and grain size (surface free energy). Quartz is crystalline and much less reactive than opaline silica, which is amorphous. This is due to the presence of weak bonds in amorphous solids facilitating the emergence of capillary pores inside the aggregate. Osmosis of alkaline solution into the pores then results in a higher dissolution rate of the aggregates.

Dissolution rate of quartz is highly dependent on the pH of the pore water solution. A pH threshold of 13.5 is reported below which little to no expansion takes place as a result of alkali-silica reaction (Struble, 1987). Figure 7 shows the relation of the dissolution rate of quartz vs pH. The data is obtained from computational modelling and the temperature condition is set as 70 °C.

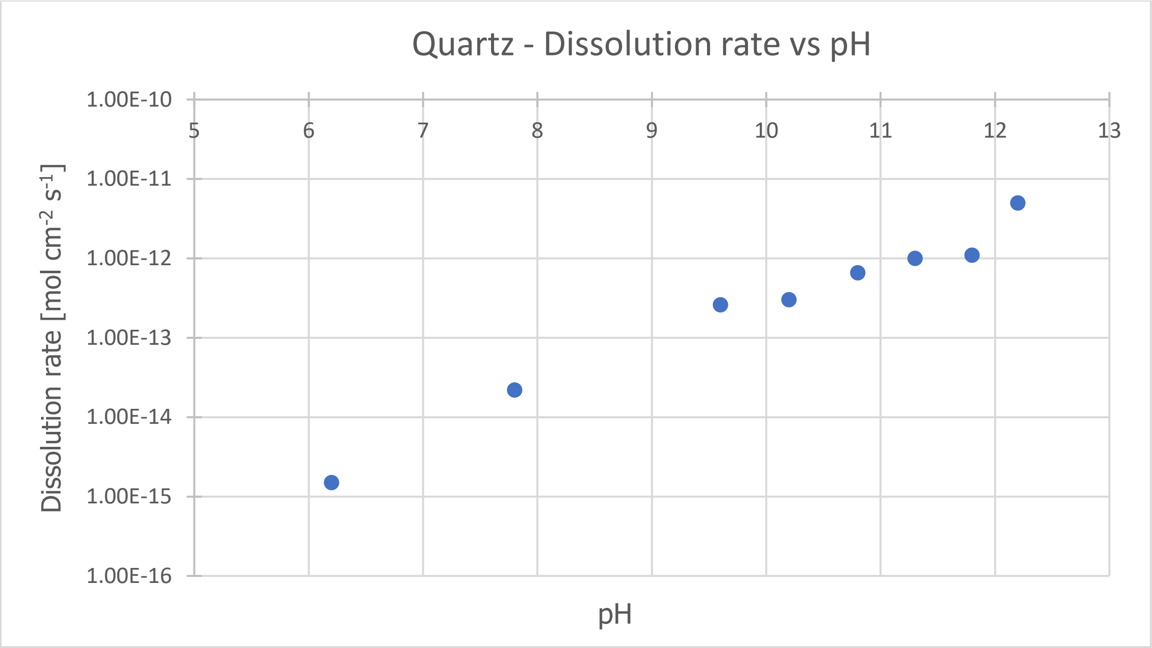

Figure 7: Dissolution rate of Quartz vs pH (Lagerblad & Tragardh, 1994)

In this model, the cement is Degerhamn Std P cement which has a pH value of 13.0. With the applied assumption that the pore solution will mix with groundwater, a reduction of pH is expected. Therefore, alkali-silica reaction will have little to no effect on concrete during the pre-closure period, which is defined to be up to 40 years (Lagerblad & Tragardh, 1994). The researchers used the Allard groundwater composition. As the concrete samples meet the criteria of minimum 0.6 wt% Na_2O equivalent, alkali-silica reactivity is difficult to reproduce in the lab. As such, this form of degradation is not further considered.

2.2.3 Sulphate attack and chloride attack

Short-term reproducible concrete degradation is limited to sulphate and chloride attack. Carbonation and alkali-silica reactivity are also responsible for deleterious deterioration, but require longer exposure up to 1 year. For that purpose, the impact of degradation on the sorptivity is limited to sulphate and chloride attack. This section covers literature findings on which chemical reactions may be expected when the concrete samples are degraded in the lab.

External sulphate attack involves the formation of AFt phases, where C_3A and CH hydration products are consumed. With the presence of carbonate ions, AFm phases may be formed as well. Sodium sulphate salt will be used to create a sulphate solution for the degradation of the concrete samples. Therefore, one of the expected chemical reaction is as follows:

$$3CaO\cdot Al_2O_3\cdot 6H_2O+2Ca(OH)_2+CaSO_4\cdot 2H_2O+2Na_2SO_4+76H_2O \rightarrow 3CaO\cdot Al_2O_3\cdot 3CaSO_4\cdot 32H_2O+4NaOH \quad [3]$$

Exact values of chemical reaction rate could not be found from literature. For complex chemical reactions however, it is customary to perform simulations. Researchers from Aberdeen created a model to determine the impact of geochemical components on phase stability and solubility of a C-S-H system. Na^+, K^+, SO_4^{2-}, Cl^- and CO_3^{2-} are the geochemical components in question. The obtained results include phase diagrams of the C-S-H system, for the case of SO_4^{2-}, the phase diagram is shown in Figure 8 (Stronach & Glasser, 1997). The sulphate concentration is set as variable, along with calcium and silicon concentration. The reason for using calcium and silicon concentration in the phase diagram is due to the fact that the Ca/Si ratio is the defining factor of the concrete performance. Due to complexity, in this concrete system the influence by aggregates are not considered.

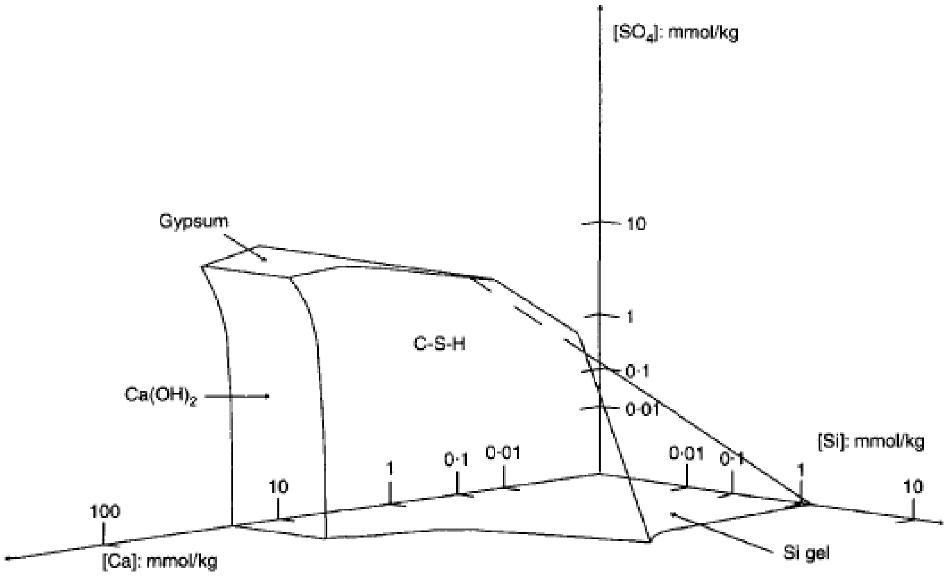

Figure 8: Modelled phase diagram of a computationally defined C-S-H system with variable SO42- concentration

The phase diagram provides insight to what degree sulphate attack plays a role when the concrete is exposed to groundwater containing boom clay. In order to determine this, the specification of the groundwater is necessary which is covered in chapter 3.

Exposure of concrete to a chloride solution lead to the formation of Kuzel's salt for lower concentration and Friedel's salt for higher concentration. Formation of the AFm phase kuzel's salt is reported to occur between 0 and 1 M of chloride concentration. At higher concentrations, up to 3 M, the AFm phase Friedel's salt is reported to be stable (Zibara, 2001). The AFm phase Kuzel's salt is expressed as:

$$2\mathrm{C_3A{\cdot}C\bar{S}+24H_2O+2NaCl} \rightarrow \mathrm{C_6A_2{\cdot}C\bar{S}{\cdot}CaCl_2{\cdot}24H_2O+2Na^{+}+Ca^{2+}+SO_4^{2-}} \qquad [4]$$

Friedel's salt is formed at higher chloride concentrations, but may also be formed when unhydrated C_3A and C_4AF are present, according to:

$$\mathrm{C_3A+2NaCl+Ca\left(OH\right)_2+10H_2O} \rightarrow \mathrm{C_3A{\cdot}CaCl_2{\cdot}10H_2O+2Na_{-}^{+}+2\left(OH\right)^{-}} \qquad [5]$$

From hydrated components, Friedel's salt is formed according to:

$$\mathrm{C_3A{\cdot}CaSO_4+12H_2O+2NaCl} \rightarrow \mathrm{C_3A{\cdot}CaCl_2{\cdot}10H_2O+2Na^{+}+SO_4^{2-}+2H_2O} \qquad [6]$$

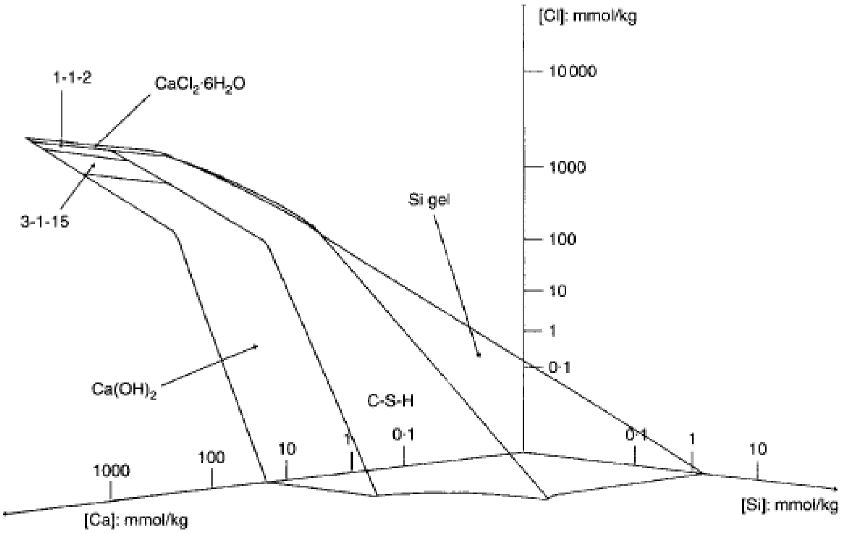

Figure 9: Modelled phase diagram of a computationally defined C-S-H system with variable Cl concentration

Similar to the phase diagram of a C-S-H system with variable sulphate concentration, this diagram provides insight to what degree chloride attack plays a role when concrete is exposed to boom clay pore water.

2.3 Boom clay

Millions of years ago, the Rupel formation was formed during the geologic Rupelian stage. Boom clay is a part of the Rupel formation, which is a marine clay. A marine clay implies that it was deposited as a seafloor sediment. Studies have shown so far that Boom clay is pyrite-rich. The clay occupies a wide volume beneath The Netherlands and Belgium. A facility to store nuclear waste at 500 meters depth, would be entirely immersed in this clay and surrounded by it for hundreds of meters.

The clay itself is a rather heavy, dark brown-grey substance. The composition consists of solid chunks connected to each other with a water layer (similar to grain boundaries in the microstructure of metals). In addition to the water layers, Boom clay contains water pockets that are rich in minerals. These water pockets may be considered as cavities/pores found in metals.

Figure 10 shows a rough sketch of the internal structure of bentonite. Bentonite is very similar to Boom clay and the channels of water act as a pathway for the radionuclides. The compounds in the water pockets are in equilibrium with the solid phase. Calcite, quartz and feldspar are present in the water pockets. The solid phase belongs to a hydrous alumina-silicate group.

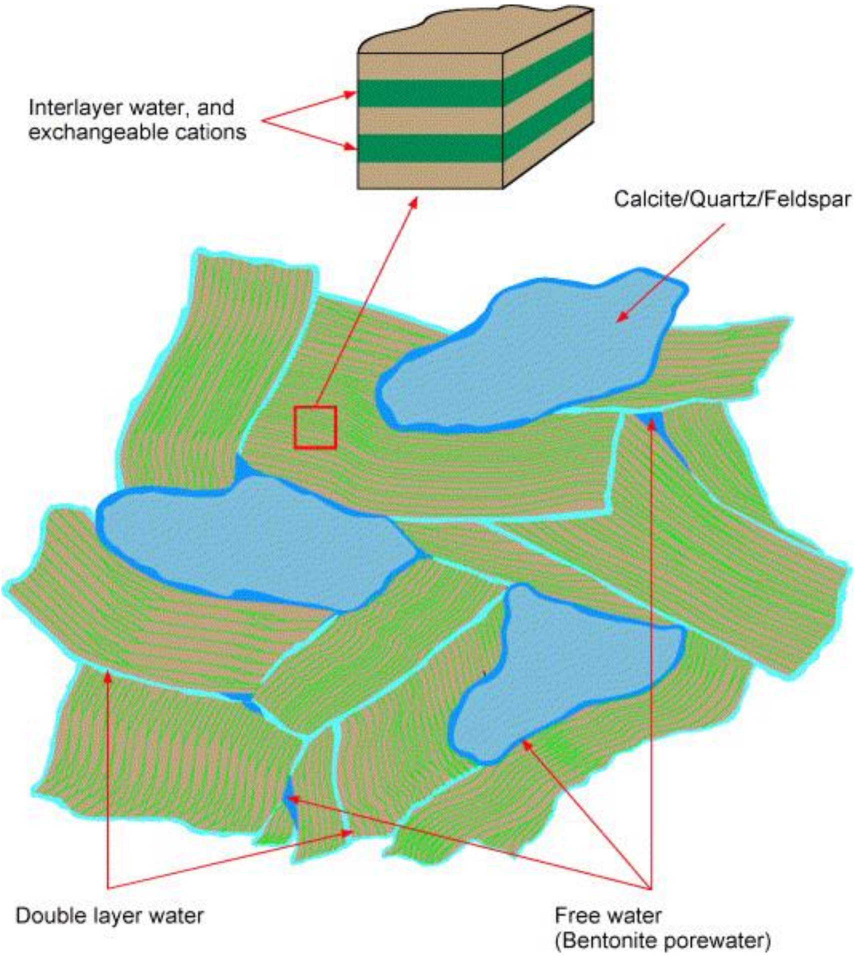

Figure 10: Sketch of the internal structure of bentonite with pores and double layer water.

Silicate layers are dominantly present in the solid phase, which consist of sheets of tetrahedrally co-ordinated Si and Al (T-sheet) bonded to sheets of octahedrally co-ordinated cations (O-sheet). The T and O sheets form up pairs that can be OT-layers (1:1 structure) or TOT-layers (2:1 structure).

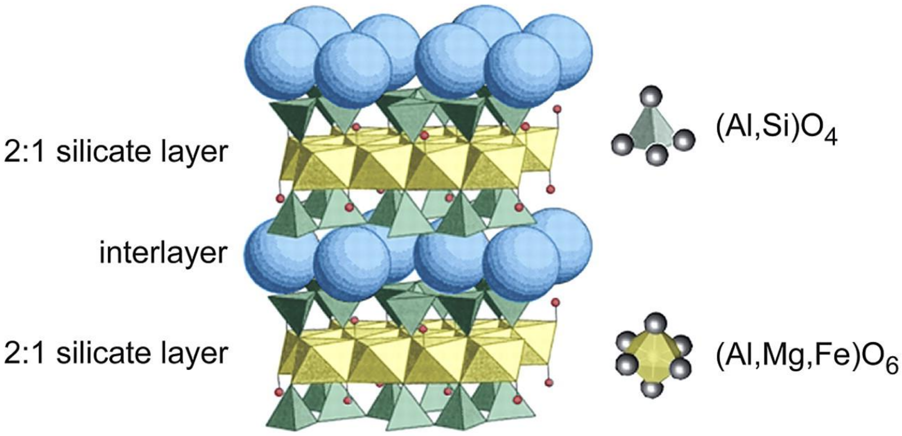

Figure 11: microstructure of bentonite clay in a TOT-layer structure. Blue sphere represents pore water, green tetrahedrons Si and Al (T-Sheet) & yellow octahedrons Al, Mg and Fe cations (O-sheet)

Figure 11 shows a TOT-layer structure which occurs in bentonite. Similar arrangements occur in various types of clay, including but not limited to kaolinite and smectite. The T and O sheets are considered to be the building blocks of clay.

2.4 Sorptivity as a transport parameter

The water retention ability of concrete materials is highly influenced by its porosity. Generally, there are 3 mechanisms that can describe the transport property of water through concrete, being diffusion, permeation and sorption. The driving force for diffusion is a concentration gradient. For permeation this is a pressure gradient and for sorption it is capillary suction.

For permeability studies, the samples are required to be completely immersed in water. After which a pressure gradient is applied. The rate at which the water moves through the specimen, is defined as the permeability. Sorptivity measurement is however an easier method to obtain a transport parameter, saving time and resources.

This property relates to the tendency of the medium to absorb and transmit a fluid by capillary forces. It is generally used to characterize the degree of capillary suction of unsaturated, hardened concrete/mortar. Permeability is a property that relates to the flow of water in a saturated medium under pressure, whereas sorptivity is a property that relates to the uptake and transmission of water in a dry medium. Sorptivity is measured as the rate of uptake of the fluid, where the following expression is used:

$$I = S\sqrt{t} \qquad [7]$$

Where I is the absorption in mm, S the sorptivity in $\mathrm{mm}/\sqrt{\mathrm{s}}$ and t the time in seconds. As it is rather difficult to reveal the distance of infiltration of the fluid I, the weight of the sample is measured over time instead. The weight change is then translated into distance with the use of the fluid density and surface of contact, as outlined in the standard:

$$I = \frac{m_t}{A \cdot d} \qquad [8]$$

Where m_t is the mass change in g, A the exposed area of the sample in mm^2 and d the density of water in $\mathrm{g/mm}^3$. The procedure to obtain sorptivity values is typically obtained by fitting the above expression in the plot of I vs $\sqrt{t}$ with least-squares linear regression analysis. This procedure is standardized by ASTM under the designation C1585. The plot of the data I vs $\sqrt{t}$ consists of two slopes, an initial slope and a secondary slope. The initial slope consists of data gathered up to 6 hours, whereas the secondary slope gathered after 1 day of exposure to the working fluid. The initial slope reflects the suction of the working fluid through capillary pores and the secondary slope reflects the filling of the pores. Two examples are shown in

Figure 12. The left graph is adapted from the standard test method ASTM C1585, where mass gain is measured over time. The right graph is adapted from a publication by Culligan and others, where a different experimental set-up is compared in determining the sorptivity (Culligan, et al., 2005). The experimental set-up makes use of a horizontal infiltration apparatus, to examine the applicability of moisture diffusion for liquid infiltration prediction in soil.

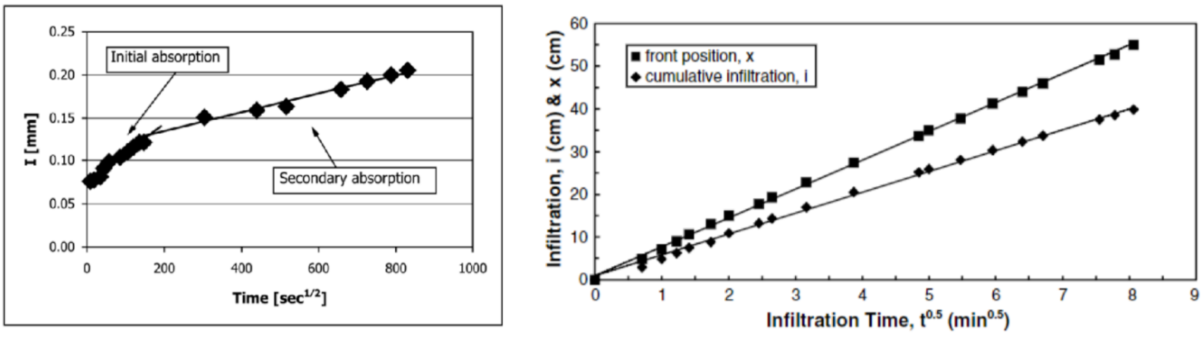

Figure 12: Sorptivity graphs. Left: ASTM C1583-13 standard. Right: Sorptivity research data on dry-soil by Culligan and others.

The currently available experimental set-ups are not suitable to perform permeability measurements. There is no apparatus that allows the presence of a pressure gradient of the concrete/mortar specimen. Furthermore, permeability is a transport parameter that remains valid when the specimen in question is saturated. At complete saturation, the suction exerted by a material is reduced to zero, thus the permeability yields no insight about the driving force by capillary flows (Hall, 1989). Sorptivity measurement has the main benefit to obtain a transport parameter which is relatively easy, time- and resource efficient to obtain.

It is theoretically possible to obtain sorptivity by the use of x-ray radiography, as outlined in the next section of this chapter. The validation of the obtained sorptivity parameter is done by additionally performing the standard test method according to ASTM C1585-13. This enables the accuracy testing of x-ray imaging as well as exploring the limits.

2.4 X-ray Imaging

An x-ray radiograph provides attenuation data of the material that is measured. The presence of water will result in an increased attenuation. Quantifying this increase results in the determination of the water content. A visual representation of sorption is shown in Figure 13 *(Belleghem, et al., 2016)*. The mortar sample were prepared using ordinary Portland cement with a water to cement ratio of 0.50 and a sand to cement ratio of 3. The grain size of the sand ranges between 0 and 2mm. The drying procedure for this sample is in accordance with NBN EN 13057.

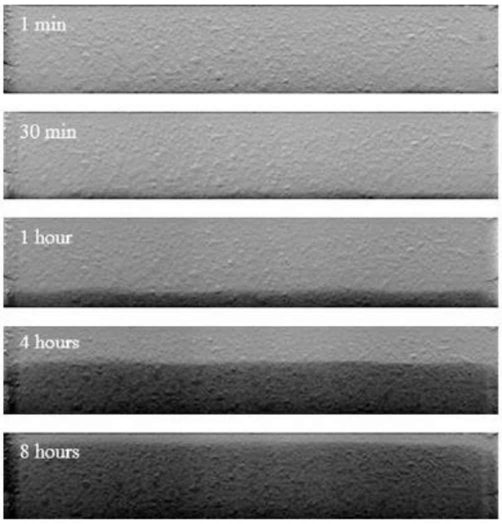

Figure 13: Transient water profiles obtained with x-ray radiography

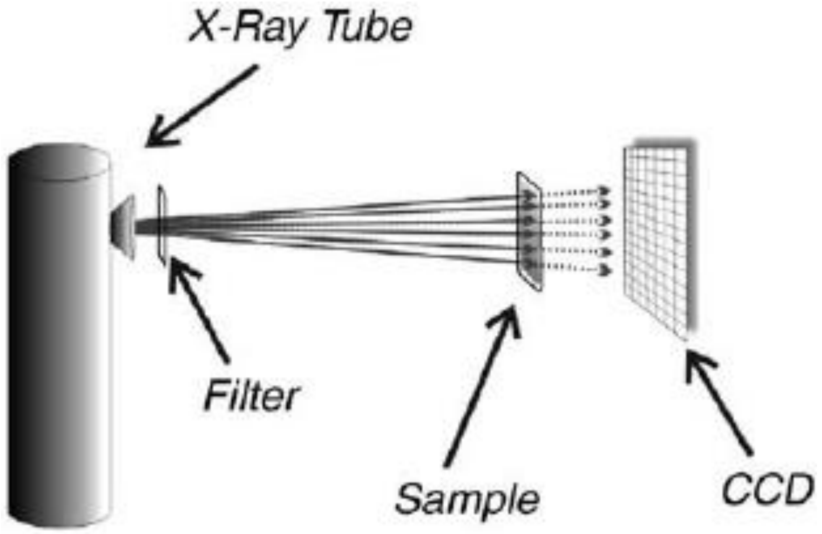

Figure 14: Schematic overview of an x-ray imaging set-up

Much work has been done in revealing water uptake in concrete. This served as a starting point for obtaining the sorptivity and the visualization of water migration through the concrete samples. This has been done for both non-degraded concrete samples and degraded concrete samples.

X-ray imaging is a non-intrusive technique available at the Reactor Institute Delft. Philips MSC 321 generates x-rays to which concrete samples are exposed to. The x-rays are consequently recorded with Medipix QTPX-262k camera. In essence, the degree of attenuation is measured. Using the Beert-Lambert law, the cross section is obtained:

$$I(x,z,t) = I_0(x,z,t)e^{\sum_i -(\mu \cdot d)_i} \quad [9]$$

Where:

- I : Measured intensity $\mathrm{cm}^{-2}\mathrm{s}^{-1}$
- I_0 : Measured open beam intensity $\mathrm{cm}^{-2}\mathrm{s}^{-1}$
- μ : Cross section cm^{-1}
- d : Thickness cm

The path through which the radiation attenuates may contain multiple elements, which is why the summation is used. For the measurements used, the equation reduces to:

$$I = I_0 e^{-\mu_{Al} d_{Al} - \mu_c d_c - \mu_Q d_Q} \quad [10]$$

Where the cross section and thicknesses of the aluminium sample container, concrete sample and water are considered. The cross section of the aluminium and water is derived by performing separate measurements, where only the element in question is measured. By manually measuring the thickness, its cross section can be calculated. The findings are in agreement with literature data. Following this procedure, the water thickness can be calculated for each pixel. Choosing a vertical line across the water front, allows the representation of the water thickness as a function of position. The measured water thickness is divided by the total thickness, resulting in water content [%]:

$$\theta = \frac{d_Q}{d_{Total}} \qquad [11]$$

Where:

- θ: The water content [%]
- d_{Total}: Total thickness of material through which radiation is attenuated [cm]

The water thickness is obtained by rewriting equation 10:

$$d_Q = \frac{-\left(\ln\left(I/I_0\right) + \mu_c d_c + \mu_{Al} d_{Al}\right)}{\mu_Q} \qquad [12]$$

The value $e^{-\mu_{Al} d_{Al} - \mu_c d_c}$ is obtained by selecting a region in the concrete of a sorption image where no Milli-Q is present and dividing the values with the corresponding open beam values. The cross section of Milli-Q is obtained from literature, allowing the determination of water thickness and thus the water content. By measuring the water content evolution over time, it is possible to obtain the sorptivity of the concrete specimen whilst imaging it.

2.5 Neutron Imaging

Neutron imaging provides two- or three-dimensional images of the internal structure of a bulk material. In addition to imaging, neutrons are used for diffraction and scattering experiments. Contrary to x-rays, neutrons do not have an electronic charge and thus interact negligibly with electrons. With x-rays the attenuation coefficient increases with the atomic number of the imaged substance. Whereas for neutrons the attenuation coefficient is highest when elements that are similar to that of neutrons are imaged. Since x-rays do not carry mass, but neutrons do, the interaction with hydrogen is quite strong as their masses are similar (billiard ball effect).

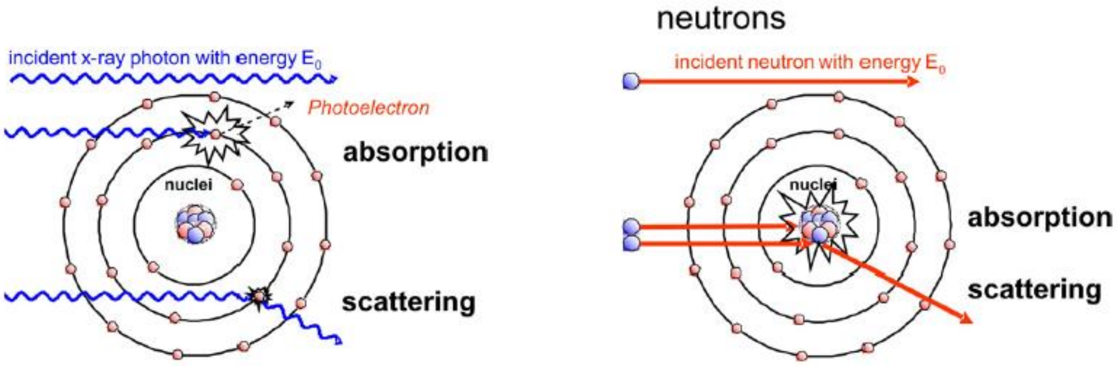

Figure 15: x-rays interact with electrons (left) whereas neutrons interacts with the nuclei (right) (Strobl, et al., 2009)

Figure 16 shows the attenuation coefficient vs atomic number chart for thermal neutrons and x-rays. Note the high attenuation coefficient of Boron for neutrons. Boron-rich rubber placement mats are widely used shielding materials against neutrons, whereas for x-rays lead blocks are used.

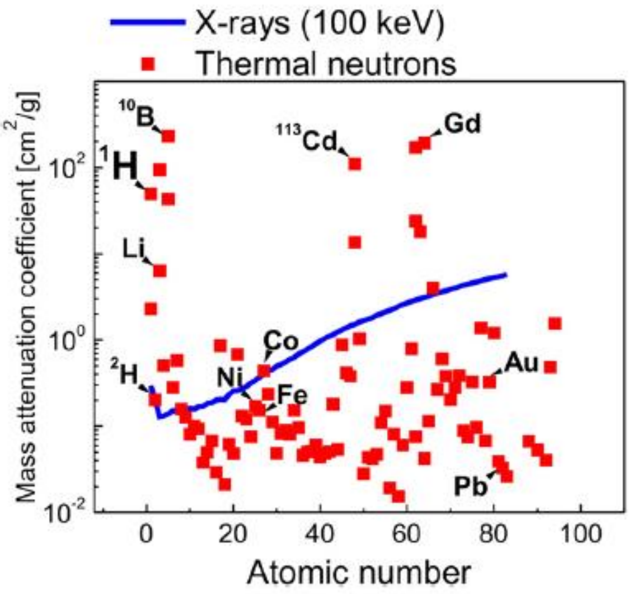

Figure 16: Attenuation coefficients for thermal neutrons and 100 keV x-rays (Strobl, et al., 2009)

The imaging of a material using neutrons is quite similar to that of x-ray imaging. Firstly, an open-beam measurement is carried out to determine the open beam intensity I_0. This is necessary to make use of the Beer-Lambert law for intensity attenuation, described in the previous section. Afterwards the material is placed on the rotor stage and a tomography is carried out. The rotor stage rotates the material in steps to record projects at different angles. The creation of an image from the data obtained from the cross-sectional scans of the sample is done with the Radon transform. For further theoretical details, the reader is advised to read MSc Julius Huijts's Master's thesis[1] and the article by Strobl and others from 2009[2].

The generation of a neutron source can be realized with a nuclear fission process in a nuclear reactor. Alternatively, a spallation neutron source is used for the generation of neutrons. This process involves bombarding liquid mercury with high-energy protons. Spallation releases neutrons, which are slowed down in a moderator. Liquid deuterium or water are often used as moderator for neutrons. Slowing down neutrons is preferred as it shows more interaction with samples for imaging purposes[3].

The detection of neutrons directly is rather difficult. Instead of observing neutrons, they are first converted to visible light using a scintillator. The resulting photons (in visible light energy spectrum) are then recorded with a conventional camera. The quality of the scintillator plays a major role in the highest achievable resolution of the images. A thinner scintillator will reduce the conversion rate of neutrons to visible light which in turns require a longer exposure time. That is why a trade-off exists between the thickness of the scintillator and permittable exposure time of the camera.

Other methods to increase the resolution of the image is to increase the distance of the sample to neutron source and minimize the distance of the sample to the detector (Huijts, 2014).

---

[1] Paving the way for a neutron imaging setup in Delft, Julius Huijts, 2014

[2] Advances in neutron radiography and tomography, Journal of Physics D: Applied Physics, Volume 42, doi: 10.1088/0022-3727/42/24/243001

[3] Oak Ridge National Laboratory, https://neutrons.ornl.gov/content/how-sns-works, accessed march 2019

3. Materials & Methods

3.1 Boom clay, concrete samples and tracers for imaging

This section covers all the materials used in the experiments in the study. The Boom clay and different types of concrete are provided by COVRA (contact person dr. E.A.C. Neeft). The tracer fluids for enhanced visualization in imaging techniques has been synthesized in the laboratorium of the Reactor Institute Delft. The next section, Methods, covers the instruments used to analyze these materials. The findings are reported in the Results section.

The clay and concrete samples that were provided by COVRA and used in this report, are specified in the OPERA reports (Verhoef, et al., 2014). The ingredients of the concrete samples in the tables are adapted from that report and from communications with dr. E.A.C. Neeft. The European cement classification system[4] is used for classification of the concrete samples. Information about the classification system, can be found in appendix B.

3.1.1 Boom clay

Boom clay has been provided by Covra for research purposes. A 3D reconstruction of boom clay has been created with the use of neutron tomography. Since the clay contains layers of pore water, revealing this internal structure provides insight and better understanding of migration behavior of radionuclides. The Boom clay is stored in a controlled environment to prevent oxidation and dehydration. Two methods to keep the clay sealed have been tried as shown in Figure 17, first being placement in an insulated food box and the other sealing the clay in an aluminum packet by melting the edges with a clamp that reaches high temperatures when pressed together.

Figure 17: Boom clay on a rotor stage for CT (left) | Boom clay in a metal-foil packet to avoid oxidation (right)

Short-term concrete degradation occurs in the presence of water. To gain understanding in which degradation phenomena and its deterioration rate prevail in the repository concept, it is required to study the composition of the groundwater. For the Netherlands, at 500 meter depth, the groundwater composition is known (Boom clay pore water), the composition is shown in Table 1.

---

[4] European Standard EN 197-1:2000 – Cement Part 1, June 2000, Brussels, European Committee for Standardization

Table 1 Synthetic Dutch boom clay pore water (Verhoef, et al., 2014)

Salt	**g/L water**	**Composition of a synthetic Dutch boom clay pore water**	
		Anions	***Mol/L water***
NaCl	24.476	**F^-**	9.16E-05
$MgCl_2$	5.137	**Cl^-**	5.57E-01
Na_2SO_4	4.107	**Br^-**	8.58E-04
$CaCl_2$	1.177	**SO_4^{2-}**	2.89E-02
KCl	0.712	**HCO_3^-**	9.10E-03
$NaHCO_3$	0.656	**I^-**	5.91E-06
KBr	0.102	***Cations***	***Mol/L water***
H_3BO_3	0.043	**Na^+**	4.85E-01
NaF	0.0038	**K^+**	1.13E-02
$FeCl_3$	0.011	**Ca^{2+}**	1.06E-02
KI	0.010	**Mg^{2+}**	5.39E-02
$AlCl_3$	0.0003	**Fe^{2+}**	6.86E-05
		Al^{3+}	2.59E-06
		Neutral species	***Mol/L water***
Silicafume (amorphous silica) EMSAC 500 S	Saturated	**H_2SiO_3**	6.96E-04
		$B(OH)_3$	1.95E-03

Due to the high presence of sulphates and chlorides, the degradations of sulphate and chloride attack have been chosen.

3.1.2 Gallery lining concrete - CEM II/A to B-V

The gallery lining concrete is what holds the repository together. Mechanical strength is important as its design should keep the structure intact for up to 140 years (Verhoef, et al., 2014). CEM II indicates a portland-composite cement is used, with a lower clinker fraction. Coarse aggregates of quartz are added to the cement mixture, together with Woermann plasticizer and superplasticizer. The size of the aggregates is large enough to be detectable with tomography investigations. However, the attenuation coefficient of silicon-based compounds is similar to that of calcium compounds, the expectation is that the aggregates will have a slightly different grey-shade. The composition is shown in Table 2.

In recent literature concrete compositions are often reported with the European cement classification system. Two concrete specimens both being labelled CEM III/A can still differ significantly in their structures. Additions of plasticizers and superplasticizers influence the porosity and are therefore mentioned in the specifications of the concrete samples.

The mass of unit implies amount of material used in weight for 1 cubic meter of concrete produced.

Table 2: Composition gallery lining concrete

Component	Type	Mass of unit	
Cement*	CEM II/A to B-V	386	kg m^{-3}
Water	-	125	kg m^{-3}
Plasticiser	Woermann BV 514	1.33	kg m^{-3}
Superplasticiser	Woermann FM 30	1.33	kg m^{-3}
Fine aggregate	Quartz sand: 0-2 mm	615	kg m^{-3}
Coarse aggregate	Quartz gravel: 2-8 mm	612	kg m^{-3}
Coarse aggregate	Quartz gravel: 8-16 mm	700	kg m^{-3}
w/c	Property	0.39	

The distinction between CEM II/A-V and CEM II/B-V lies in the portion of the wt% of clinker used. This sample is the result of adding fly ash to CEM I 42.5 R. How much fly ash is added is not accurate enough to classify this sample as either CEM II/A-V or CEM II/B-V. Therefore, CEM II/A to B-V notation is used. The -V indicates that fly ash was added. For details, refer to appendix B.

3.1.3 Encapsulation concrete - CEM III/B 42.5 LH/SR

This concrete sample provided by COVRA, servers the primary function to contain the nuclear waste. Two types of encapsulation concretes are designed, one for the containment of High Level Waste and the other for Low Level Waste. The difference is that in the HLW containment concrete recipe, coarse aggregates of up to 20mm are added, in addition to a polycarboxylic based plasticizer and a filler (Verhoef, et al., 2014). The sample provided servers the purposes to contain LLW and its composition is shown in Table 3.

Table 3: Composition encapsulation concrete for Low Level Waste (LLW)

Component	Type	Mass of unit	
Cement	CEM III/B 42.5 LH/SR	407-430	kg m^{-3}
Water	-	175-185	kg m^{-3}
Plasticiser	TM OFT-II B84/39 CON. 35% (BT-SPL)	3-5	kg m^{-3}
Fine aggregate	Quartz sand : 0-4 mm	819-972	kg m^{-3}
Coarse aggregate	Quartz gravel : 2-8 mm	891-763	kg m^{-3}
w/c	Property	0.43	

CEM III indicates that granulated blast furnace slag was added to the portland cement. /B designation indicates that the clinker mass fraction is between 20% and 34%. 42,5N designation indicates that an early compressive strength of ≥ 10,0 MPa is obtained after 2 days of setting, whereas 42,5R designation would indicate an early compressive strength of ≥ 20,0 MPa. LH is an abbreviation for Low Heat, which indicates lower heat generation during the process of hydration. The secondary result is low shrinkage, particularly important for large structure purposes. Finally, SR is an abbreviation of sulphate-resistant, a designation that indicates the formed concrete would delay sulphate-attack.

The exact composition of the granulated blast furnace slag fraction of the samples is not known. Researchers in Brazil analysed their blast furnace slag samples and reported the following composition: limestone (CaO, 43.5 wt%), silica (SiO_2, 35.8 wt%), alumina (Al_2O_3, 11.8 wt%) and magnesium oxide (MgO, 6.2 wt%) (Fredericci, et al., 2000).

3.1.4 Foam concrete - CEM III/B 42.5N LH/SR + Foaming Agent

The Foam concrete is rather similar to that of encapsulation concrete, with the difference being the addition of a foaming agent for volumetric expansion. The composition is shown in Table 4.

Table 4: Composition CEM III/B 42.5N LH/SR + Foaming agent, e.g. foam concrete

Component	Type	Mass [kg/m^3]
Cement	CEM III/B 42.5N LH/SR	408
Water		143
Superplasticiser	TM OFT-II B84/39 CON. 35% (BT-SPL) TM	4
Foaming agent +water	80/23	5
Fine aggregate	Quartz sand: 0-2 mm	1121
w/c	Property	

For this sample, the quartz aggregates are at most 2 mm in diameter. The samples are delivered in cylindrical shapes shown in Figure 18. The samples are used for neutron tomography studies to reveal and characterize the internal structure. X-ray radiography is used to visualize the water uptake which is used to calculate the sorptivity. ASTM standardized sorptivity tests (C1585-13) are done to determine the sorptivity in a universally accepted standard, in order to validate the x-ray results. These measurements are repeated for degraded samples, to quantify the influence of chloride and sulphate attack on the microstructure of the concrete.

Figure 18: CEM III/B 42.5N LH/SR + Foaming agent, foam concrete used for Neutron Tomography studies

3.1.5 Tracer fluids for imaging

Tracer fluids have enhanced brightness on radiographs, the purpose is to enhance the visualization of the water movement through concrete. In this research, the tracer fluids are dissolved in demi water. The concrete is put in contact with these mixtures, with neutron and x-ray imaging the capillary suction is then visualized. Two tracer fluids are used, namely cesium carbonate (Cs_2CO_3) solution and heavy water. Heavy water is expected to have a distinguishable attenuation effect in neutron tomography studies compared with the hydration products in concrete, as the hydration products have a large amount of hydrogen atoms.

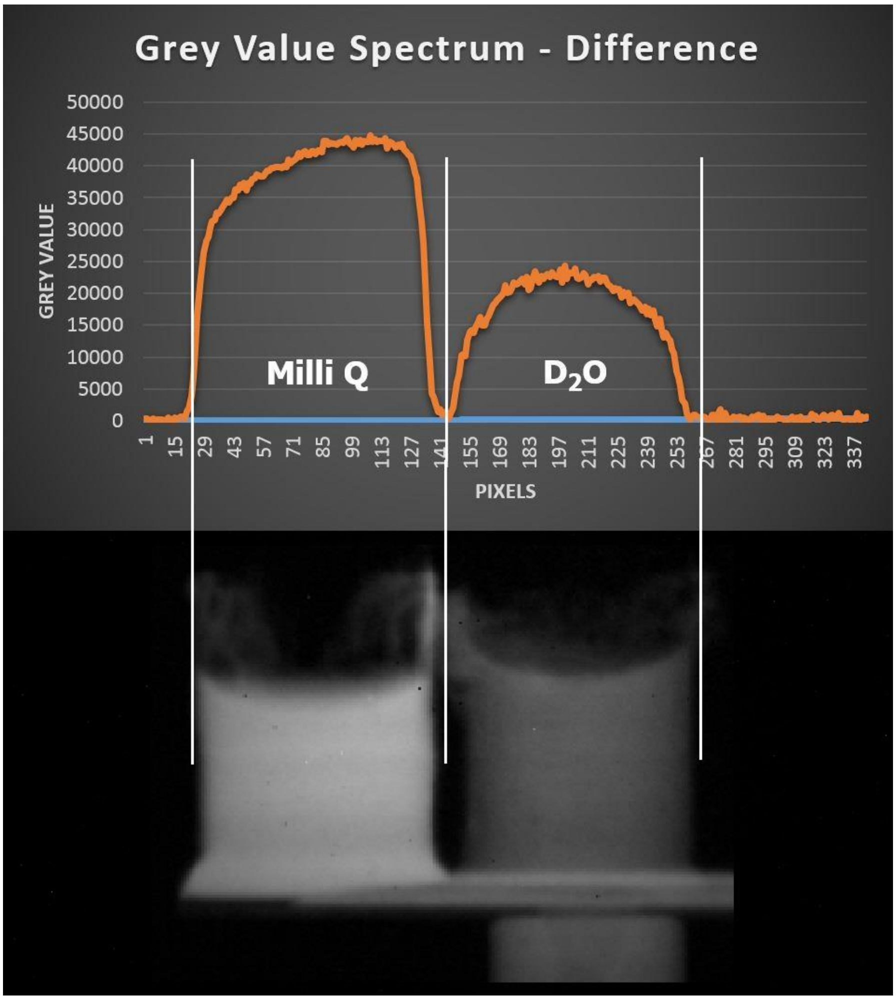

Figure 19: Upper: Grey value spectrum of demi water and D2O. Lower: Processed image showing the two Al foil cups containing demi water (left) and D2O (right), the rotation stage and the axis of the step motor.

Figure 19 shows a neutron radiograph of two small (1 cm width) cups made of aluminum foil which contain water (left) and heavy water (right). The output is a radiograph with a grey value, high value indicates strong interaction of neutrons with the material. A low grey value indicates of course the opposite. The blurry lines above the solutions is the Aluminum foil wrapping. The fluids and their foil-cups, are placed on the rotor stage. The rotor stage axis and plate are visible on the bottom side of the image.

In the analysis of the radiographs and tomography, image processing algorithms are extensively used to enhance the 3D render of internal structures of concrete and clay.

Cesium carbonate solution is used as a tracer fluid in x-ray imaging (radiography) studies. Preliminary testing with x-ray imaging has shown that simply using water yields inaccurate results, cesium carbonate as a tracer fluid has enhanced the images surprisingly well. Cesium carbonate interacts strongly with x-rays which makes the distinction with concrete more accurate.

3.2 Concrete degradation

Short-term reproducible concrete degradation is limited to sulphate and chloride attack. Carbonation and alkali-silica reactivity are also responsible for deleterious deterioration, but require longer exposure up to 1 year. As such an amount of time was not available, the impact of degradation on the sorptivity is limited to sulphate and chloride attack.

Concrete specimens are degraded in the lab to produce a set of samples:

1) Non-degraded concrete
2) Degraded concrete by sulphates
3) Degraded concrete by chloride

The degradation is done by immersing the samples in a 50 g/L Na_2SO_4 solution (ASTM C 1012-4) and, separately, 9.8 g/L NH_4Cl solution (Slomka-Slupik, 2009) for 1 and a half month. The sorptivity of all three specimens are measured by an ASTM standardized method and by quantification of the rate of water uptake with x-ray transmission imaging. The degradation continues for another month after which the measurements are repeated.

The concrete samples have been put in the sulphate and chloride rich solutions. The pH values have been measured every day, the exposure to the solutions lasted up to 6 weeks. Figure 20 shows the samples in a partially degraded state.

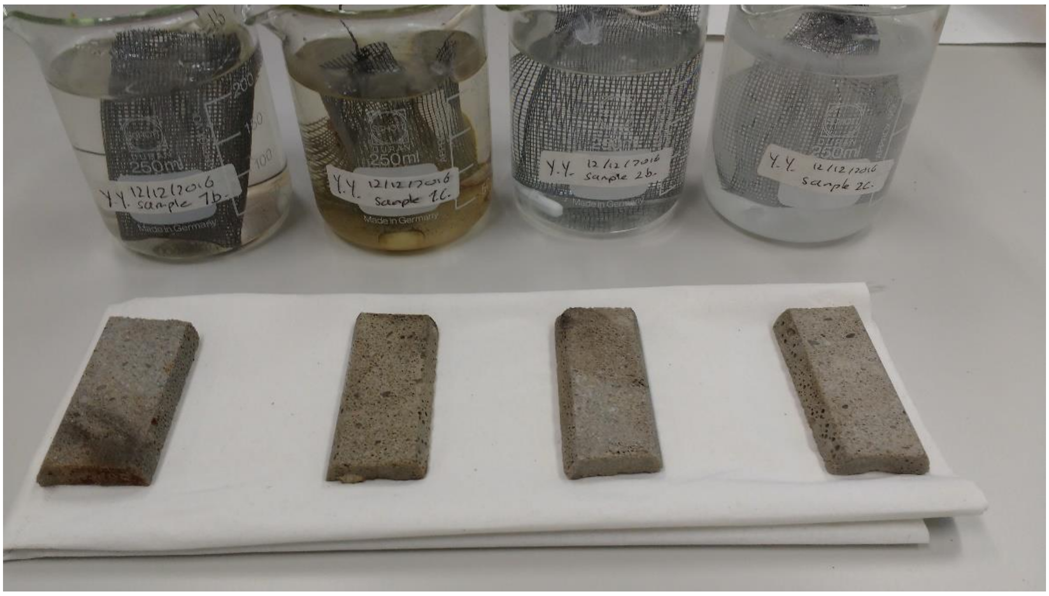

Figure 20: CEM-III Foam concrete samples cut in a rectangular shape and exposed to sulphate and chloride solutions

pH values are measured during the degradation process. Sulphates and chlorides will react with the concrete material to form crystals. In this process, the pH value will change. The rate at which the pH value changes indicates the degradation rate. pH values measured are reported in the next chapter.

Once degradation is complete, the samples are prepared for sorptivity measurements by x-ray radiography and ASTM sorptivity measurements. In the preparation, the samples are oven-dried until no mass change is observed[5]. This takes about 24 hours as a relatively low temperature (60 degrees Celsius) must be used to prevent damage to the internal structure of the concrete, as outlined in the ASTM standard for oven-drying of concrete materials for sorptivity measurements.

3.3 Tomographies and Transmission imaging

3.3.1 X-ray imaging

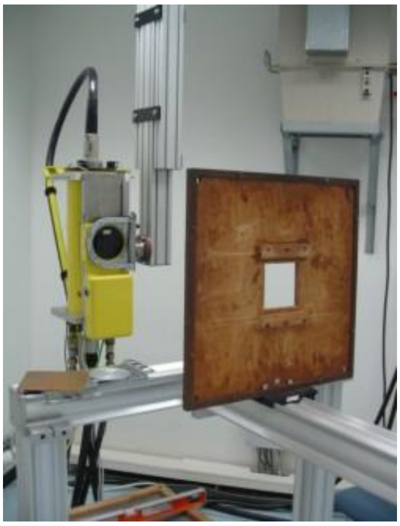

Figure 21: Philips MSC 321, X-ray generator

The X-ray generator used is shown in Figure 21 to the right. At the other end of the metal bar, the camera is positioned along with the concrete samples investigated. The set-up belongs to the radiation protection services of the Reactor Institute Delft. The use of this instrument requires permission and its availability is limited to working hours. The supplied voltage and current are manually configured in the operation room. Furthermore, filters may be added to filter out the lower energy x-rays, which poses usefulness if absorption is unwanted. As macroscopic cross sections are used in the derivation of water content, filters are not used in these measurements. The rate of absorption of water in concrete is investigated by measuring transmission images over time.

The camera used to measure the attenuated x-rays is manufactured by National Instrument. The model is Medipix QTPX-262k. Pixel size is 55 μm, where the sensitive area of the detector contains 512x512 pixels. This makes up for a sensitive surface of 2.8cm x 2.8cm. The detector can be operated in three modes: Counting mode, Time-Over-Threshold (TOT) mode & Time-Of-Arrival (TOA) mode. For the transmission measurements, the counting mode is selected.

By using equation 12 (page 25) and analyzing the data with Matlab, the rate of water uptake is calculated. This enables the determination of sorptivity. A measurement will take up to 4 days, to collect sufficient data the same way as it is required by the ASTM standard for easier comparison.

The Medipix camera is borrowed from the NERA department (dr. Zhou) and the X-ray generator from the radiation protection services (SBD). Raw data is processed with Matlab, the scripts can be found in Appendix A.

---

[5] ASTM Standard C1585, 2013, "Measurement of Rate of Absorption of Water by Hydraulic-Cement Concretes," ASTM International, West Conshohocken, PA, 2013, DOI: 10.1520/C1585-13, www.astm.org.

3.3.2 Neutron imaging

The nuclear reactor, Hoger Onderwijs Reactor (HOR), is a 2MW swimming-pool type reactor which is fed with low-enriched Uranium-235 (<20%) as fuel. In the event of a fission, Cs-140 and Rb-92 by products are created, on average 2.5 neutrons are released with an energy of about 2 MeV and an energy of 200 MeV is dissipated. The neutrons are released with a velocity of about 6% of the speed of light. The water surrounding the core acts as a moderator with which the neutrons scatter with. The resulting thermal neutrons are characterized as follows:

$$\langle E \rangle \approx 28\,\mathrm{meV}, \quad \langle \lambda \rangle \approx 15\,\mathrm{nm}$$

With the use of beam guides containing internal mirrors, the neutrons are guided towards instruments where they are utilized in measurements. Two beams are guided within the reactor hall where the flux is higher. Four beams are guided to the experimental hall where the background radiation is lower, but the neutron flux as well. The beam used for experiments in this work is collimated and then guided through a vacuum tube, to minimize scattering with air. The collimation ratio L/D is approximately 250. At the end of the vacuum tube, the neutrons reach the sample set-up and the neutron detector. The sample set-up and the detector are surrounded by sheets of boron rubber and then by lead blocks. Lithium and boron are known to be good neutron absorbers, lithium containing rubber does not emit gamma radiation whereas boron does. Lithium rubber is rather expensive which is why in this setup boron rubber is used in addition with the lead blocks to attenuate the gamma rays.

The neutron flux is $1.3 \cdot 10^{6}\ \mathrm{cm}^{-2}\ \mathrm{s}^{-1}$ and the neutron detector is a NeutronOptics camera. It is equipped with a LiF and a ZnS(ag) scintillator. The Li-6 acts to convert the neutrons to gamma rays, the ZnS(Ag) is a scintillator which converts the gamma rays to visible light. The light is then reflected towards a CCD camera (Sony ICX85AL0) with a resolution of 1360x1024 and pixel size of 0.11 mm.

The samples measured are emplaced on a rotation stage which is needed to perform a tomography. The step motor of the rotation stage is controlled with Labview to periodically rotate with a specified angle. The raw images are collected with the software Artemis Capture, which is manually synchronized with Labview. The labview script scans for an image file within a specified directory, upon detection of a saved image with a specific name, a signal is sent to the rotation stage. In all the measurements, a tomography over 180 degrees are performed with 0.225 degrees per step, resulting in 800 pictures per tomography. Additional to the tomography, dark images and empty beam images are recorded. Dark images imply the absence of neutrons by closing the shutter. This is useful as it allows the subtraction of background noise. Empty beam measurements imply the absence of only the sample, where the raw images are subtracted with the beam spot. The subtraction of background noise and beam spot are done with the software ‘Octopus’, which allows the user to perform reconstruction of the raw images with stacked slices as output. The stacked slices are then used for the following, but not limited to, image processing technique: surface rendering, interactive thresholding and porosity measurements.

Octopus comes with 3 separate modules: Reconstruction, Visualization (free) & Analysis. The only license the imaging department has is the reconstruction module, which can provide stacked slices. The visualization module is a free 3D rending software package, which can perform volume renderings with different camera settings. Typically, it stacks the slices together and allows the user to view the 3D object. The Analysis module is far more useful to the researcher. This module allows slice by slice studies with the use of powerful algorithms that enables the rendering of structures of interest only, such as pores.

Avizo is a commercial 3D analysis software for scientific and industrial purposes. The researcher imports stacked slices in the software and performs image processing tools, the output may be studied with various rendering tools and may be recorded as well. Avizo is found to be more user friendly which is why this tool is used to study the neutron imaging datasets. In addition to Avizo, the software VGStudio MAX from Volume Graphics is used.

With Neutron imaging and the tools for image processing, the internal structure of materials can be investigated. This is done extensively in the master's project, where different types of concrete samples are studied and the pore-size distributions have been obtained.

4. Results & Discussion

4.1 Neutron tomography

All the samples mentioned in the materials section have been analyzed with neutron tomography. The results for each sample are presented in the next sections. The camera set-up used in these experiments have been improved over time. The results of the improved neutron imaging setup are shown in section 4.3. The improved setup was made available near the final phase of this study. Therefore, the neutron tomography data of degraded foam concrete and non-degraded foam concrete were obtained with the improved setup which enabled the detection of more pores.

4.1.1 Boom clay

The clay provided by COVRA are stored in sealed packages to prevent oxidation. A fraction of this clay is removed and put in a smaller sealable package using a glove box. Another fraction of similar size is stored in a sealed glass container while entirely immersed in D_2O (purity 99.8%). Tomography's of both fractions are performed under limited exposure to air. The purpose of immersion in heavy water was to see to what degree the heavy water ingress in the clay was observable, by comparing the tomography data from the non-immersed clay with the immersed clay.

Figure 22 illustrates the volume render of the reconstructed dataset obtained from the tomography preformed on the boom clay which was immersed in D_2O. A tracer substance will not be visible directly, which is why image processing algorithms are implemented and used in imaging techniques.

Figure 23 shows one of these processing techniques, called 'interactive thresholding' in Avizo. Here a range of grey values is selected, any grey value outside this range is ruled out. If it is known what material exists in a particular spot, the grey value of that location may be used for threshold filtering, where all other grey values are removed. This is in particular useful to highlight something of interest within the material. The identification of grey value of interest is the variable that the researcher must test out in order to reveal insightful images. Boom clay is known to have an extremely low permeability coefficient of water.

Figure 24 shows the volume render of the other boom clay sample that has not been immersed in heavy water.

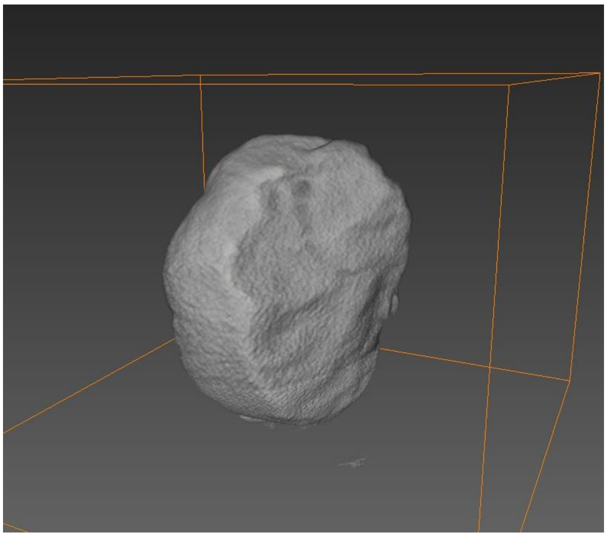

Figure 22: Volume render of boom clay, roughly 3cm in diameter

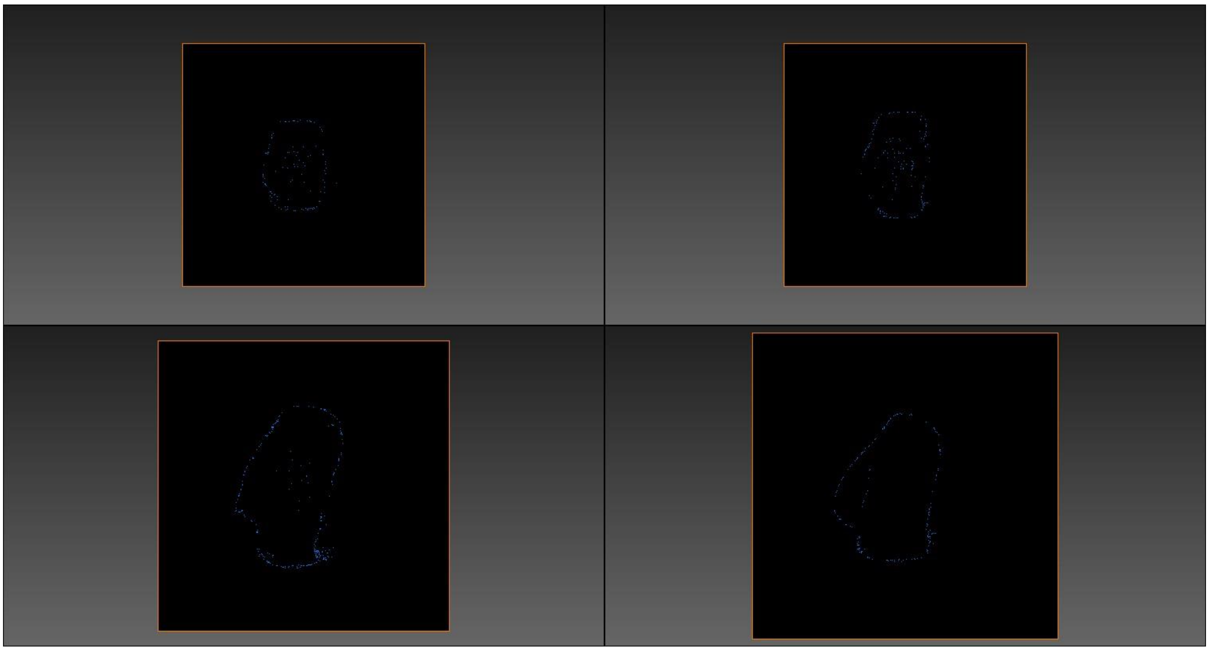

Figure 23: Grey value thresholding where the edges of the (immersed) clay sample is highlighted

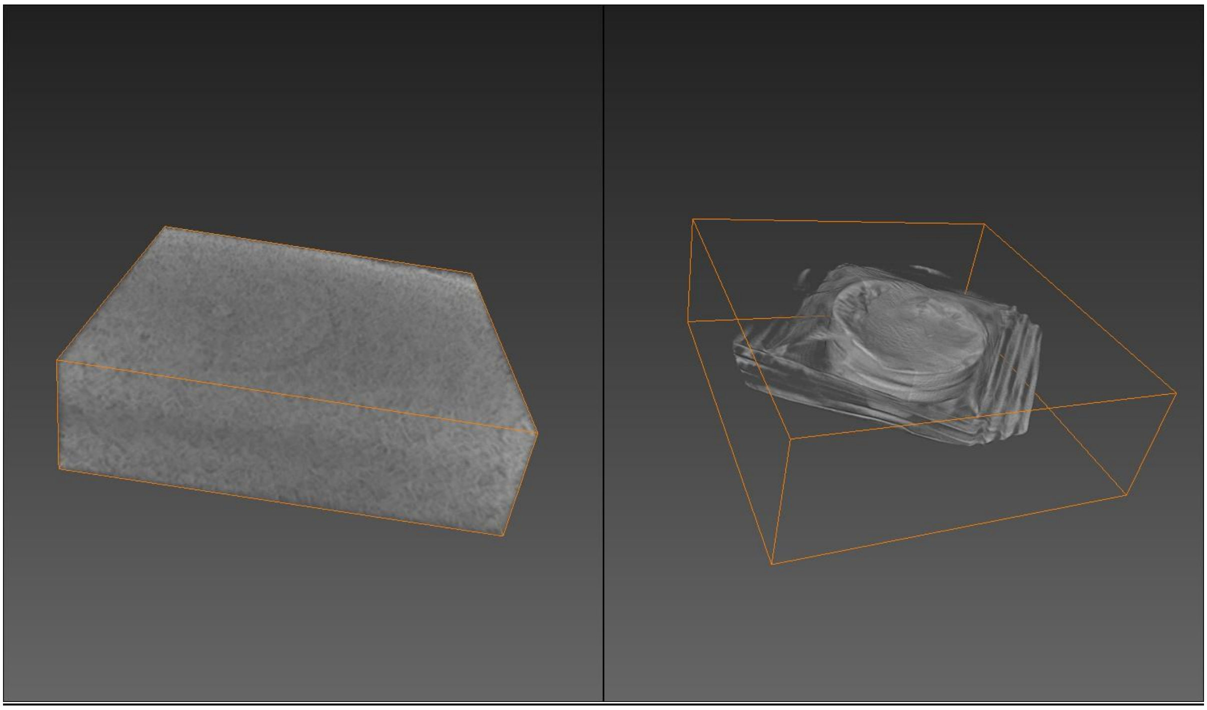

Figure 24: Boom clay that is not immersed; Right: the sealed clay sample. Left: Extracted sub volume

Both boom clay datasets (immersed & non-immersed) have been compared with each other, the edge of each sample was selected as area of interest, however no ingress of heavy water could be determined. The image thresholding of the edge of the samples have equal thickness. The reason is that it is very unlikely that the border between two voxels happens to be exactly the edge of the clay sample. The edge of the clay material will end up within the voxel. The grey value of that voxel will have the average value which is lower than the voxel grey value inside the clay but higher than empty space. In other words, the grey value transition when moving from empty space into the clay sample does not occur like a step-function does, but a steep smooth curve as an asymptote.

The microstructure of boom clay is described in chapter 2 could not be revealed with the neutron tomography setup. No water pockets were distinguishable from the rest of the material.

4.1.2 Gallery lining concrete - CEM II/A to B-V

The very first sample provided by COVRA is CEM II/A to B-V, an aggregate-rich sample, primarily to serve for mechanical support. Note that from Table 2 the size of the largest aggregates can be up to 16 mm. This specimen has not been conditioned in any way. As the first neutron tomography has been performed on this sample, the feasibility of the neutron tomography set-up has been tested. Figure 25 clearly visualized the aggregates within the sample. The stacked slices have been analyzed further using Volume Graphics software. Figure 25 is a slice from the 3D reconstructed object.

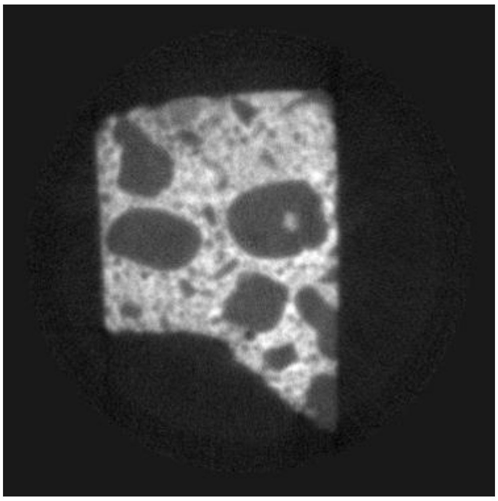

Figure 25: Cross-section of CEM II/A to B-V, gallery lining concrete

Figure 26 shows the concrete specimen in grey color rendered in 3D. The pores are highlighted in color ranging from blue to red. The color indicates the size of the pore, where red highlights represent the largest pore detected within this dataset. As there were few pores within the red region, most pores are colored blue to green, indicating that most pores are between 0.01 to 1.70 mm^3 in volume (0.22 mm to 1.20 mm in pore diameter). The pore diameter is the longest distance within a reconstructed pore. The pixel size is 110 μm for this set-up and connected cluster of minimum 4 pixels that are similarly dark is treated as the prerequisite for pore characterization. The smallest detectable pore is then 2 pixels which equals 220 μm, about 2 human hairs. Porosity data is shown in Table 5.

Table 5: Porosity data of CEM II/A to B-V, gallery lining concrete

Material volume	12083.45 mm^3
Pore volume	399.96 mm^3
Porosity	**3.31% ± 0.36%**

1590 pores have been detected with an average pore diameter of 1.10 ± 0.20 mm and an average pore volume of 0.60 ± 0.43 mm^3. The high error in the pore volume is explained in the next page.

Other researchers have investigated the porosity by Mercury Intrusion Porosimetry of a CEM II/B-V concrete sample, in 2004. They report a porosity of 7% 2 days after setting the concrete, 4.5% 7 days after, 4.2% 28 days after and 0.18% 3 months after (Dhir, et al., 2002). The obtained porosity in this study is 3.31% which is fairly in agreement.

In a more recent publication, porosity of CEM II/A-V with 0.40 w/c ratio, is reported to have a helium porosity of 24.6%, MIP porosity of 19.5% and water saturation porosity of 39.2% (Tracz, 2016). Methods used in their study are capable of detecting meso pores (2-50 nm) and macro pores (beyond 50nm). Water immersion porosimetry, as reported, introduces additional porosity.

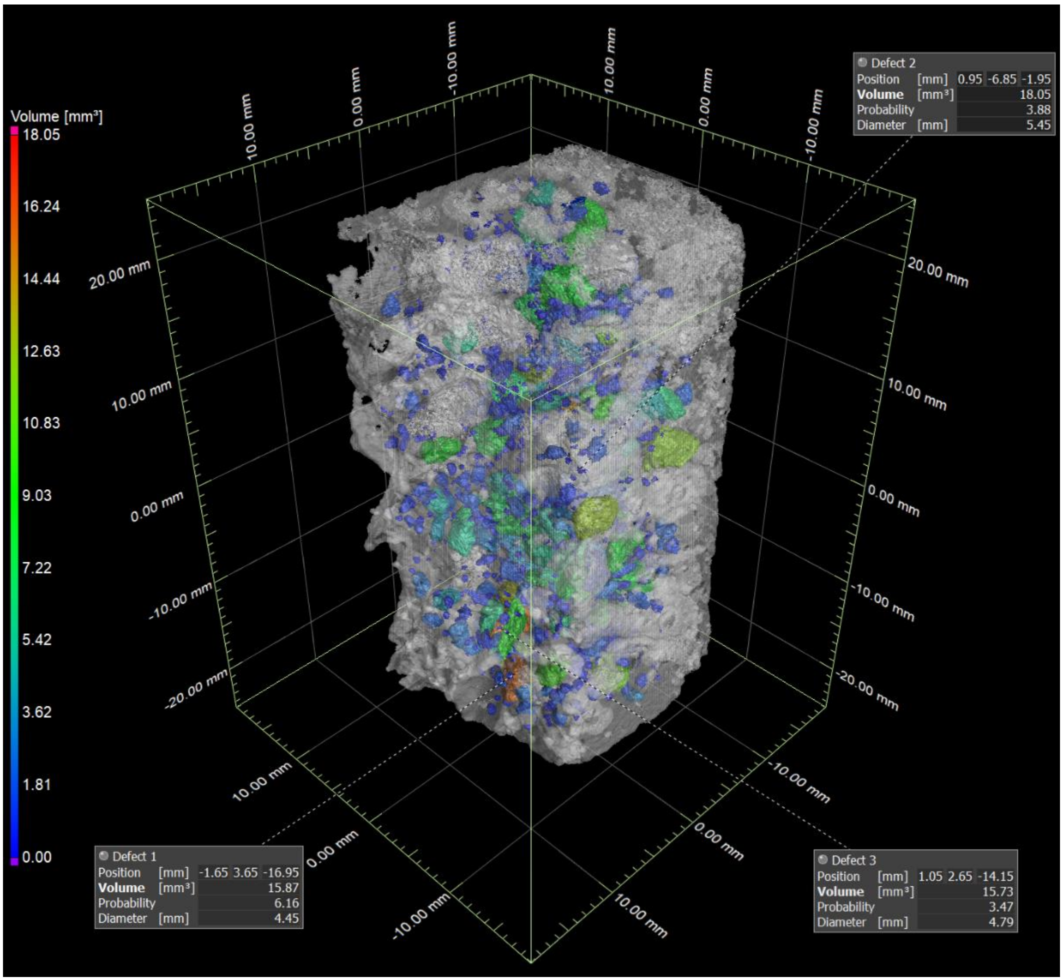

Figure 26: 3D Rendered visualization of CEM II/A to B-V, gallery lining concrete using Volume Graphics

The error in pore volume as a result of inaccuracy in measuring the scintillator dimensions is calculated.

The scintillator has the dimensions of 150 mm x 120 mm where the CCD array consists of 1360x1024 pixels. Assuming 0.5 mm read error (half of the smallest graduation), the error in pore diameter is:

$$\Delta E_{pixel} = \frac{0.5\ \text{mm}}{1360\ \text{pixels}} = 3.7 \cdot 10^{-4}\ \text{mm/px}$$

For 0.22 mm pore diameter, with η the number of pixels, the error in pore volume becomes:

$$\frac{\Delta V}{V} = \frac{\Delta L}{L} + \frac{\Delta W}{W} + \frac{\Delta H}{H} = 3 \cdot \frac{\Delta E_{pore}}{D_{pore}} = 3 \cdot \frac{\eta \cdot \Delta E_{pixel}}{D_{pore}} = \frac{2\text{px} \cdot 3.7 \cdot 10^{-4}\ \text{mm/px}}{0.22\ \text{mm}} = 0.01\%$$

For 1.20 mm pore diameter, the calculation yields:

$$\frac{\Delta V}{V} = 3 \cdot \frac{\Delta E_{pore}}{D_{pore}} = 3 \cdot \frac{\eta \cdot \Delta E_{pixel}}{D_{pore}} = 3 \cdot \frac{12\text{px} \cdot 3.7 \cdot 10^{-4}\ \text{mm/px}}{1.2\ \text{mm}} = 0.01\%$$

Thus, the aforementioned pore volumes with an error analysis become 0.01 ± 10^{-4} mm^3 and

1.70 ± 0.02 mm^3. The error in pore volume as a result of blurriness however dominate the error as a result of measuring with a ruler. Reviewing the stacked slices and zooming greatly in one of the pores, clearly shows that due to lack of spatial resolution the error in pore diameter is rather in the range of 3 pixels, i.e. $\Delta E_{pore} = 0.3\ \text{mm}$, highlighted in Figure 27. For small pores, the error becomes:

$$\frac{\Delta V}{V} = 2 \cdot \frac{\Delta E_{pore}}{D_{pore}} = 2 \cdot \frac{0.30\ \text{mm}}{1.2\ \text{mm}} = 50\%$$

And for larger pores, 18 mm^3 (= 2.62 mm) as highlighted in Figure 26, the error yields:

$$\frac{\Delta V}{V} = 2 \cdot \frac{\Delta E_{pore}}{D_{pore}} = 2 \cdot \frac{0.30\ \text{mm}}{2.62\ \text{mm}} = 23\%$$

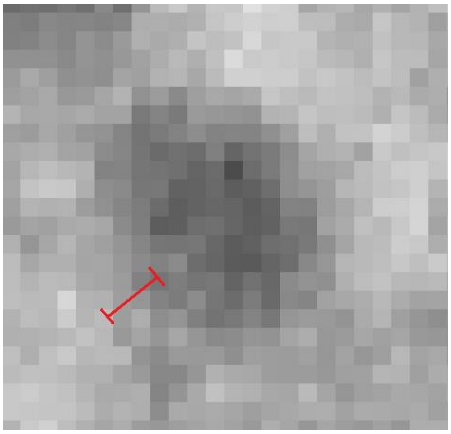

Figure 27: Detected pore in a slice from the Tomography of CEM II/A to B-V, gallery lining concrete

This experimental set-up is far from being as optimal as the experimental set-ups used later on in this study. Inaccuracy in this set-up primary comes from blurriness, which is introduced mainly by:

- Low collimator aperture diameter over sample distance ratio (L/D)
- Thickness scintillator, camera resolution & pixel size

It is clear that in order to compare the data with literature values, the spatial resolution of the pores need to be improved.

Figure 28 shows the pore size distribution of the gallery lining concrete obtained by analyzing the Volume Graphics data with Matlab. Noteworthy is the low amount of pore count, when compared to the datasets obtained in improved set-ups. Pores with volumes larger than 0.5 mm^3 are detected once or twice, whereas for smaller volume pores the count rate goes up to hundreds.

Figure 29 shows the sphericity of the concrete sample. The inaccuracy is well demonstrated as there is a big spread in sphericity for higher pore diameter detections.

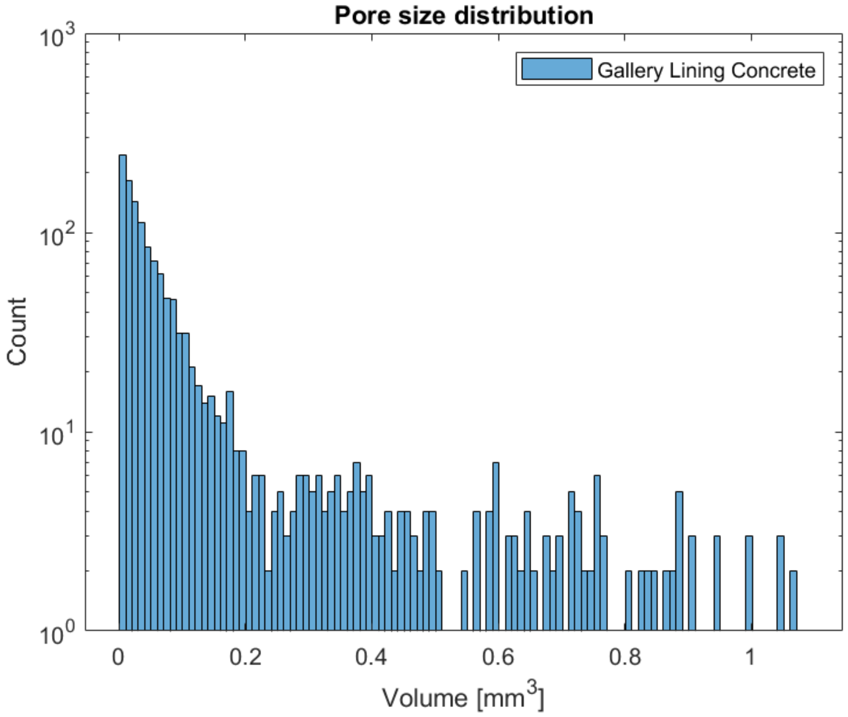

Figure 28: Pore size distribution of CEM II/A to B-V, gallery lining concrete

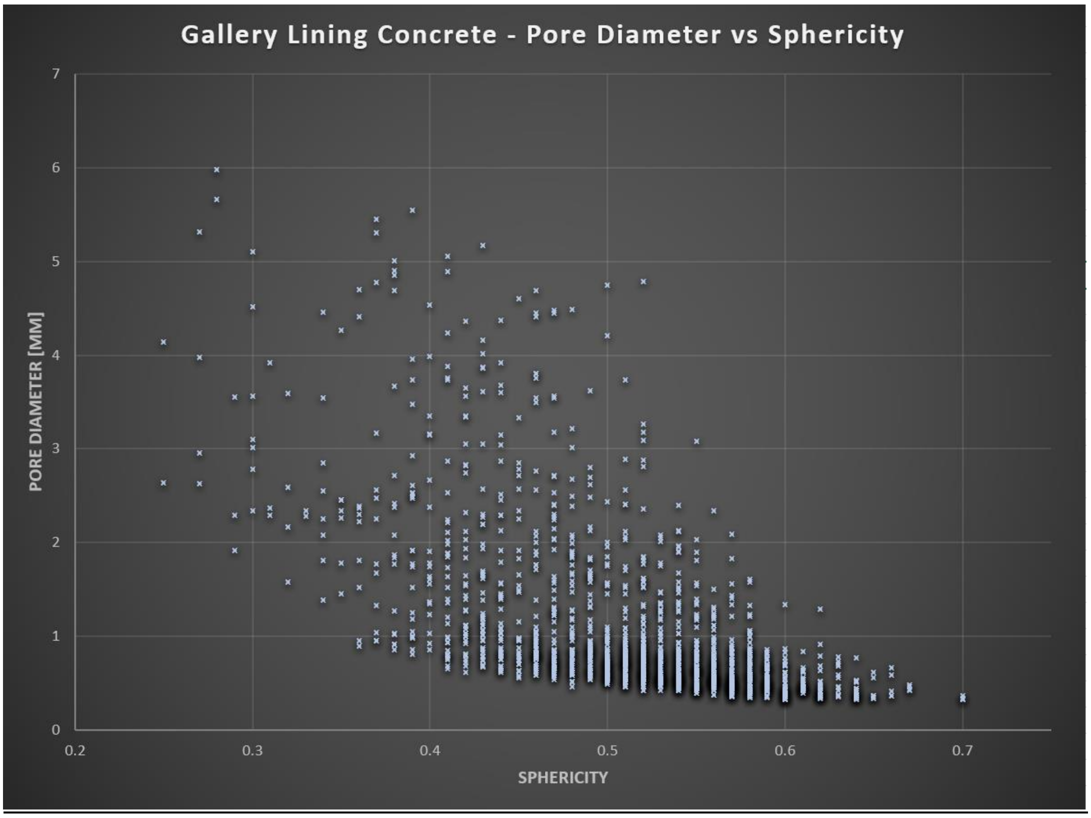

Figure 29: Sphericity of CEM II/A to B-V, gallery lining concrete vs its pore diameter

4.1.3 Encapsulation concrete - CEM III/B 42.5 LH/SR

The experimental set-up was improved by reducing the collimator-aperture over sample distance ratio (L/D). Temporal resolution of the dark measurement and open beam measurement was improved by taking the average of 10 recordings of the same area. The CEM III/B 42.5 LH/SR encapsulation concrete sample has been studied by performing a neutron tomography with these improvements. The images are reconstructed with Octopus Reconstruction, loaded in Avizo & Volume Graphics and further analyzed in Matlab.

The results for this sample are shown in Table 6, followed by statistics in pore diameter and volume. Next, some visualizations are presented with the procedure in how the data have been obtained.

Table 6: Porosity data of CEM III/B 42.5 LH/SR, encapsulation concrete

Material volume	14309.68 mm^3
Pore volume	93.18 mm^3
Porosity	**0.65% ± 0.07%**

232 pores have been detected where the average pore diameter is 1.47 mm and the average pore volume is 0.41 mm^3. After reviewing the stacked slices, an error of 1-pixel width is still present. Repeating the error analysis produces an error in pore diameter of 0.10 mm and in pore volume of 0.40 mm^3. The error for larger pores is much less, for the largest pore this yields 7.41 ± 0.15 mm^3.

A CEM III specimen of similar w/c ratio is investigated where the effective porosity is measured using water immersion porosimetry. A porosity of 12.5% is measured shortly after setting the concrete, which reduces down to approximately 4% after 1 month (Ortegaa, et al., 2014). The concrete sample used in this study however is designed to have a low shrinkage (LH). Additionally, the samples have been put on vibrating drums to reduce the amount of macro pores. The neutron tomography is a set-up viable to detect these macro pores, the ones that are detected in this study have failed to be extracted by the vibrating drums. Taking this in consideration, the measured value of 0.65% porosity for this sample is in-line with the findings by Ortegaa and others.

Figure 30 shows the volume reconstruction of the concrete sample. The rough surface of the concrete sample is recognizable and the rotor stage that it is placed on as well. On the right the output of grey-value thresholding is shown. The pores have been revealed, there is a strong diversity in pore size, however the number of pores is extremely low, as one would expect from concrete that is used to incarcerate nuclear waste.

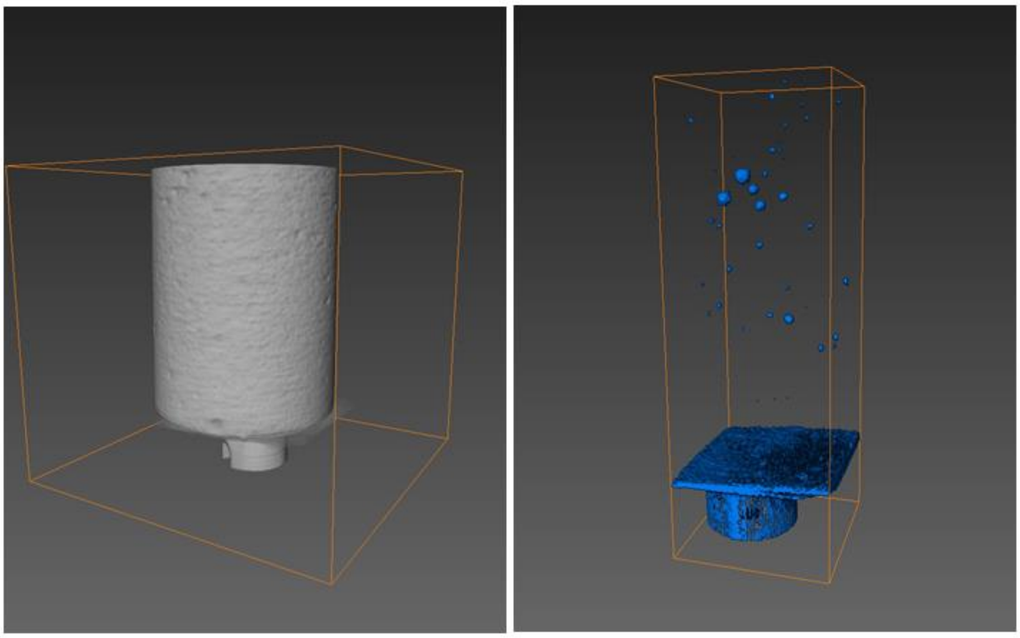

Figure 30: Waste concrete (not immersed sample). Left: volume render of reconstructed slices. Right: interactive thresholding applied, voids visualized among with the rotor stage and step motor axis.

Figure 31 shows the encapsulation concrete further processed. Top left image shows a volume extraction, the cross section is shown on the top right image. Before pores are visualized, the inner volume is extracted. Pore size vary greatly, as highlighted in Figure 32.

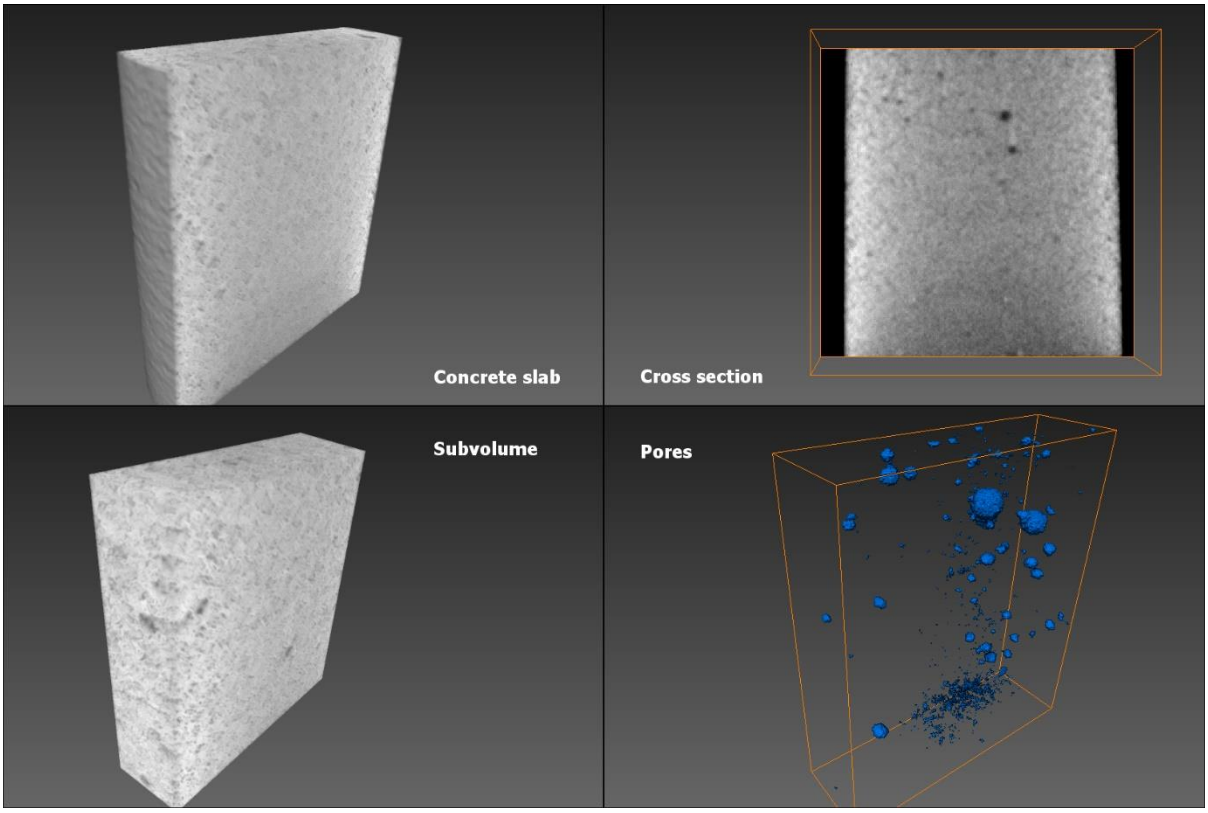

Figure 31: Encapsulation concrete further analyzed with image processing

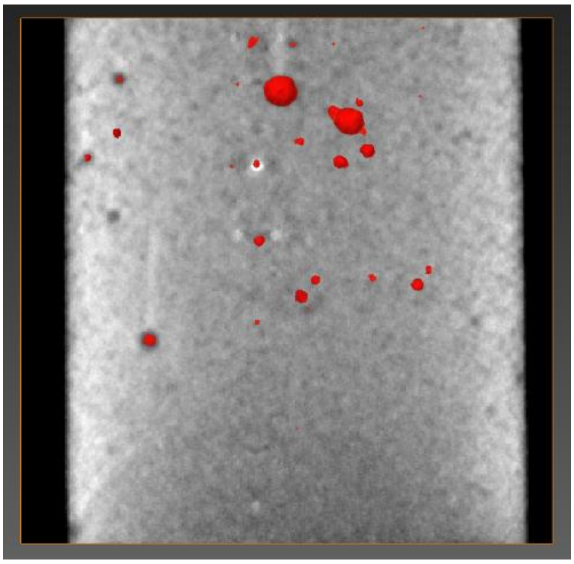

Figure 32: Cross section of encapsulation concrete, pores are highlighted with red color

Reviewing the slices in this reconstruction, it is clear that the pores are much better defined when compared with the previous setup. This material is further investigated with Volume Graphics.

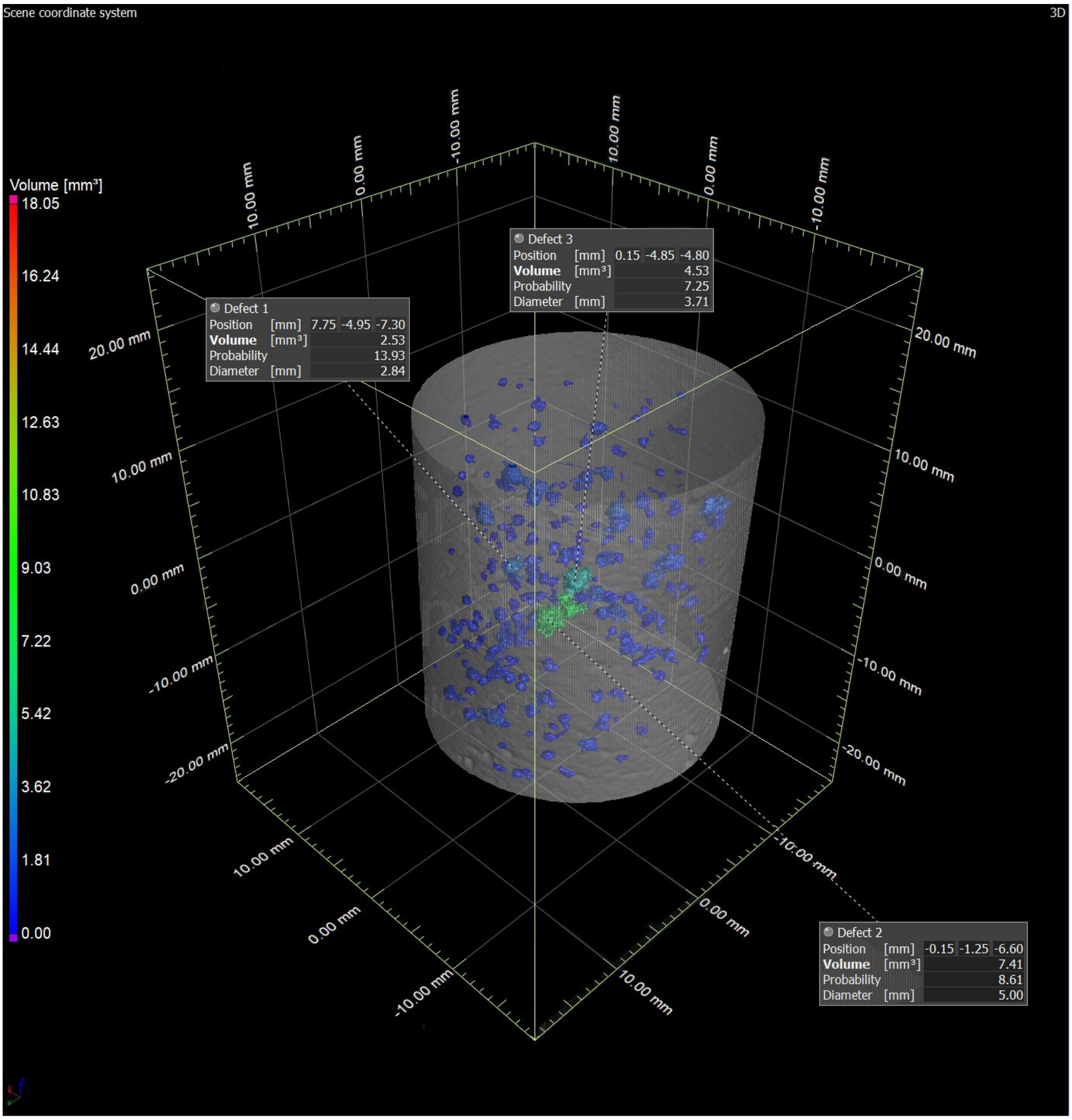

Defect 1

Position	[mm]	7.75	-4.95	-7.30
Volume	[mm³]			2.53
Probability				13.93
Diameter	[mm]			2.84

Defect 3

Position	[mm]	0.15	-4.85	-4.80
Volume	[mm³]			4.53
Probability				7.25
Diameter	[mm]			3.71

Defect 2

Position	[mm]	-0.15	-1.25	-6.60
Volume	[mm³]			7.41
Probability				8.61
Diameter	[mm]			5.00

Figure 33: 3D Rendered visualization of CEM III/B 42.5 LH/SR, encapsulation concrete using Volume Graphics

Figure 33 shows the volume reconstruction of the encapsulation concrete sample. The concrete sample itself is 60% transparent and the 3 biggest pores are again annotated. The volumes are notably smaller compared to the pores of the gallery lining sample. The scalebar has not been adjusted, resulting in the biggest pore being colored green.

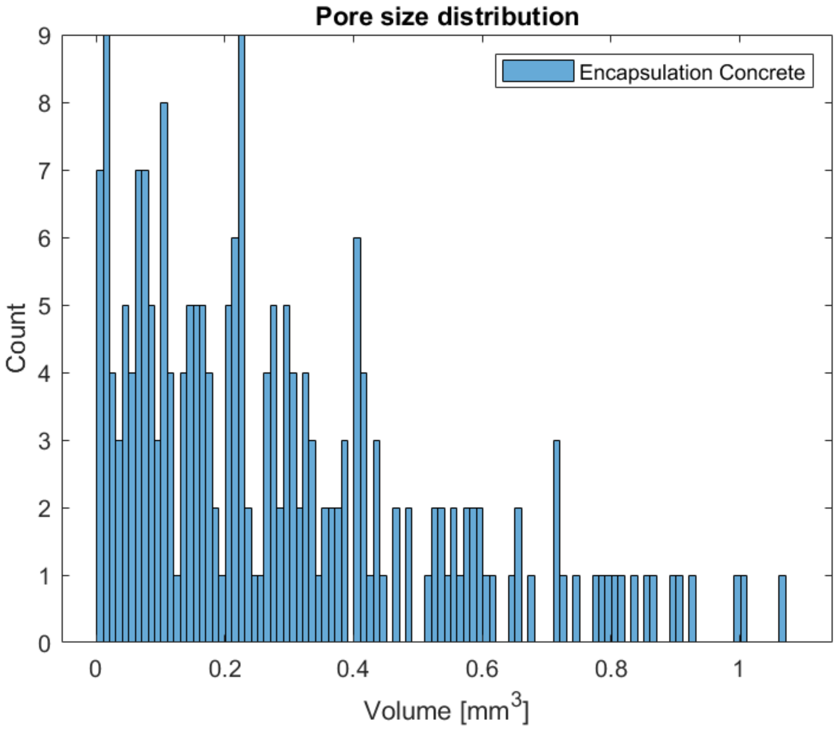

Figure 34: Pore size distribution of CEM III/B 42.5 LH/SR, encapsulation concrete

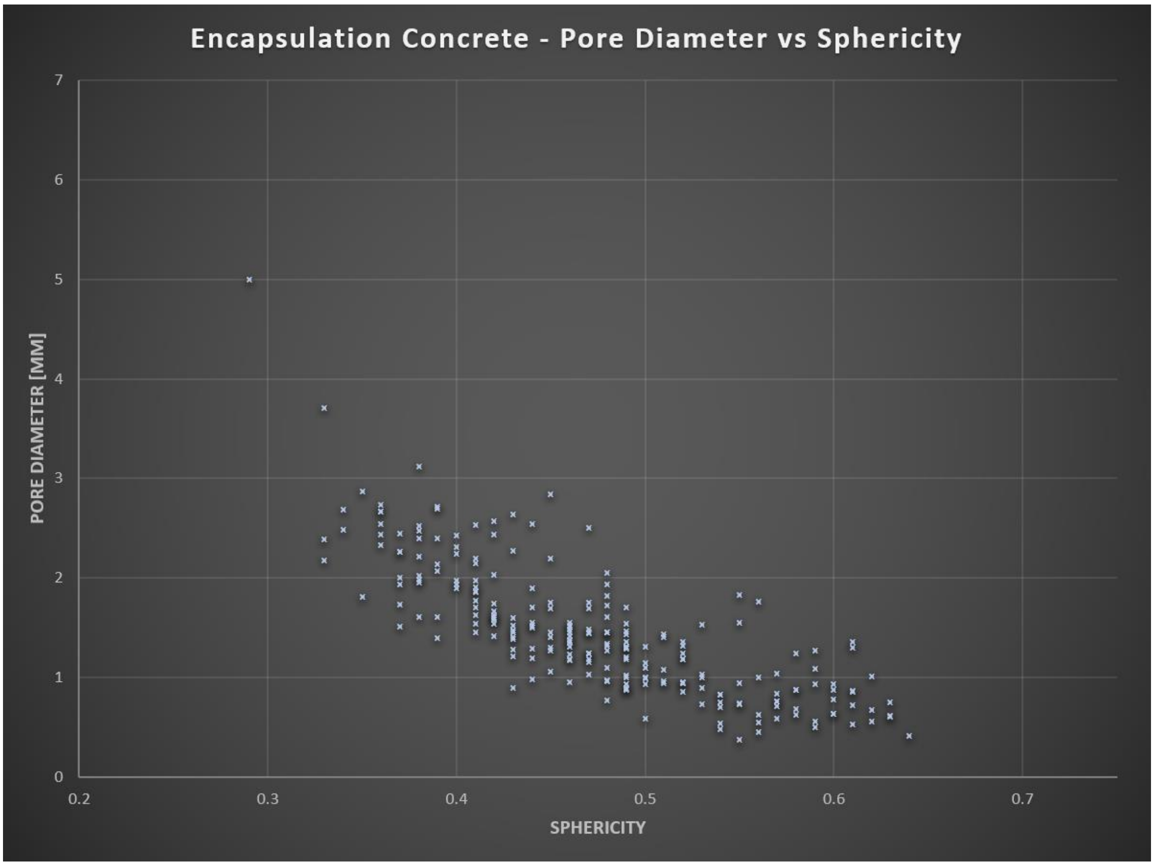

Figure 35: Sphericity of CEM III/B 42.5 LH/SR, encapsulation concrete

Figure 34 shows the pore size distribution of encapsulation concrete. The pores are detected using Volume Graphics and further analyzed in Matlab. This sample has a significant lower porosity resulting in a low pore count. This explains the step-behavior of the pore size distribution. Several pores have been detected above 0.5 mm^3 where most of the pores are around half of this value.

Figure 35 shows the sphericity vs pore diameter for this sample. When comparing this sphericity with the sphericity of the gallery lining concrete, it is clear that the data is less 'spread'. This indicates that the shape of the pores is generally better defined.

4.1.4 Foam concrete - CEM III/B 42.5N LH/SR + Foaming Agent

Using the same improved setup for encapsulation concrete, CEM III/B 42.5N LH/SR + Foaming agent, or foam concrete, samples have been analyzed with neutron tomography. Compared with the previous tomography studies, these samples have been conditioned. The concrete samples are 3 cm in diameter and have been oven dried for 24 hours at 45 degrees Celsius. One of the two samples have been immersed in heavy water for 2 days before the tomographies have been carried out. This is to test whether water uptake can be visualized. As concrete contains large amounts of hydrogen, heavy water was chosen. Both samples have been reconstructed. A slab out of the volume has been isolated which are visualized in Figure 36. On the left the dry foam concrete sample is shown. On the right, the second foam concrete that was immersed in heavy water is shown.

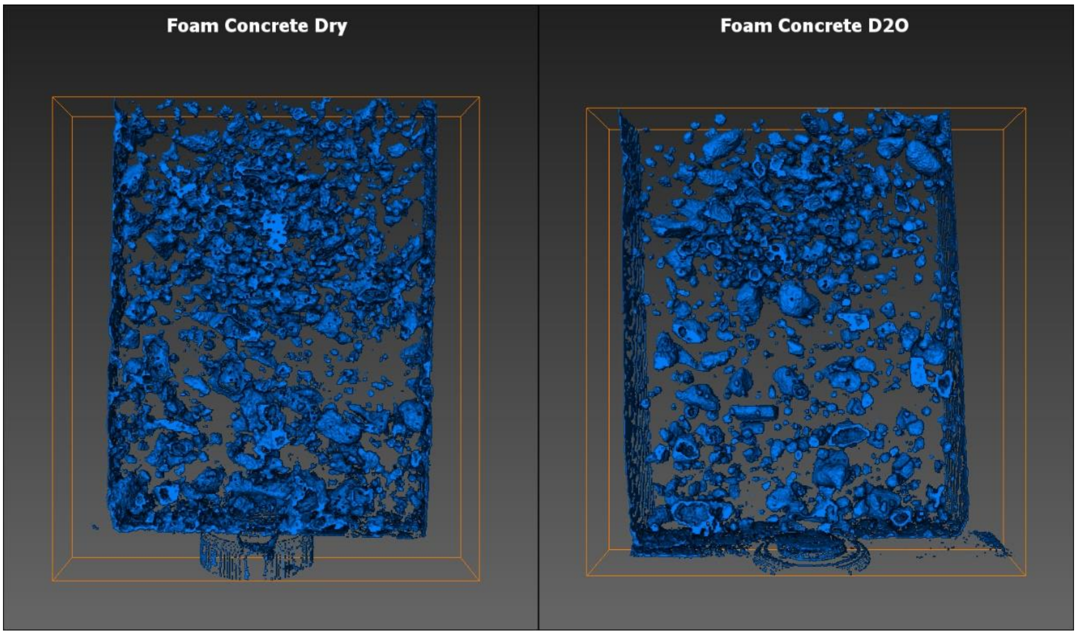

Figure 36: Internal structure of CEM III/B 42.5N LH/SR, foam concrete. Left: Dry sample. Right: Sample immersed in a mini-pool of D_2O

No clear distinction could be made between the immersed and non-immersed foamed concrete. There was no detectable grey value range corresponding with the D_2O. As the measurement took place overnight, and some heat is generated from the step motor which is in contact with the sample, the D_2O was assumed evaporated where two days of immersion was not sufficient for the retention of the absorbed D_2O.

The dataset of the dry foam concrete is further analyzed.

Table 7 shows the porosity data obtained with Volume Graphics pore analysis measurement.

Table 7: Porosity data of CEM III/B 42.5N LH/SR foam concrete

Material volume	14094.20 mm^3
Pore volume	1008.34 mm^3
Porosity	**6.68% ± 0.71%**

1870 pores have been detected where the average pore diameter is 1.50 ± 0.1 mm and the average pore volume is 0.50 ± 0.40 mm^3. The neutron tomography setup is identical to the setup used for the encapsulation concrete; hence the errors are similar as well. The largest pore volume detected is 13.92 ± 0.12 mm^3.

Since this concrete sample's composition is rather unique, no literature value could be found with regards to its porosity.

Figure 37 shows the 3D reconstructed sample with the concrete sample itself made transparent. The pores within the samples are highlighted according to a color code, where the smallest pore is blue and the biggest red. The biggest three pores are annotated where the pore diameter and pore volume are shown.

Figure 38 presents the pore size distribution of the CEM III/B 42.5N LH/SR + Foaming agent concrete. Characteristic is the high number of large pores, which reflects the structure of the material that is shaped by the foaming agent.

Figure 39 illustrates the sphericity of the sample. While the improved spatial resolution was demonstrated in the sphericity of the encapsulation concrete (Figure 35), the sphericity distribution for the foam concrete shows that for larger pores the shapes tend to be more spherical. These pores are assumed to be introduced as a result of reacting with the foaming agent.

Tomography measurements are suitable methods to reveal the pore size distribution but come with high error values. This method is unsuitable to obtain transport properties, as the time it takes to complete on tomography can take up to 6 hours.

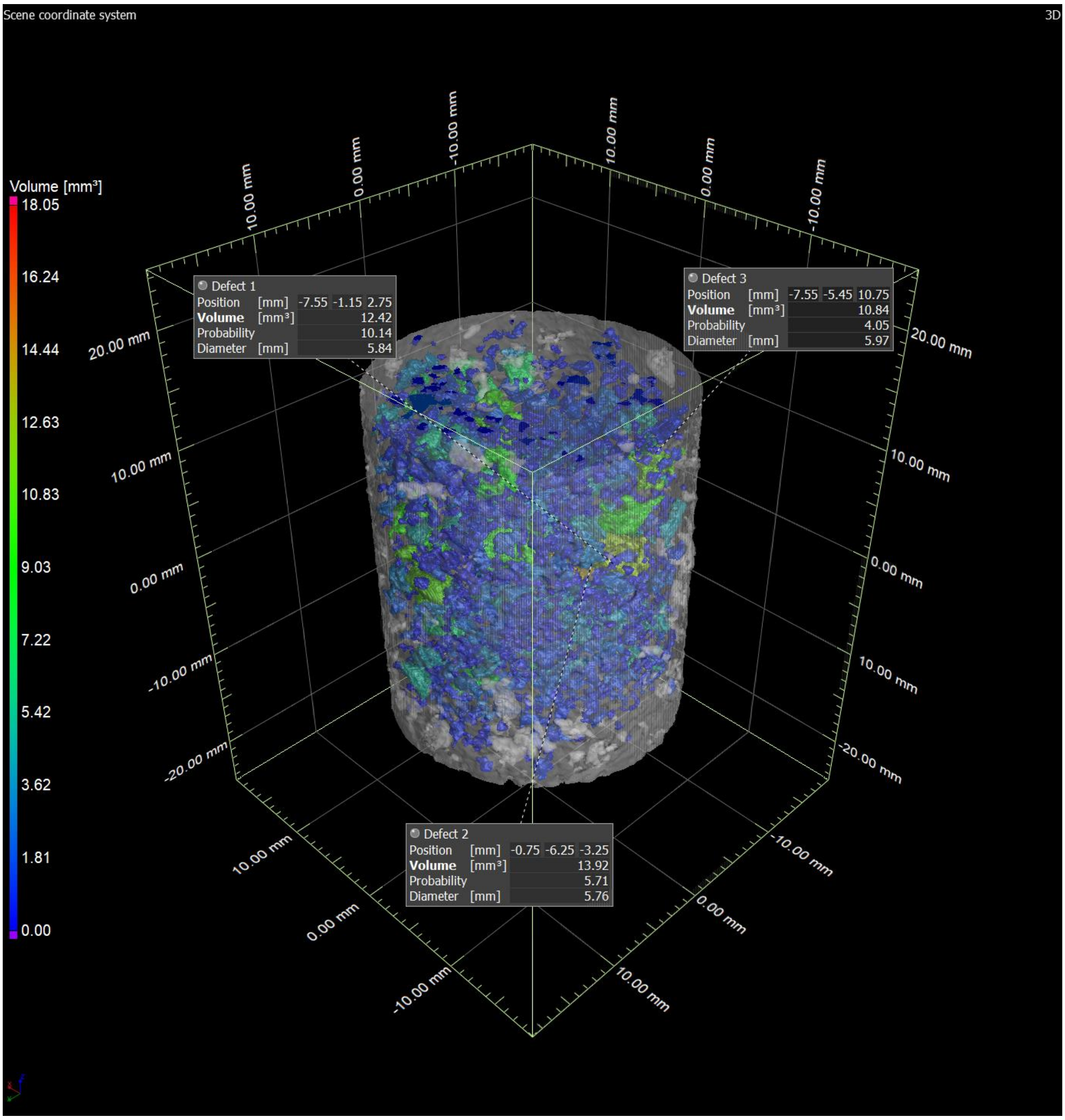

Defect 1

Position	[mm]	-7.55	-1.15	2.75
Volume	[mm³]			12.42
Probability				10.14
Diameter	[mm]			5.84

Defect 3

Position	[mm]	-7.55	-5.45	10.75
Volume	[mm³]			10.84
Probability				4.05
Diameter	[mm]			5.97

Defect 2

Position	[mm]	-0.75	-6.25	-3.25
Volume	[mm³]			13.92
Probability				5.71
Diameter	[mm]			5.76

Figure 37: 3D Rendered visualization of CEM III/B 42.5N LH/SR + Foaming Agent, foam concrete using Volume Graphics

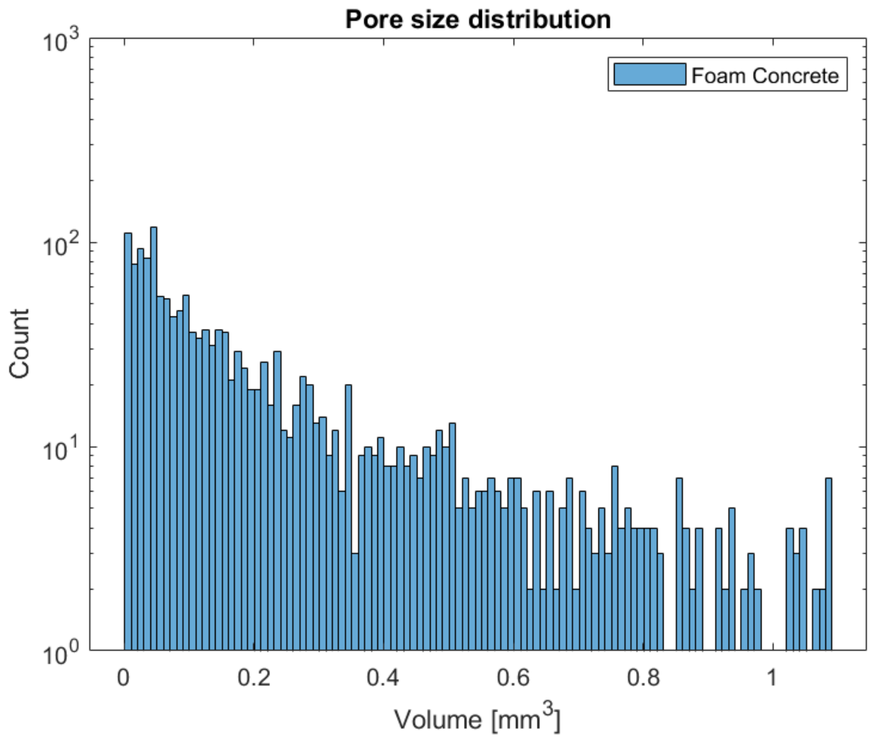

Figure 38: Pore size distribution of CEM III/B 42.5N LH/SR + Foaming Agent, foam concrete

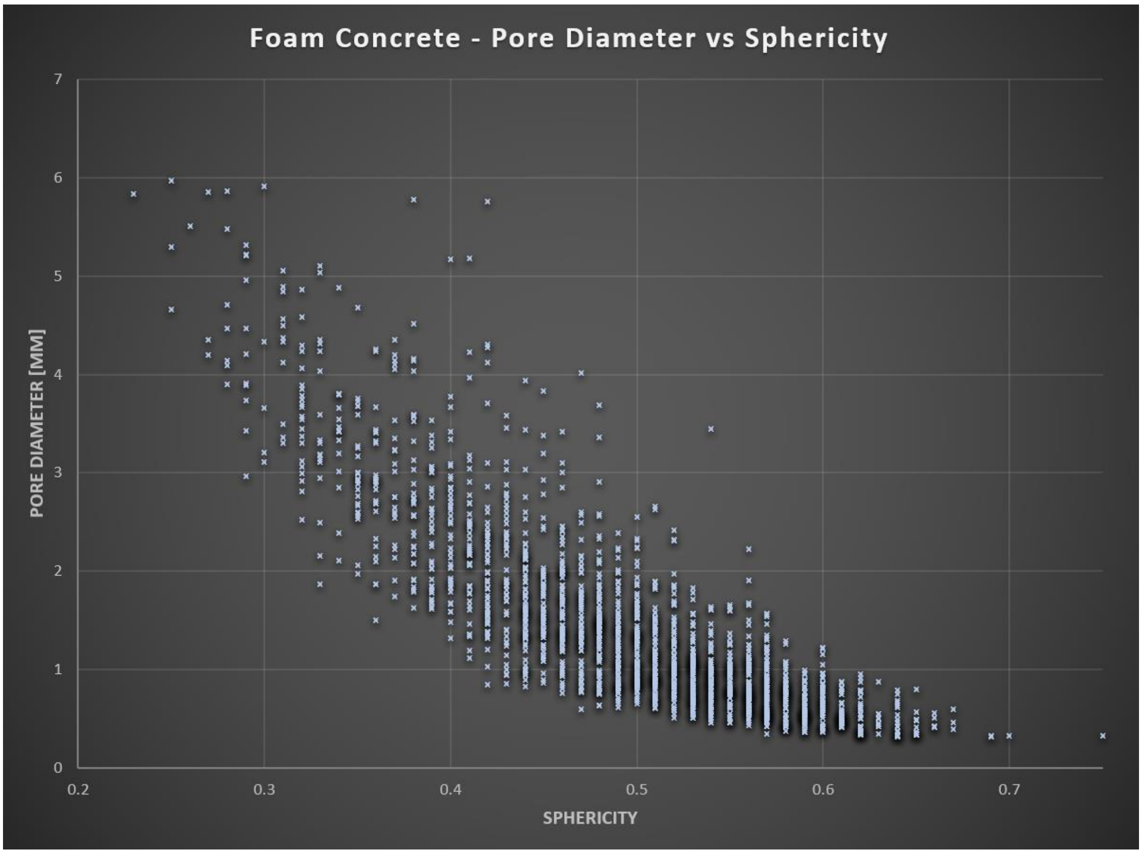

Figure 39: Sphericity of CEM III/B 42.5N LH/SR + Foaming Agent, foam concrete.

4.1.5 Neutron transmission imaging

The previous section demonstrated that it is possible to visualize the internal structure of concrete samples. Pore size distribution is detectable up to a certain resolution. The permeation of fluidic substances however cannot be measured with tomography measurements. Completing a tomography measurement takes on average 6 hours. To measure a transport parameter with neutron imaging, neutron transmission imaging has been applied to CEM III/B 42.5N LH/SR + Foaming Agent concrete specimen. The difference with a tomography study is that there is no rotation involved. The sample is kept stationery and radiographs are taken repeatedly, while the bottom part of the concrete sample is immersed in a mini-pool of D_2O. Capillary forces then drives the heavy water upwards. This process is visible as shown in Figure 40.

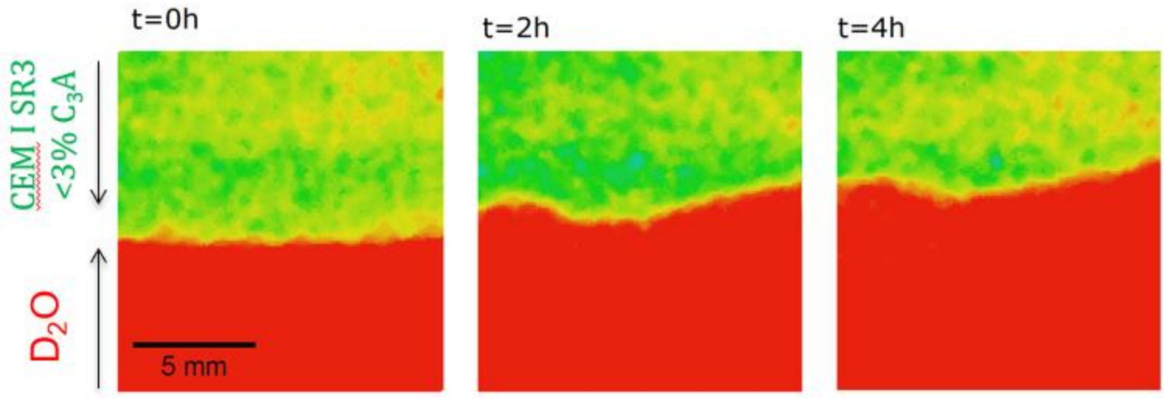

Figure 40: D_2O uptake in CEM III/B 42.5N LH/SR + Foaming Agent concrete measured with neutron radiography

Neutron imaging is a viable technique to perform permeability studies in concrete materials. However, the reactor required maintenance and as a result had a long down-time. The influence of degradation on the transport parameter is further studied with x-ray radiography, as the x-ray generator and detector were available for a longer period of time.

Using a slightly different setup, the water uptake is quantified. In the next sections, the water uptake and internal pore size distribution analysis are repeated for degraded and non-degraded samples.

4.2 Sorptivity studies on degraded concrete

As covered in the materials and methods section, concrete samples have been degraded manually in the laboratory in order to investigate the influence of boom clay pore water on the deterioration of concrete by comparing the sorptivity of non-degraded and degraded samples. Extracting large amounts of boom clay pore water is rather tedious, but knowing its composition is not challenging. The pore water has been synthesized in the lab and the samples have been degraded while keeping a spare set for comparison purposes. During the degradation, the pH value of the solution in which the samples are placed have been measured over time. The pH value will change as hydration products of the concrete samples will dissolve, measuring it over time tells us something about the rate at which the degradation takes place. The volume is 225 mL of milli-Q with 10 g/L NH_4Cl concentration for chloride attack simulation and 35 g/L Na_2SO_4 concentration for the sulphate attack simulation. The samples are labelled as shown in Table 8 and Figure 41 shows the samples and the beakers containing the solutions.

Table 8: Sample labelling and degradation selection

Sample	No degradation	Sodium sulphate degradation	Ammonium chloride degradation	Technique used for sorptivity measurements
1a	✓			X-ray radiography
1b		✓		X-ray radiography
1c			✓	X-ray radiography
2a	✓			ASTM C1585-13
2b		✓		ASTM C1585-13
2c			✓	ASTM C1585-13

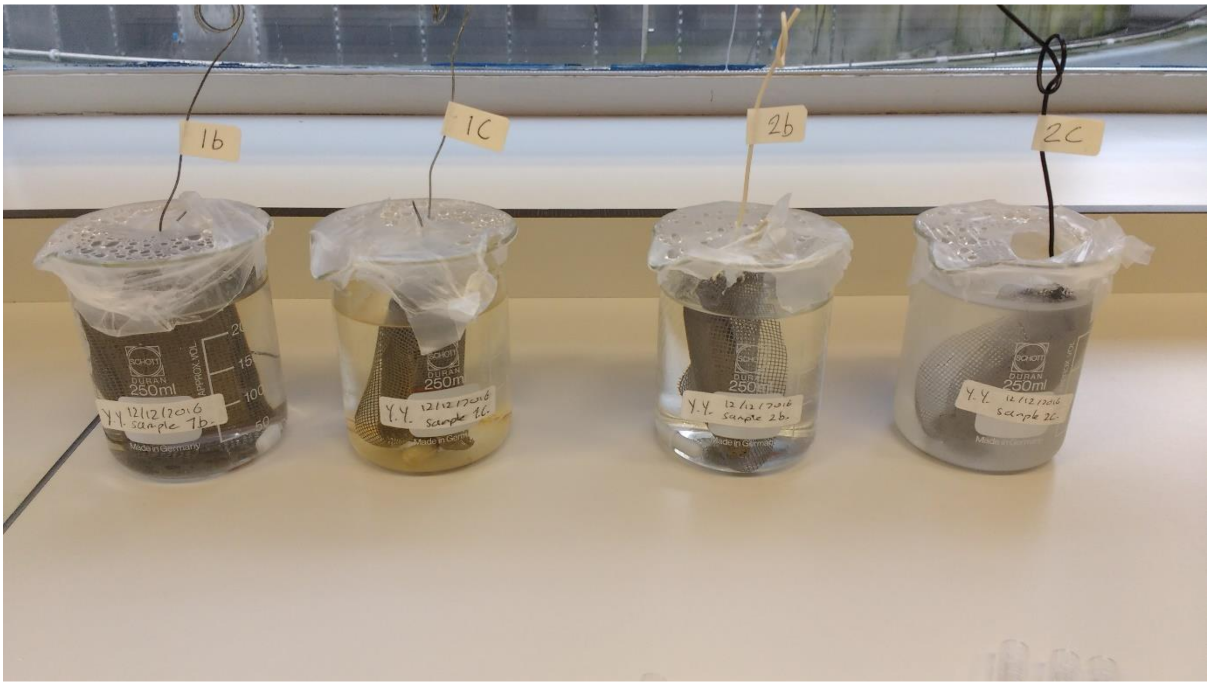

Figure 41: State of the CEM III/B 42.5N LH/SR + Foaming Agent, foam concrete samples after 37 days of exposure

4.2.1 pH evolution

Corrosion resistance of steel reinforcement in concrete is an extensively studied phenomena. pH studies in concrete are therefore often related to attempts to improve the concrete durability, in particular by corrosion prevention of the reinforcing steel by chloride penetration.

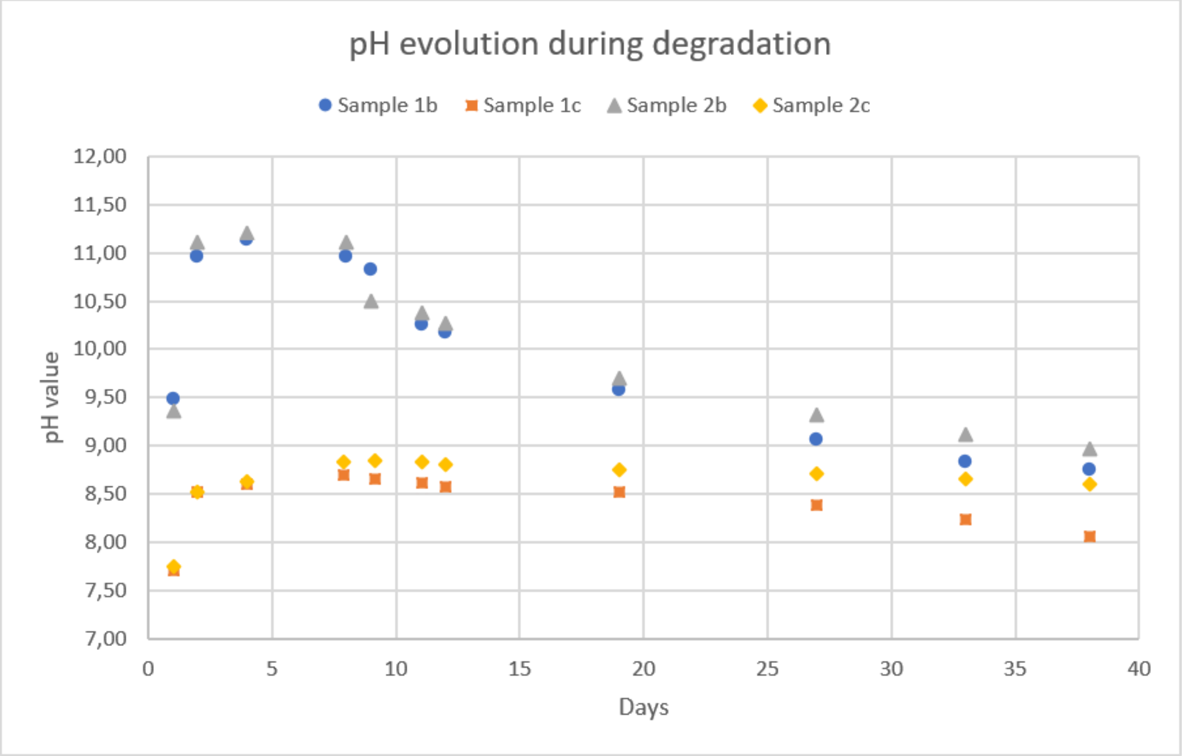

Figure 42: pH value of solution the samples were immersed in for degradation, measured over time

The pH evolution of the concrete samples investigated in this study has been measured and shown in Figure 42. Table 8 explains the sample labelling that is presented as the legend in the graph. Samples 1b and 2b are essentially exposed to the same sodium sulphate concentration. The difference in pH value between them is due to the difference in sample size. From days 19 to 40 however, the difference between 1c and 2c becomes larger. The peak pH value is reached rapidly, during the first few days of immersion. All samples exhibit a slow decrease of pH value after reaching the terminal value. The samples 1b and 2b show a more rapid reduction in pH value compared to the samples 1c and 2c.

In section 2.2.3 it is explained that sulphate attack involves the formation of AFt phases (ettringite), where hydration products are consumed. The slow decrease of the pH value is caused by the release of hydrogen ion of the concrete samples. Evolving pH value of the solution indicates the formation of new phases or the growth of existing phases. This influence on the concrete samples are further investigated with imaging and sorptivity tests.

4.2.2 Sorptivity by X-ray transmission imaging

Due to maintenance on the nuclear reactor, it was not possible to perform neutron transmission imaging to measure the rate of water absorption. X-ray transmission imaging is an alternative imaging method that is used to obtain the rate of water uptake. To save time, the x-ray setup was used to obtain the sorptivity of the samples.

3 concrete slabs were prepared for x-ray transmission imaging, according to the sample numbering in Table 3. Prior to the x-ray radiography, all samples are oven dried. The state of the non-degraded sample is shown in Figure 43.

Figure 43: Non-degraded CEM III/B 42.5N LH/SR + Foaming Agent, foam concrete, oven-dried until constant mass

The samples are prepared in accordance with ASTM C1585-13 standard for sorptivity measurement. Instead of measuring mass change, the rate of attenuation increase per pixel is measured. The setup is shown in the Figure 44.

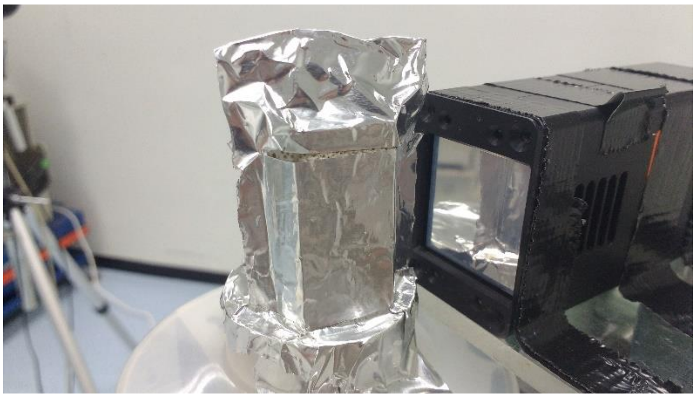

Figure 44: X-ray radiography set-up, a concrete sample is put in front of the x-ray camera

The output generated is an image file and a text file. There is a wide variety in how radiographs are reported in scientific articles. In a publication by Shafizadeh and others in 2014, the neutron radiographs obtained were reported in two styles: transmission images & graphs containing processed data. The transmission images are obtained by dividing the radiograph by the empty beam measurement. The processed data is obtained using the Beert-Lambert expression. The calculated water content is converted to I [mm], defined as the absorption in the ASTM C1585-13 standard.

The procedure to obtain the sorptivity is explained generally in section 2.4. Here, the radiographs are presented in grayscale. The darker the pixel color, the less interaction x-rays experienced with the sample.

In this measurement, the sorptivity of CEM III/B 42.5N LH/SR + Foaming Agent, foam concrete has been obtained, in both non-degraded and degraded state by sulphate and chloride attack. To increase the interaction rate of x-rays, Cs_2CO_3 solution with concentration 200 g/L has been used as a tracing agent (section 3.1.5).

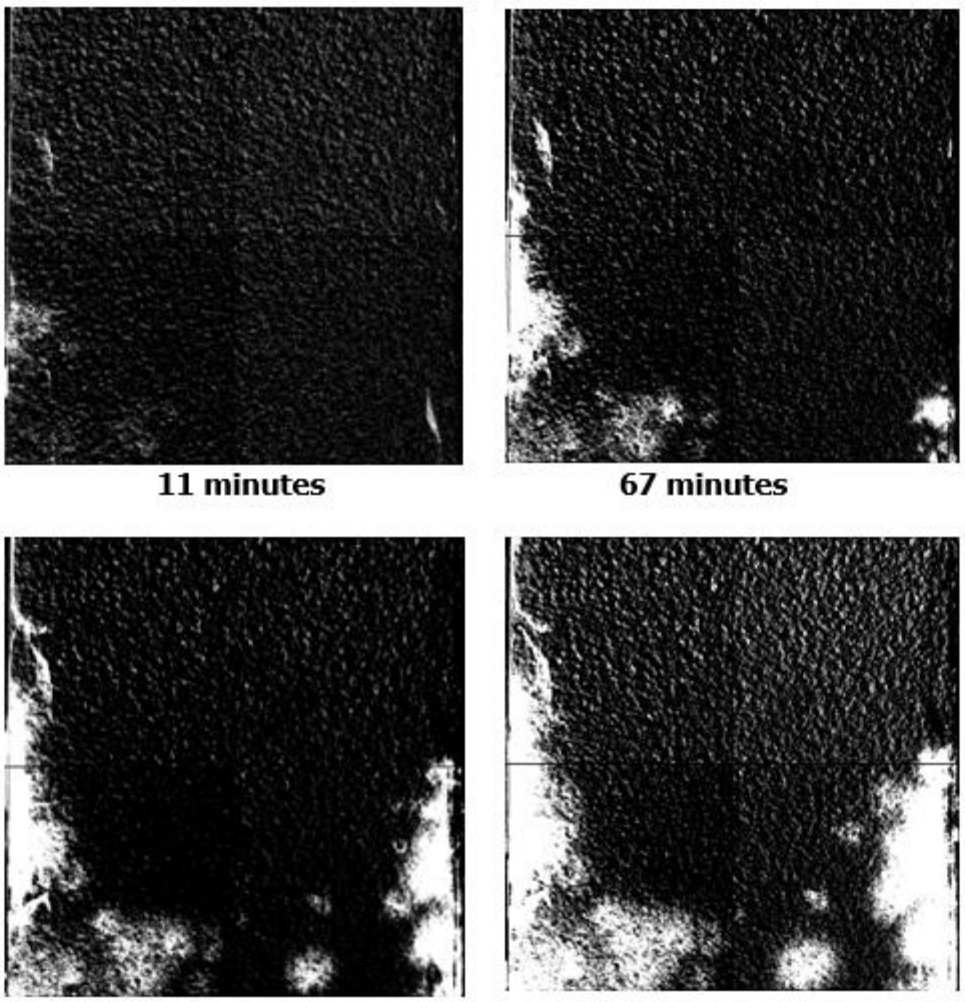
11 minutes 67 minutes
185 minutes 318 minutes

Figure 45: X-ray radiographs of CEM III/B 42.5N LH/SR + Foaming Agent, foam concrete, exposed to sulphate solution for 6 weeks

The four radiographs shown in Figure 45 demonstrate the capillary suction of water in the concrete sample. In these images, the portion section of the sample that was not in contact with the tracer solution is recorded over time. It shows that the tracer solutions climbed upwards in the edges of the sample (between the aluminum foil and the sample) and consequently continued inwards by capillary suction. This is however not an issue in the assessment of the sorptivity parameter, as the rate of capillary suction (correlated with rate of mass gain) can still be obtained.

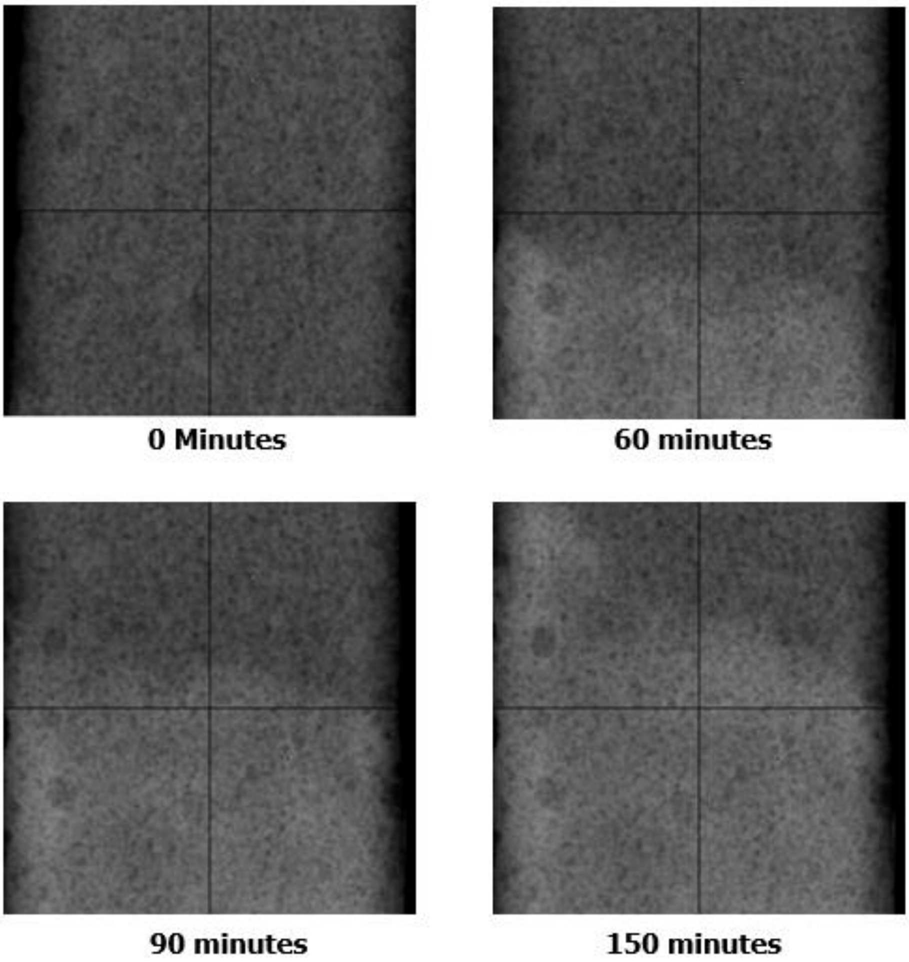

Figure 46: X-ray radiograph of CEM III/B 42.5N LH/SR + Foaming Agent, foam concrete, exposed to chloride solution for 6 weeks

In Figure 46, the images presented are raw radiographs as recorded by the camera, no processing was applied. In these images, water movement occurs at a more steady, symmetric way. The rate of capillary suction is surprising, in comparison with the non-degraded sample. In the bottom part of the radiographs, the brighter areas correspond to the zones saturated with the tracer solution. Within a shorter amount of time, this CEM III/B 42.5N LH/SR + Foaming Agent, foam concrete absorbs a far greater amount of water.

The data recorded by the X-ray camera (MEDIPIX) is generated and stored in a text file. The data is processed with Matlab. In order to obtain the sorptivity of the concrete samples, the method outlined in section 2.4 is used. The raw data is processed to obtain the water content according to equation [16]. Figure 47 shows part of this process, where the difference between radiographs is presented (width of each image represents 2.8 cm of material). Note that according to the Beert-Lambert law, to obtain the difference the dataset needs to be divided from each other, in order to subtract exponents from each other (see eq. 10).

The unit required for sorptivity is I [mm / $s^{1/2}$]. Time is measured during which the water gets absorbed by the concrete samples, in order to obtain the sorptivity of these samples with x-ray radiography. The Matlab code is shown in appendix 2. The sorptivity data of the measurements are displayed in Figure 48.

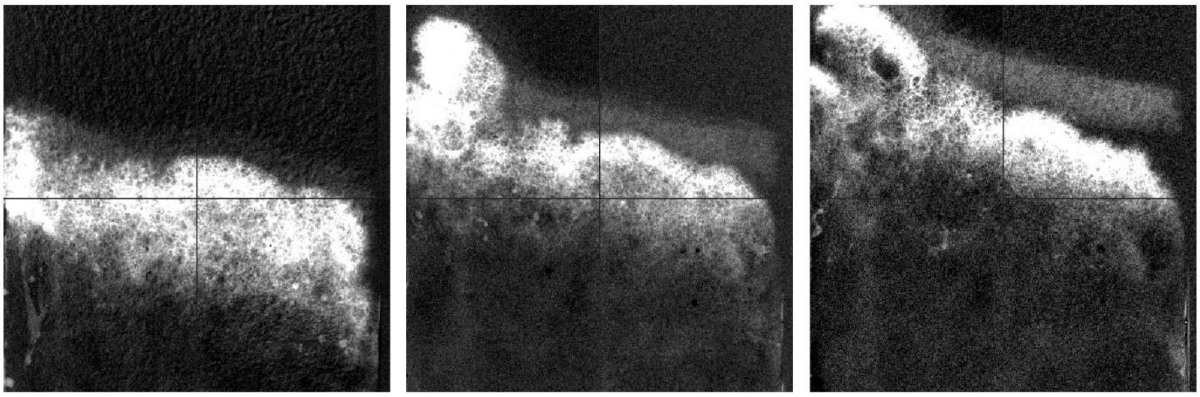

Figure 47: Water movement through chloride attack exposed CEM III/B 42.5N LH/SR + Foaming Agent, foam concrete, is visualized. Cs_2CO_3 tracer is dissolved in water. Left: 60-90 minutes, middle: 90-120 minutes, right: 120-150 minutes).

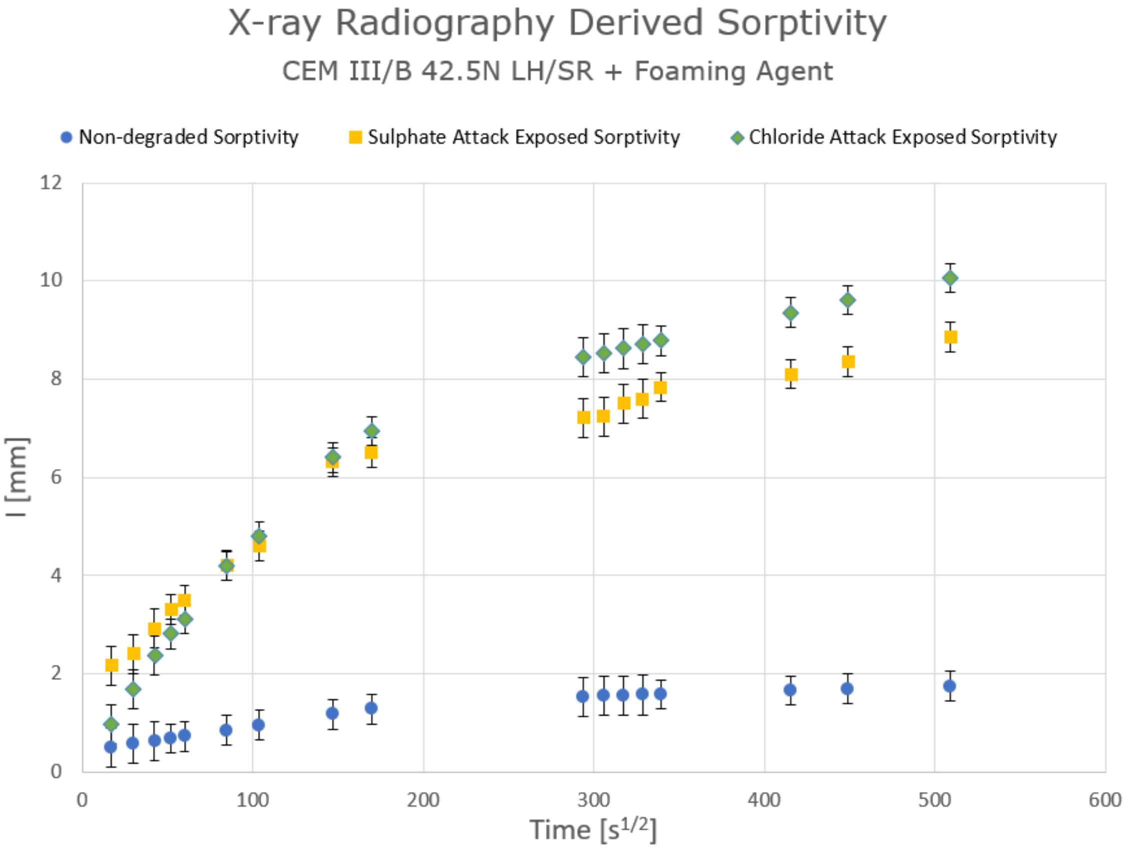

Figure 48: Sorptivity of non-degraded, sulphate exposed and chloride exposed CEM III/B 42.5N LH/SR + Foaming Agent, foam concrete samples

As the radiographs indicated, chloride exposed sample shows the highest sorptivity. Sorptivity graphs contain a gap between the initial and secondary absorption. The last measurement before 200 $s^{1/2}$ (x-axis) is measured 6 hours after contact with water. The next measurement, just below 300 $s^{1/2}$, takes place 25 hours later. It is possible to build a setup that performed the measurement automatically, but this would violate the ASTM standard. One could still perform the measurement, but the dataset obtained would typically display the transition from the first slope the next. The initial and secondary slopes describe different sorption mechanisms, the transition between the slopes are not relevant and therefore an over-night (automated) measurement is unnecessary. Least-square linear regression analysis is used to obtain the slope of the curve, which are different for the initial and secondary absorption stages. The ASTM standard states that up to 6 hours the graph should consists of a linear curve with a fixed slope. The time between 6 hours and 1 day after starting the sorptivity measurement, is when the slope transitions to a lower value (i.e. bends down to a lower angle). Once the secondary fixed slope is reached, least-square linear regression is applied again to obtain the secondary rate of absorption. The obtained slopes are summarized in Table 9.

Table 9: X-ray derived sorptivity of degraded and non-degraded CEM III/B 42.5N LH/SR + Foaming Agent, foam concrete

CEM-III/B 42.5N LH/SR + Foaming Agent, Foam Concrete	Initial absorption [mm/s$^{1/2}$]	Secondary absorption [mm/s$^{1/2}$]
1a - Non-degraded sample	$5.1 \cdot 10^{-3} \pm 0.47 \cdot 10^{-3}$	$1.0 \cdot 10^{-3} \pm 0.31 \cdot 10^{-3}$
1b – Sulphate Attack exposed sample	$29.8 \cdot 10^{-3} \pm 0.47 \cdot 10^{-3}$	$7.2 \cdot 10^{-3} \pm 0.31 \cdot 10^{-3}$
1c – Chloride Attack exposed sample	$46.9 \cdot 10^{-3} \pm 0.47 \cdot 10^{-3}$	$7.5 \cdot 10^{-3} \pm 0.31 \cdot 10^{-3}$

The samples 2b and 2c were exposed to a 50 g/L sodium sulphate and 9.8 g/L ammonium chloride solution, respectively. The total exposure time is 37 days. Sample 1b's initial absorption rate has increased by a factor of 5.8, while the secondary absorption rate has increased by a factor of 7.2. For sample 1c, the initial absorption has increased by a factor of 9.2 and the secondary absorption rate by a factor of 7.5.

Noteworthy is that due to degradation, the absorption rates in the initial stage are far more affected. Chloride attack exposed sample exhibits stronger initial capillary suction, but over longer timeframes the absorption rate is slightly higher than the sulphate attack exposed sample. This indicates that chloride attack exposed sample suffers more severe damage to its pore network.

4.2.3 Sorptivity by ASTM standardized testing

The sorptivity of samples 2a, 2b and 2c has been measured following the ASTM C1585-13 standard. In addition, the sorptivity of CEM III/B 42.5 LH/SR, encapsulation concrete sample has been measured as well. The encapsulation concrete is a dense, compact concrete designed for nuclear waste containment. As its aggregates are very fine, the porosity is much lower and consequently the sorptivity as well. The results are shown in Figure 49, Figure 50, Figure 51 and Figure 52.

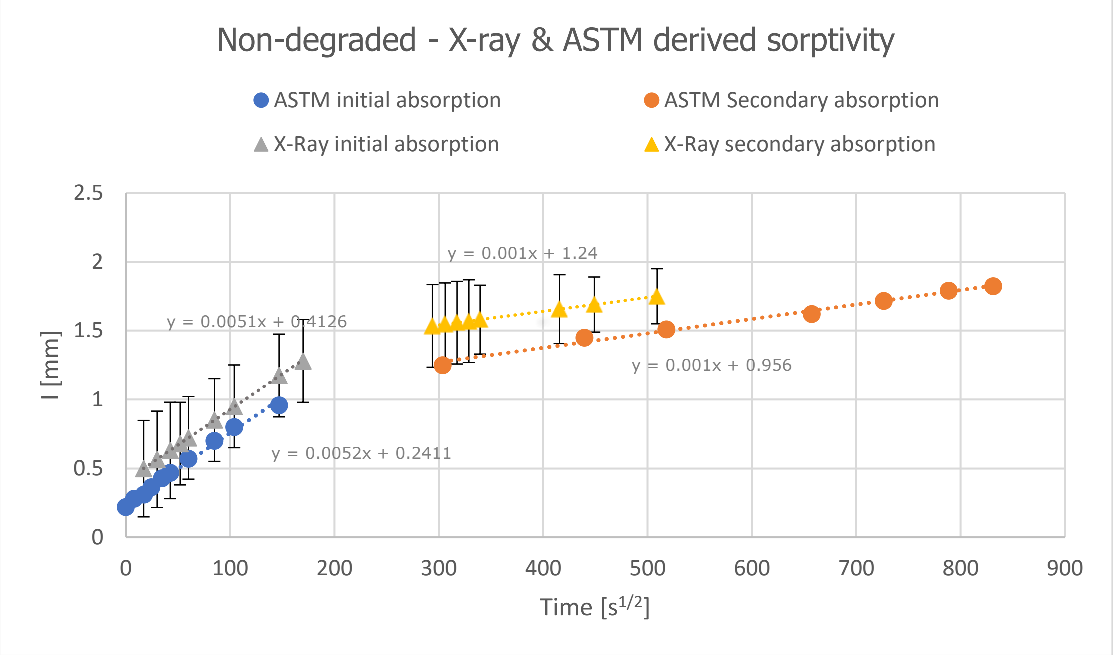

Figure 49: Sorptivity measurement of non-degraded CEM III/B 42.5N LH/SR + Foaming Agent, foam concrete CEM-III by X-Ray radiography and ASTM

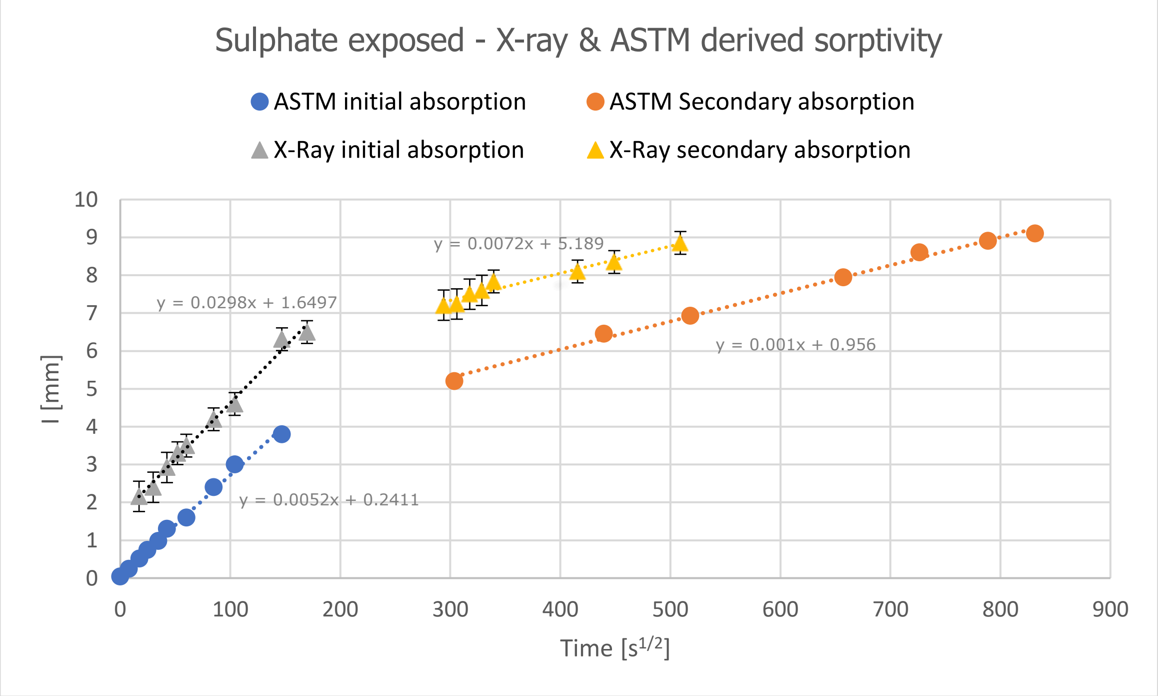

Figure 50: Sorptivity measurement of sulphate attack exposed CEM III/B 42.5N LH/SR + Foaming Agent, foam concrete by X-Ray radiography and ASTM

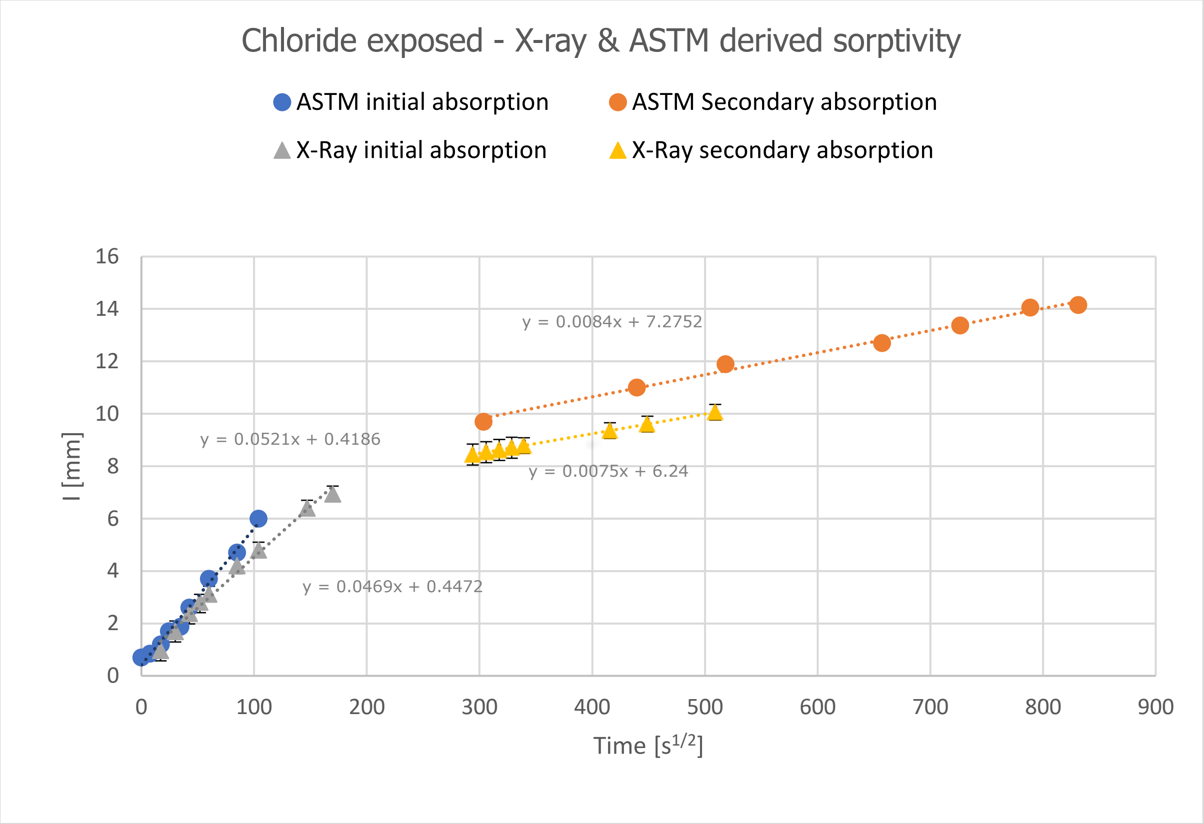

Figure 51: Sorptivity measurement of chloride attack exposed CEM III/B 42.5N LH/SR + Foaming Agent, foam concrete by X-Ray radiography and ASTM

Figure 51 show the initial and secondary absorption rates obtained from the ASTM standard, with the x-ray radiography derived data added. This allows immediate comparison of sorptivity behavior of the samples with the two different methods, X-ray radiography & ASTM. The slope of each curve represents the absorption rate, which the data are in good agreement. However, the samples prepared for x-ray radiography are not geometrically identical with the samples prepared for ASTM sorptivity measurements. For non-degraded samples, the x-ray samples show higher absorption distance, which is due to its smaller surface area. Equation [12] shows the inverse relation between the absorption distance and contact surface area. The difference in heights of the curves are therefore assumed to be related due to the different geometric shapes.

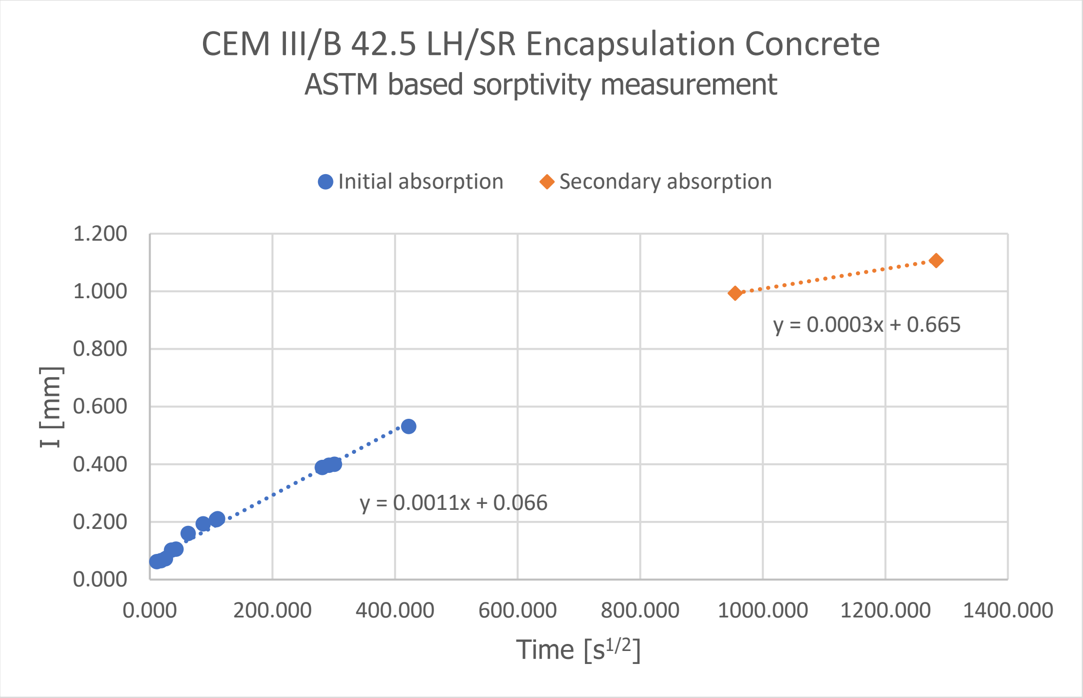

Figure 52: Water absorption measurement of CEM III/B 42.5 LH/SR, encapsulation concrete

Table 10: ASTM derived sorptivity of degraded and non-degraded CEM III/B 42.5N LH/SR + Foaming Agent, foam concrete and CEM III/B 42.5 LH/SR encapsulation concrete

CEM III/B 42.5N LH/SR + Foaming Agent, foam concrete	Initial absorption [mm/s$^{1/2}$]	Secondary absorption [mm/s$^{1/2}$]
2a - Non-degraded sample	$4.6\cdot10^{-3} \pm 0.35\cdot10^{-3}$	$1.0\cdot10^{-3} \pm 0.35\cdot10^{-3}$
2b – Sulphate Attack exposed sample	$27\cdot10^{-3} \pm 0.35\cdot10^{-3}$	$7.3\cdot10^{-3} \pm 0.35\cdot10^{-3}$
2c – Chloride Attack exposed sample	$38\cdot10^{-3} \pm 0.35\cdot10^{-3}$	$8.7\cdot10^{-3} \pm 0.35\cdot10^{-3}$
CEM III/B 42.5 LH/SR encapsulation concrete – Non-degraded	$1.1\cdot10^{-3} \pm 0.98\cdot10^{-5}$	$0.3\cdot10^{-3} \pm 0.98\cdot10^{-5}$

The sorptivity of CEM III/B 42.5 LH/SR encapsulation concrete is measured for validation and comparison purposes. Figure 31 (page 44) shows a cross section of this sample obtained with neutron tomography. Compared to the foam concrete samples, the rate of absorption for CEM III/B 42.5 LH/SR encapsulation concrete is roughly 5 times lower than the non-degraded CEM-III foam concrete. This is expected as the encapsulation concrete is highly compact, aside from a few pores that remained.

CEM III/B 42.5N LH/SR + Foaming Agent, foam concrete sample which has been exposed to sulphate and chloride attack clearly show a highly increased rates of absorption. The initial rate of absorption is increased 6 times by sulphate attack and 8.3 times by chloride attack. The secondary rate of absorption is affected more severe, namely 7.3 times by sulphate attack and 8.7 times by chloride attack.

The porosity of each concrete sample investigated with neutron tomography is mentioned in the previous subsections. In addition to the porosity, the sorptivity of the concrete samples is obtained. The data is plotted in Figure 53. The dark-red colored datapoint is obtained from literature, where both porosity analysis and sorptivity measurement have been performed on a mortar and concrete sample. Based on the concrete composition the authors report, CEM II/B-L is the closest designation according to the European classification. The difference of this concrete sample with the samples used in this thesis, is that the authors have used limestone instead of siliceous fly ash.

A porosity of 13.10% is reported for their concrete sample with a sorptivity of 0.323 mm/s$^{1/2}$ (Yang, et al., 2019). The aggregate size is not reported by the authors, but it remains interesting to see how their data compare with the data obtained in this study. This datapoint is shown as a dark-red diamond.

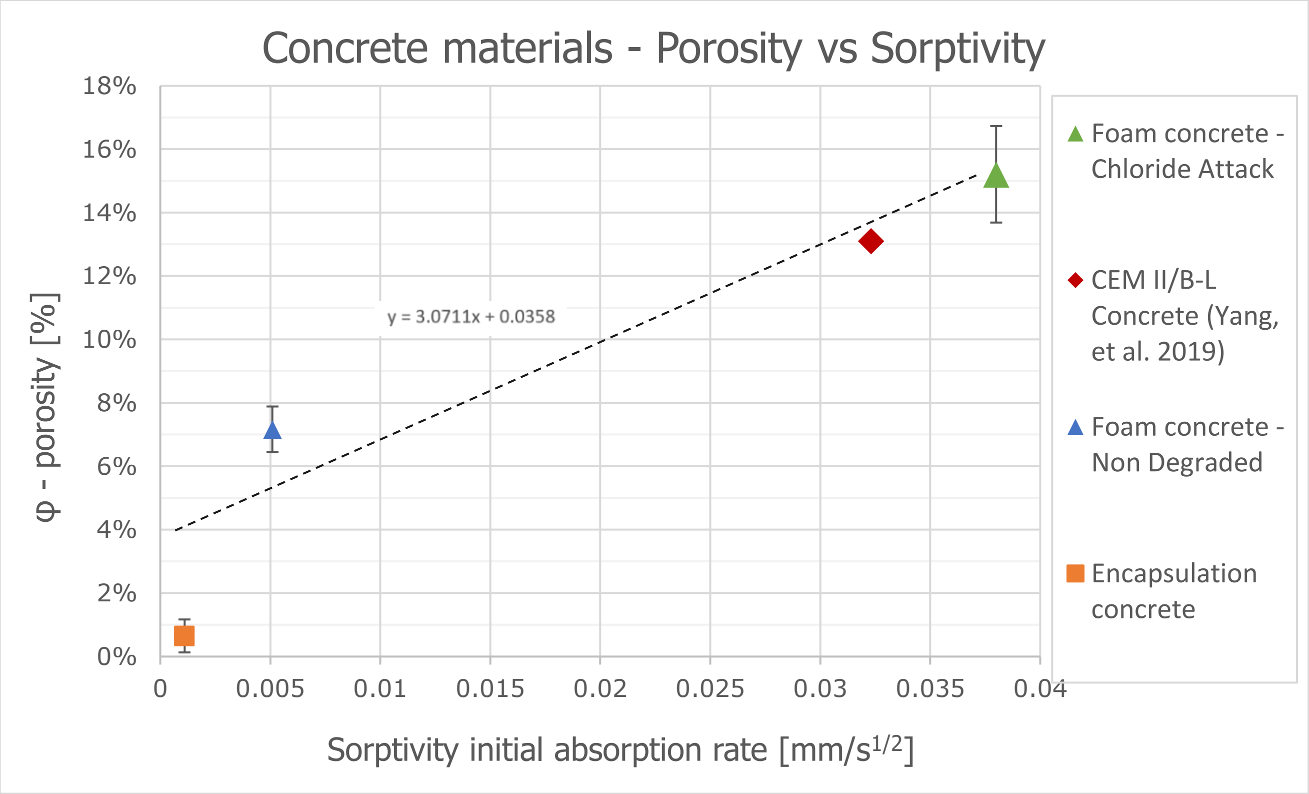

Figure 53: The porosity is plotted against the sorptivity of the initial absorption rate

The error is approximately 10% for the dataset obtained in this thesis. The authors did not report uncertainty in their data. The trendline indicates a linear relationship of:

$$\varphi \sim 3.07 \cdot S + 0.0358 \qquad [13]$$

The results which provide the datapoints of non-degraded foam concrete and degraded foam concrete presented in this graph (blue & green triangle), are presented in section 4.3.

The sorptivity datapoints from Figure 53 represent the initial absorption rates. Recall from section 2.4 (page 22) that a sorptivity plot consists 2 slopes, the first reflecting capillary absorption, the second the filling of the pores. The porosity vs sorptivity of the secondary absorption rate, is plotted in Figure 54.

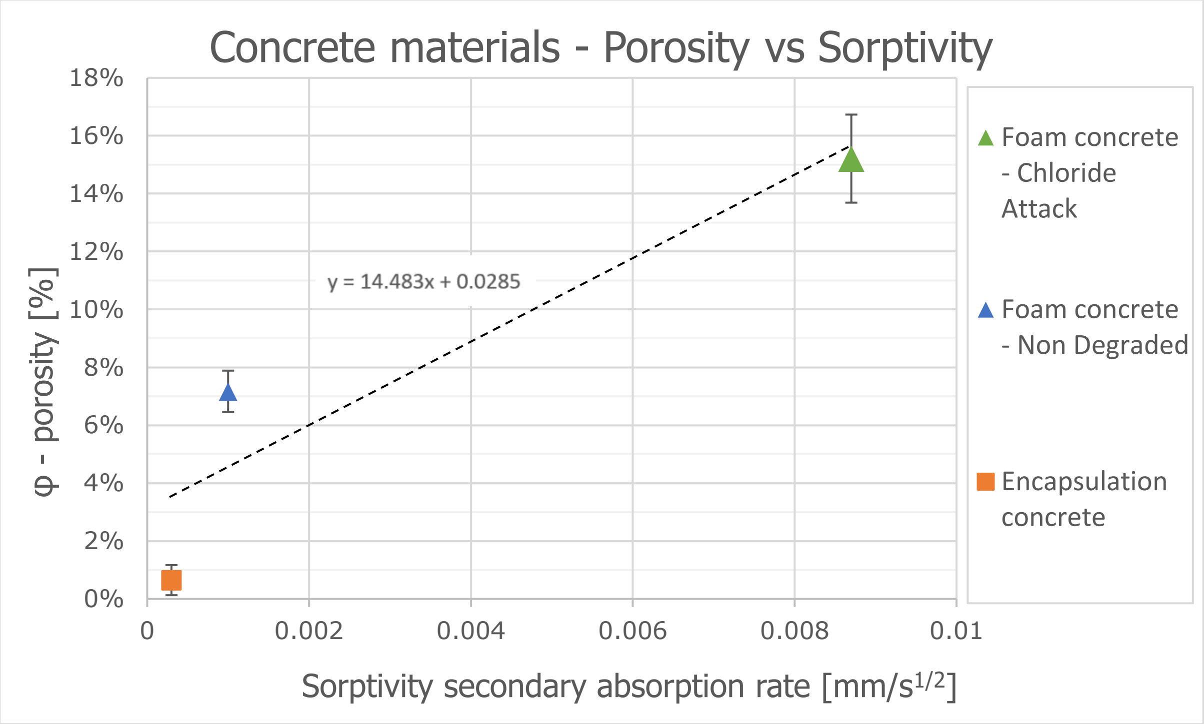

Figure 54:The porosity plotted against the sorptivity of the secondary absorption rate

For the secondary absorption rate, the slope is much steeper. The x-axis has been shortened compared to Figure 53, from the trendline the porosity and sorptivity relation reads:

$$\varphi \sim 14.48 \cdot S + 0.0285 \qquad [14]$$

The slope is nearly 5x higher when compares to the initial absorption rate, which in other words implies that when porosity is increased, the secondary absorption rate increases 5x slower. The capillary suction is 5x more affected by porosity change than for the process of pore filling.

4.3 Chloride attack quantification using Neutron Tomography

The ASTM and x-ray radiography sorptivity data indicate a severe impact on the pore network by chloride attack. This has inspired the idea to perform a neutron tomography measurement on the non-degraded sample and the chloride attack exposed sample (samples 1a and 1c from table 3). The sulphate exposed samples could not be measured as there was not enough time. The samples were oven-dried and covered in aluminum tape. The cover was necessary as cesium chloride was used as an image tracer, which is toxic. This sample was preferred over sample 2c, as it was larger in size. Due to lack of time, tomography for the sulphate attack exposed sample could not be performed.

The tomography data has been analyzed with Volume Graphics to obtain the porosity. The results are shown in Table 11 and Table 12. Since the foam concrete's composition is unique, no literature data could be found.

Table 11: CEM III/B 42.5N LH/SR + Foaming Agent, foam concrete non-degraded (sample 1A)

Material volume	13461.37 mm^3
Pore volume	1039.44 mm^3
Porosity	**7.17% ± 0.74%**

Table 12: CEM III/B 42.5N LH/SR + Foaming Agent, foam concrete chloride attack exposed (sample 1C)

Material volume	10451.94 mm^3
Pore volume	1874.9 mm^3
Porosity	**15.21% ± 1.68%**

Figure 55 shows the reconstructed volumes of both samples, using Avizo 3D Visualization & Analysis software. The aluminum wrapping is clearly visible. At the bottom the rotor stage is visible on which the samples are placed. The pictures do not provide the necessary information to quantify internal structure damage, but with image processing techniques the internal structure is revealed.

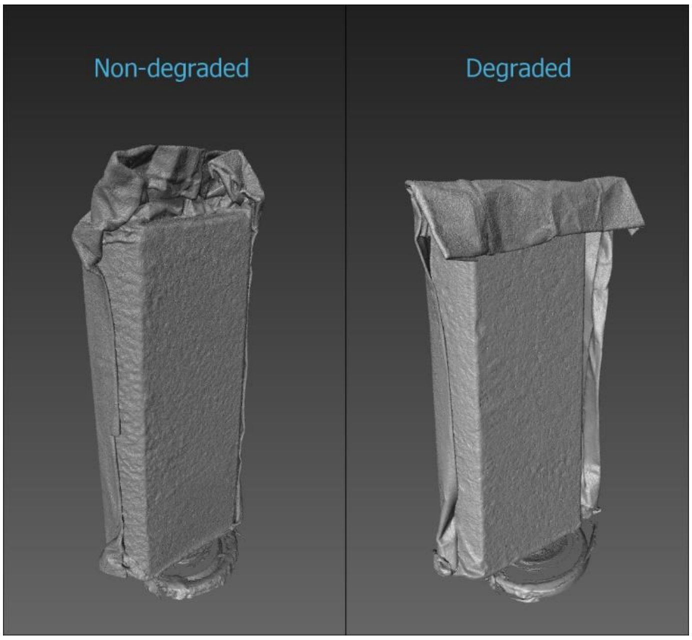

Figure 55: Reconstructed volume of non-degraded and chloride attack exposed CEM III/B 42.5N LH/SR + Foaming Agent, foam concrete

By the time these tomographies were ready to be performed, the neutron imaging setup received some improvements. Firstly, the setup was relocated closer to the reactor, yielding a higher flux of neutrons. This accelerates the measurement time as the camera saturates within a shorter amount of time which permits increased shutter speed. Instead of reducing measurement time, the temporal resolution can be improved. To improve the temporal resolution, the average of multiple images of the same object can be taken to counter the blurriness induced by the index of refraction of the scintillator and to smear out pixel-defects. Due to lack of time, multiple images of open beam and dark images are recorded to take its average. This method was not applied for the tomography data itself.

The scintillator was replaced with a thinner scintillator with higher quantum efficiency (the rate at which neutrons are converted into visible light. With the camera being replaced, the pixel size was measured to be 46 µm.

Reducing the scintillator thickness has the advantage that the index of refraction shifts the light less. This comes at a cost however, as, thinner scintillators will yield lower conversion rate, requiring longer beam exposure time to record neutron radiographs. As the setup was placed closer to the reactor core, the neutron flux is higher and reduces the required time of exposure, thus making this setup viable. Roughly 5 hours was required for each tomography measurement.

Figure 56 shows the internal pores and cavities between the concrete and aluminum tape. The colored pores are superimposed on the 3D reconstruction of the sample. The color categorization is automatically done based on size by Avizo's image processing algorithms.

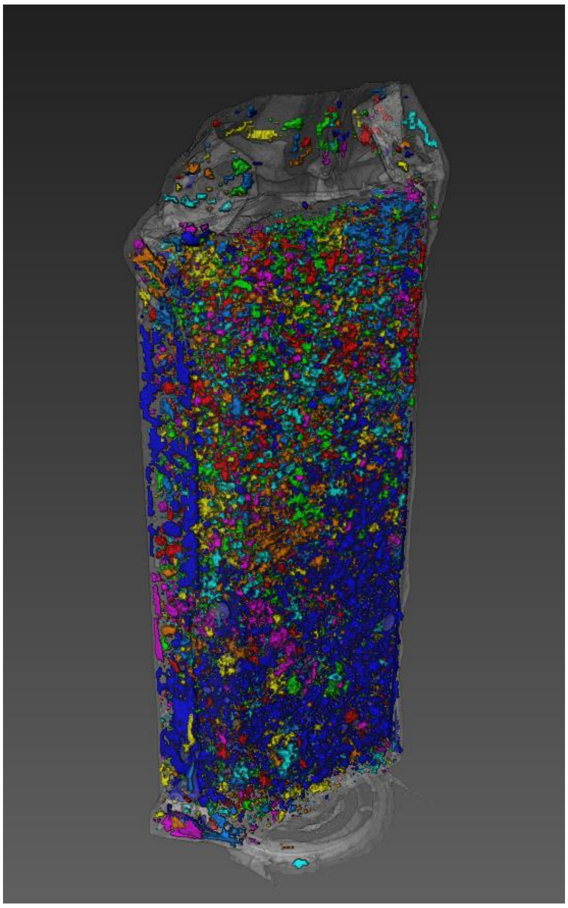

Figure 56: CEM III/B 42.5N LH/SR + Foaming Agent, foam concrete with pores identified and categorized based on size

The volume of interest is in the internal structure, imaging software have methods to extract a subvolume to filter out unwanted visualizations (in this case the aluminum foil and the concrete surface).

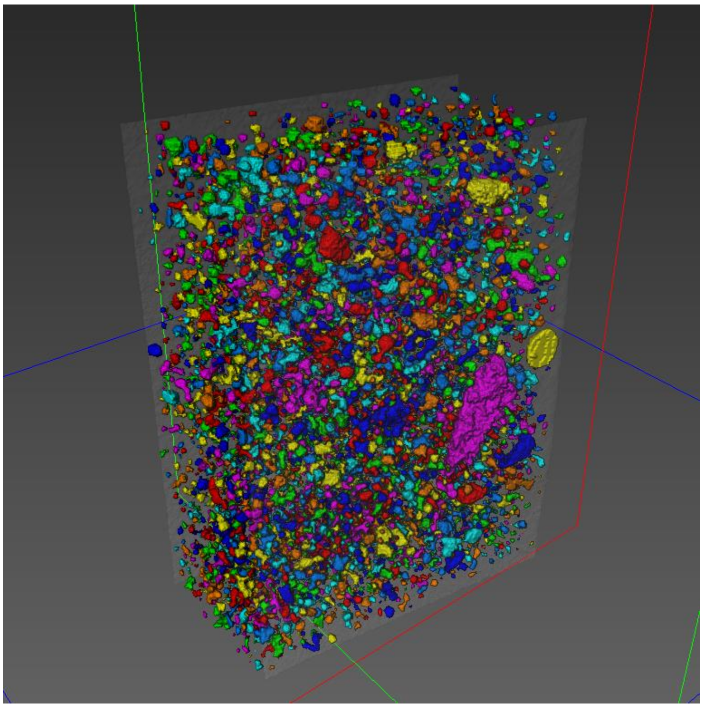

Figure 57: Pore size identification of CEM III/B 42.5N LH/SR + Foaming Agent, foam concrete

Figure 57 is the result of volume subtraction, sized roughly 1.5 cm in width, 0.8 cm in thickness and 2.0 cm in height. Useful information is stored for each detected void, such as volume and maximum length. The data is exported as a spreadsheet and analyses in MATLAB. Pore size distributions for both the non-degraded sample and degradation by ammonium chloride were obtained this way and compared in a histogram.

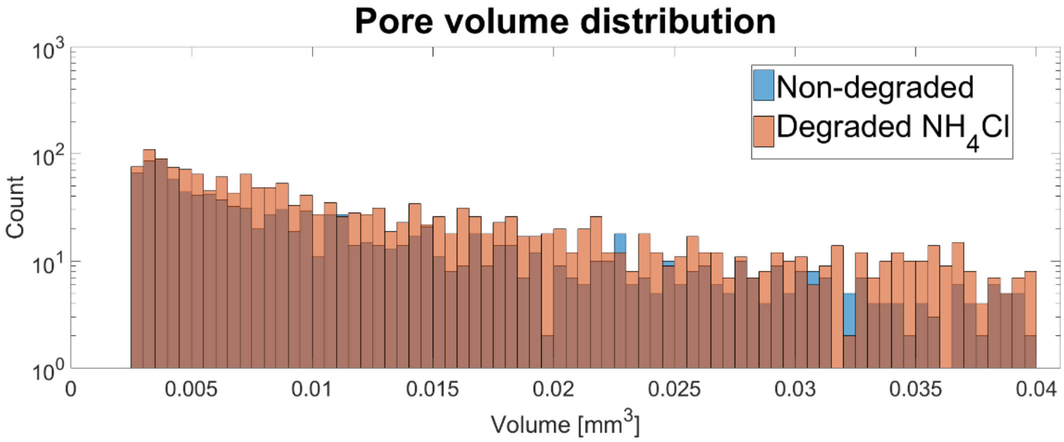

Figure 58: Pore volume distribution of CEM III/B 42.5N LH/SR + Foaming Agent, foam concrete. Non-degraded and chloride attack exposed samples are compared.

The histogram shows the pore size distribution obtained with neutron tomography. The dataset associated with the non-degraded sample is coloured blue, whereas the dataset associated with the degradation by chloride solution is coloured brown. The darker colored bins represent non-degraded data. The graph shows a combination of more pores being introduced in the degraded sample with the already existing pores having grown in size. A shift to the right on the graph indicates pore size growth, whereas a shift in the vertical direction indicates an increase in the pore size's count.

5. Conclusions

Sorptivity is a transport parameter which is at the same time a durability parameter. The assessment of concrete performance is often done by measuring the sorptivity and comparing the values for different concrete candidates, or to test the effectivity of a modification.

Tomography and radiography studies are non-destructive methods that allows the evaluation of the internal properties of a material. In this study, materials were provided on a regular basis by COVRA. Boom clay has been provided as well, due to the difficulty to obtain such materials and the necessary preservation conditions, non-destructive methods are highly practical.

Boom clay samples have been investigated with neutron tomography. The shape of the sample could be visualized well, however there were no distinguishable internal structures. Concrete samples are suitable for internal structure studies with neutron tomography. Pore size distributions have been obtained for CEM II/A to B-V gallery lining and CEM III/B 42.5N LH/SR + Foaming Agent, foam concrete samples. The smallest distinguishable difference in pore volume is 0.0005 mm^3 or the size of 80 µm. This is near the pixel size of 55 µm and is therefore likely to be contributed by noise, defects or saturation. A cluster of pixels with similar grey value should be treated as the smallest detectable object. Taking this in consideration, the smallest detectable pore size is roughly 250 µm.

The process of the water uptake through various concrete samples have been recorded with x-ray and neutron radiography. The water front movement is produced by recording radiographs repeatedly over time while the sample is kept stationary. It was not possible to perform a tomography in order to visualize the water uptake in 3D. The total exposure time required to complete one tomography, is far too long in order to perform the tomographies repeatedly in order to visualize the water front movement. This is possible with a synchrotron-based x-ray microtomography, as the radiation flux is significantly greater (Wildenschild, et al., 2005).

CEM III/B 42.5N LH/SR + Foaming Agent, foam concrete samples have been degraded in the lab by exposure to sulphate and chloride attack. Concentrations have been chosen based on simulated phase diagrams of concrete systems (Lagerblad & Tragardh, 1994). It is found that by chloride attack, the sorptivity of the concrete samples is increased by a factor of 7.5 during the second stage (>24hours). In the case of concrete samples exposed to sulphate attack, this factor is 7.2. The initial absorption stage of the sorptivity differs far greater. Chloride exposed concrete sample has nearly twice the absorption rate during the first 6 hours of contact with water. During sulphate degradation of concrete, salts and compounds tend to be formed at the border between the cement and aggregates. The present of sulphates will induce local formations of expansive products, such as gypsum and ettringite. At this stage, all structural strength is lost that the aggregate would otherwise introduce. The chloride exposed sample was mainly damaged due to the leaching of the cement. Therefore, the chloride exposed sample suffers from increased pore connectivity, whereas for sulphate exposed sample the damage is introduced near the aggregates/cement borders.

Using x-ray radiography to measure the rate of water uptake and calculating the sorptivity is proven to work. The highest deviation in the datasets of ASTM derived sorptivity and x-ray derived sorptivity is not greater than 10%.

Sorptivity data on the concrete samples used in this study has been compared with literature data. In a study performed in 1987, sorptivity measurements have been performed on concrete samples. The sorptivity data presented in their study, range from 0.5 $mm/s^{1/2}$ to 2.5 $mm/s^{1/2}$ (Hall and Yau, 1987). The data is in good agreement with the sorptivity data reported in this study, ranging from 1.0 $mm/s^{1/2}$ to nearly 50 $mm/s^{1/2}$ (degradation by chloride attack exposure).

In 2016, Xiong and others published an article regarding a similar research, where chloride attack exposed samples suffered the greatest loss of Vickers hardness.

6. References

Anderson, I., McGreevy, R. & Bilheux, H., 2019. *Neutron Imaging and Applications: A reference for the imaging community,* New York: Springer.

Arostegui, D. & Holt, M., 2019. *Advanced Nuclear Reactors: Technology Overview and Current Issues,* s.l.: Congressional Research Service.

Atkinson, A., 1985. *The time depence of pH within a repository for radioactive waste disposal,* Harwell: AERE.

Beaudoin, J., Ramachandran, V. & Feldman, R., 1990. Interaction of chloride and C-S-H. *Cement and Concrete Research,* pp. 875-883.

Belleghem, B. v. et al., 2016. Capillary water absorption in cracked and uncracked mortar - A comparison between experimental study and finite element analysis. *Construction and Building Materials,* pp. 154-162.

Boers, C., 2016. *Concrete degradation in OPERA geological repository concept investigated by SESANS,* Delft: s.n.

Castro, J., Bentz, D. & Weiss, J., 2011. Effect of sample conditioning on the water absorption of concrete. *Ceement & Concrete Composites,* pp. 805-813.

Culligan, P., Ivanov, V. & Germaine, J., 2005. Sorptivity and liquid infiltration into dry soil. *Advances in Water Resources,* pp. 1010-1020.

Dhir, R. K., McCarthy, M. J. & Newlands, M. D., 2002. *Concrete for Extreme Conditions.* s.l., ThomasTelford, pp. 88-89.

Diamond, S., 1986. *Cement Concrete and Aggregates,* p. 97.

Fredericci, C., Zanotto, E. & Ziemath, E., 2000. Crystallization mechanism and properties of a blast furnace slag glass. *Journal of Non-Crystalline Solids,* 31 10.pp. 64-75.

Gascogne, M., Davidson, C., Ross, J. & Pearson, J., 1987. Saline groundwaters and brines in plutons in the Canadian Shield. *Geological Association of Canada,* 33(1), pp. 53-68.

Hall, C., 1989. Water sorptivity of mortars and concretes: a review. *Magazine of Concrete Research,* pp. 51-61.

Hall, C. & Yau, M., 1987. Water Movement in Porous Building Mateirals - IX. The Water Absorption and Sorptivity of Concretes. *Building and Environment,* pp. 77-82.

Hirao, H., Yamada, K., H., T. & Zibara, H., 2005. Chloride binding of cement estimated by binding isotherms of hydrates. *Journal of Advanced Concrete Technology,* 3(1), pp. 77-84.

Huijts, J., 2014. *Paving the way for a neutron imaging setup in Delft,* Delft: Delft, University of Technology.

Kadak, A., 2016. The Status of the US High-Temperature Gas Reactors. *Engineering,* 2(1), pp. 119-123.

Kayyali, O. & Haque, M., 1988. *Cement Concrete Research,* p. 895.

Laaksoharju, M., 1990. *Measured and predicted groundwater chemistry at Äspö,* Äspö: SKP.

Laboratory, O. R. N., 2019. *How SNS works.* [Online]
Available at: https://neutrons.ornl.gov/content/how-sns-works

Lagerblad, B. & Tragardh, J., 1994. *Conceptual model for concrete long time degradation in a deep nuclear waste repository,* Stockholm: Swedish Cement and Concrete Research Institute.

Lin, W., Liu, C. & Li, M., 2016. *Influences of specific ions in groundwater on concrete degradation in sunbsurface engineered barrier system,* Taipei: Springer.

Luna, M., Arcos, D. & Duro, L., 2006. *Effects of grouting, shotcreting and concrete leachates on backfill geochemistry,* Stockholm: Swedish Nuclear Fuel and Waste Management Co.

McWhorter, D. & Sunda, D., 1977. Ground-Water Hydrology and Hydraulics. *Water Resources Publications,* pp. 79-80.

Midgley, H. & Illston, J., 1984. *Cement Concrete Research,* p. 546.

Ortegaa, J. et al., 2014. Durability and compressive strength of blast furnace slag-based cement grout for special geotechnical applications. *Materiales de construccion,* 64(313).

PCA, 2002. *Types and Causes of Concrete Deterioration,* Skokie, illinois: Portland Cement Association.

Savage, D. et al., 1992. Rate and mechanism of the reaction of silicates with cement pore fluids. *Applied Clay Science,* 7(1), pp. 33-45.

Slomka-Slupik, B., 2009. Chloride ions diffusion in hydrated cement paste immersed in saturated NH4Cl solution. *Cement, Wapno, Beton,* pp. 232-239.

Stangenberg, F. et al., 2009. *Lifetime-Oriented Structural Design Concepts.* Berlin: Springer.

Strobl, M. et al., 2009. Advances in neutron radiography and tomography. *Journal of Physics D: Applied Physics,* Volume 42, pp. 1-21.

Stronach, S. & Glasser, F., 1997. Modelling the impact of abundant geochemical components on phase stability and solubility of C-S-H system at 25°C: Na+, K+, SO42-, Cl-, CO32-. *Advances in Cement Research,* 9(36), pp. 167-181.

Struble, L., 1987. *The influence of cement pore solution on alkali-silica reaction,* s.l.: Purdue University.

Taylor, H., 1993. Nanostructure of C-S-H: current status. *Advances in Cement Based Materials,* pp. 22-37.

Tillman, 2016. *Tillman Chemical Building Materials.* [Online]
Available at: http://www.tillman.nl/CB/CBM%20UK/producten.htm

Tracz, T., 2016. Open porosity of cement pastes and their gas permeability. *Bulletin of the Polish Academy of Sciences,* 64(4).

Tuutti, K., 1982. Corrosion of steel in concrete. *CBI Research,* pp. 4-82.

Verhoef, E. et al., 2014. *Cementitious materials in OPERA disposal concept in Boom Clay,* s.l.: Covra N.V..

Verhoef, E. et al., 2014. *Cementitious materials in OPERA disposal concept in Boom Clay,* s.l.: Centraal Orgaan Voor Radioactief Afval.

Wildenschild, D., Hopmans, J., Rivers, M. & Kent, A., 2005. Quantitative Analysis of Flow Processes in a Sand using Synchrotron-Based X-ray Microtomogrpahy. *Soil Science Society of America,* pp. 112-126.

Xiong, C. et al., 2016. Deterioration of pastes exposed to leaching, external sulfate attack. *Construction and Building Materials,* pp. 52-62.

Yamada, K., Takahashi, T., Hanehara, S. & Matsuhisa, M., 2000. Effects of the chemical structure on the properties of polycarboxylate-type superplasticizer. *Cement and Concrete Research,* 30(1), pp. 197-207.

Yang, L. et al., 2019. Relationship between sorptivity and capillary coefficient for water absorption of cement-based materials: theory analysis and experiment. *Royal Society Open Science,* 06 June.

Yoon, I., 2010. *Reaction experimental study on chloride binding behavior in cement composition,* Delft: 2nd International Symposium on Service Life Design for Infrastructure.

Zibara, H., 2001. *Binding of external chlorides by cement pastes.* 1 ed. Toronto: National Library of Canada.

7. Appendix A - European cement classification system

Table 13: 27 products in the family of common cements. Adapted from EN 197-1 standard, version June 2000

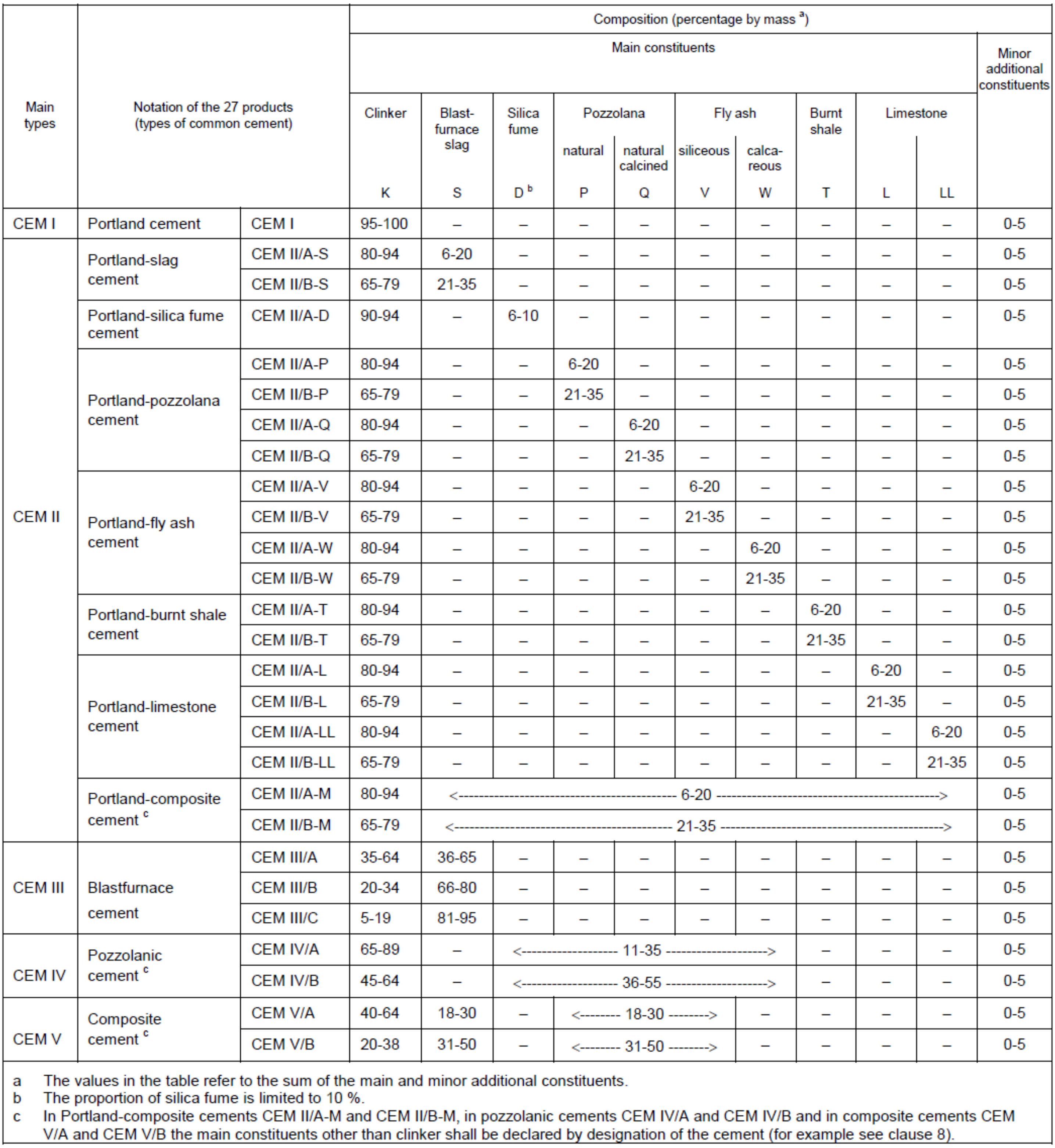

Main types	Notation of the 27 products (types of common cement)		Composition (percentage by mass [a])										
			Main constituents										Minor additional constituents
			Clinker	Blast-furnace slag	Silica fume	Pozzolana		Fly ash		Burnt shale	Limestone		
						natural	natural calcined	siliceous	calca-reous				
			K	S	D [b]	P	Q	V	W	T	L	LL	
CEM I	Portland cement	CEM I	95-100	–	–	–	–	–	–	–	–	–	0-5
CEM II	Portland-slag cement	CEM II/A-S	80-94	6-20	–	–	–	–	–	–	–	–	0-5
		CEM II/B-S	65-79	21-35	–	–	–	–	–	–	–	–	0-5
	Portland-silica fume cement	CEM II/A-D	90-94	–	6-10	–	–	–	–	–	–	–	0-5
	Portland-pozzolana cement	CEM II/A-P	80-94	–	–	6-20	–	–	–	–	–	–	0-5
		CEM II/B-P	65-79	–	–	21-35	–	–	–	–	–	–	0-5
		CEM II/A-Q	80-94	–	–	–	6-20	–	–	–	–	–	0-5
		CEM II/B-Q	65-79	–	–	–	21-35	–	–	–	–	–	0-5
	Portland-fly ash cement	CEM II/A-V	80-94	–	–	–	–	6-20	–	–	–	–	0-5
		CEM II/B-V	65-79	–	–	–	–	21-35	–	–	–	–	0-5
		CEM II/A-W	80-94	–	–	–	–	–	6-20	–	–	–	0-5
		CEM II/B-W	65-79	–	–	–	–	–	21-35	–	–	–	0-5
	Portland-burnt shale cement	CEM II/A-T	80-94	–	–	–	–	–	–	6-20	–	–	0-5
		CEM II/B-T	65-79	–	–	–	–	–	–	21-35	–	–	0-5
	Portland-limestone cement	CEM II/A-L	80-94	–	–	–	–	–	–	–	6-20	–	0-5
		CEM II/B-L	65-79	–	–	–	–	–	–	–	21-35	–	0-5
		CEM II/A-LL	80-94	–	–	–	–	–	–	–	–	6-20	0-5
		CEM II/B-LL	65-79	–	–	–	–	–	–	–	–	21-35	0-5
	Portland-composite cement [c]	CEM II/A-M	80-94	<-- 6-20 -->									0-5
		CEM II/B-M	65-79	<-- 21-35 -->									0-5
CEM III	Blastfurnace cement	CEM III/A	35-64	36-65	–	–	–	–	–	–	–	–	0-5
		CEM III/B	20-34	66-80	–	–	–	–	–	–	–	–	0-5
		CEM III/C	5-19	81-95	–	–	–	–	–	–	–	–	0-5
CEM IV	Pozzolanic cement [c]	CEM IV/A	65-89	–	<------------------ 11-35 ------------------>					–	–	–	0-5
		CEM IV/B	45-64	–	<------------------ 36-55 ------------------>					–	–	–	0-5
CEM V	Composite cement [c]	CEM V/A	40-64	18-30	–	<-------- 18-30 -------->			–	–	–	–	0-5
		CEM V/B	20-38	31-50	–	<-------- 31-50 -------->			–	–	–	–	0-5

a The values in the table refer to the sum of the main and minor additional constituents.
b The proportion of silica fume is limited to 10 %.
c In Portland-composite cements CEM II/A-M and CEM II/B-M, in pozzolanic cements CEM IV/A and CEM IV/B and in composite cements CEM V/A and CEM V/B the main constituents other than clinker shall be declared by designation of the cement (for example see clause 8).

8. Acknowledgements

The Reactor Institute Delft is a place where physicists, chemists and mechanical engineers work together to develop techniques that enables advanced material characterization. I have done my Bachelor’s end project (BEP) at the Applied Radiation & Isotopes (ARI, former Radiation Isotopes for Health RIH) department under supervision by dr. A. Denkova. I have investigated the creation, stabilization and fluorescence of polymersomes.

I am glad that I have chosen the Reactor Institute Delft again in doing research for the Master’s project. Here I have investigated clay and concrete materials using Neutron and X-ray tomography & radiography. It is precious to have a neutron source to work with. Investigating its potential in material characterization has been insightful and educational.

Special thanks and gratitude go to members of NPM2 (Neutron and Positron Methods for Materials): Dr. L. van Eijck, Dr. Z. Zhou for their continued support in performing the experiments, borrowing the neutron and x-ray cameras and advising on the obtained raw data.

Dr. J. Plomp’s quick mind in proposing technical solutions in measurement setups have been useful more than once.

The technical staff and the radiation protection services have always provided me with support, insightful suggestions and kindness. The Reactor Institute Delft benefits greatly from them, not only in the sense of security and safety, but also in keeping the good atmosphere (especially by maintaining the bar).

Image processing software licenses were provided by Thermo Fisher (Avizo) & Volume Graphics GmbH (VGStudio MAX), their software have been a great help to investigate internal structures.

Finally, gratitude is expressed to dr. D. Bykov & dr. A. Sabau for their supervision.